UNIVERSITÀ DEGLI STUDI DI PADOVA
DIPARTIMENTO DI INGEGNERIA CIVILE, EDILE E AMBIENTALE
Department Of Civil, Environmental and Architectural Engineering

Corso di Laurea Magistrale in Water and Geological risk Engineering

TESI DI LAUREA

The Modigliana landslide of May 2023: monitoring systems and analysis of displacements

Relatore:
Filippo Catani

Laureando: Giada De Franceschi
Matricola 2074301

ANNO ACCADEMICO 2024-2025

A mia sorella Greta.

Per aspera ad astra.

Abstract

In May 2023, Emilia Romagna was affected by an exceptional meteorological event, characterized by precipitations of high intensity and duration. The heavy rains triggered a high number of landslides with serious consequences on the territory, infrastructure and local communities. Considering the above context, this thesis focuses on the analysis of a landslide that occurred in conjunction with the extreme event, located around the Romagna Apennines, particularly vulnerable to slope instability phenomena.

The aim of the work was to understand in detail the evolutionary dynamics of the landslide, through an integrated approach that combines the geological characterization of the slope, the rainfall event and the instrumental control. The monitoring system installed includes a weather station, a total station, GPS, reflectors, extensometers and InSAR data capable of recording the detect small dimensional deformations of a body subjected to mechanical stress.

The collected data were processed to define the relationship between rainfall and landslide movements, highlighting significant rainfall thresholds and differentiated slope responses depending on local hydrogeological conditions. A comparison was also conducted between the different types of monitoring data to validate the simulations and identify any discrepancies between the observed and predicted behaviour.

The results obtained highlight the usefulness of an integrated monitoring system for the prediction and management of landslide events. The methodology adopted represents a valid tool for the mitigation of hydrogeological risk and the protection of the territory, especially in Apennine contexts with high susceptibility to landslides.

Sommario

Introduction 1
1. Frameworks of May 2023 events 3
1.1 Study area 3
1.2 Meteorological context of the extreme events..... 5
1.3 Framework of the rainfall events and occurred landslides 9
..... 13
1.4 Geology of the area 14
1.5 Introduction to landslide monitoring systems and rainfall-landslide correlations 16
2. Materials and methods..... 18
2.1 Landslide 1 - Via Lago Characterization..... 18
2.2 Monitoring system description 25
3. Results 37
3.1 Results of monitoring systems..... 37
3.1.1 Extensometers and piezometers results 37
3.1.2 Total station and reflectors result 44
3.1.3 GNSS-GPS results..... 54
3.1.4. InSAR data results..... 59
4. Discussion..... 64
4.1 Extensometers..... 64
4.2 Reflectors..... 66
4.3 GPS..... 68
4.4 SAOCOM data 71
5. Conclusions 74
Bibliography 78

List of Figures

Figure 1. Borders of the province of Forlì-Cesena. 4
Figure 2. Geopotential, temperature and wind analysis map at 500 hP from the IFS-ECMWF model at 12 UTC on 1 May 2023 (top left) and at 12 UTC on 2 May 2023 (top right) and at 12 UTC on 3 May 2023 (bottom center). 5
Figure 3. Weather map with fronts, showing the surface pressure values and the synoptic subjects identified on the Euro-Atlantic scenario, at 02 (00 UTC) on 15 May (top) and at 02 (00 UTC) on 17 May (bottom). 6
Figure 4. Radar composite reflectivity maps for May 17 at 01:15 (23:15 UTC 16/05/2023) top left, 03:50 (01:50 UTC) top right, 05:40 (03:40 UTC) center left, 07:00 (05:00 UTC) center right, 07:35. 8
Figure 5. Radar composite reflectivity maps for May 17 at 11:00 (09:00 UTC), top left, 12:50 (10:50 UTC), top right, and 14:40 (12:40 UTC), bottom. 8
Figure 6. Cumulative precipitation observed in the event from 1st to 3rd May 2023, with indication of the specific values and the boundaries of the municipal territories. 9
Figure 7. Cumulative precipitation of May 2023. 12
Figure 8: Geographic distribution of landslides inventoried by the Emilia-Romagna Region. 13
Figure 9: Map of the Geological-Structural Domains of the Emilia-Romagna Region - General Directorate for Land and Environmental Care, Land Protection Sector... 15
Figure 10: Landslide 1 – Via Lago landslide orthophoto. 19
Figure 11: location plan with position of geognostic surveys. 20
Figure 12: location plan with position of ERT and SRT surveys. 21
Figure 13: location plan with position of HVRS and MASW. 22
Figure 14. Extract from sheet 254 of the Geological Map of Italy, corresponding to the Via Lago slope. 23
Figure 15. Schematic representation of a buckling failure (left) and the role of water pressures (right) in determining limit stresses (from Tommasi et al., 2009). 24
Figure 16. Location of the different monitoring systems. 26
Figure 17. Schematic representation of the total station. 27
Figure 18. Schematic representation of GNSS system. 28
Figure 19. Borehole exstensometer. 29
Figure 20. Schematic representation of an inclinometer. 29
Figure 21. Casagrande piezometer. 30
Figure 22. Representation of the acquisition mode of SAR satellites. 32
Figure 23. Basic principle of phase difference radar interferometry. 32
Figure 24. Google Earth aerial view of the focus area for the satellite survey. 33
Figure 25. Technical data of SAOCOM acquisitions in ascending orbit. 34
Figure 26. Technical data of SAOCOM acquisitions in descending orbit. 35
Figure 27. Location of extensometers, piezometers and weather station. 37
Figure 28. Results recorded by the weather station for mean air humidity from 29 February 2024 to 31 December 2024. 38
Figure 29. Results recorded by the weather station for precipitation from 29 February 2024 to 31 December 2024. 38
Figure 30. Results recorded by the weather station for air temperature from 29 February 2024 to 31 December 2024. 39
Figure 31. Results recorded by the weather station for wind velocity from 29 February 2024 to 31 December 2024. 39
Figure 32. Exstensimeter C_0102 trend from 29 February 2024 to 31 December 2024. 40
Figure 33. Exstensimeter C_0103 trend from 29 February 2024 to 31 December 2024. 40

Figure 34. Exstensimeter R_0003 trend from 29 February 2024 to 31 December 2024. 41
Figure 35. Exstensimeter R_0004 trend from 29 February 2024 to 31 December 2024. 41
Figure 36. Exstensimeter R_0005 trend from 29 February 2024 to 31 December 2024. 42
Figure 37. Exstensimeter R_0006 trend from 29 February 2024 to 31 December 2024. 42
Figure 38. Water height C_0103 trend from 29 February 2024 to 31 December 2024. 43
Figure 39. Water height R_0006 trend from 29 February 2024 to 31 December 2024. 43
Figure 40. Reflectors position along the slope. 44
Figure 41. Point coordinate graph, Easting of P1001, P1002, P1003, P1004, P1005, P1006 and P1007. 45
Figure 42. Point coordinate graph, Easting of P1008, P1009, P1010, P1011, P1012, P1013 and P1014. 45
Figure 43. Point coordinate graph, Easting of P1015, P1016, P1017, P1018, P1019, P1020 and P1021. 46
Figure 44.Point coordinate graph, Easting of P1022, P1023, P1024, P1027, P1028, P1029 and P1030. 46
Figure 45. Point coordinate graph, Easting of P1031, P1032, P1034, P1035, P1036, P1038 and P1039. 47
Figure 46. Point coordinate graph, Northing of P1001, P1002, P1003, P1004, P1005, P1006 and P1007. 47
Figure 47. Point coordinate graph, Northing of P1008, P1009, P1010, P1011, P1012, P1013 and P1014. 48
Figure 48. Point coordinate graph, Northing of P1015, P1016, P1017, P1018, P1019, P1020 and P1021. 48
Figure 49. Point coordinate graph, Northing of P1022, P1023, P1024, P1027, P1028, P1029 and P1030. 49
Figure 50. Point coordinate graph, Northing of P1031, P1032, P1034, P1035, P1036, P1038 and P1039. 49
Figure 51. Point coordinate graph, Heigth of P1001, P1002, P1003, P1004, P1005, P1006 and P1007. 50
Figure 52. Point coordinate graph, Heigth of P1008, P1009, P1010, P1011, P1012, P1013 and P1014. 50
Figure 53. Point coordinate graph, Heigth of P1015, P1016, P1017, P1018, P1019, P1020 and P1021. 51
Figure 54. Point coordinate graph, Heigth of P1022, P1023, P1024, P1027, P1028, P1029 and P1030. 51
Figure 55. Point coordinate graph, Heigth of P1031, P1032, P1034, P1035, P1036, P1038 and P1039. 52
Figure 56. Coordinate graph of reference points, Easting of CS1, CS2, CS3 and CS4. 52
Figure 57. Coordinate graph of reference points, Northing of CS1, CS2, CS3 and CS4. 53
Figure 58. Coordinate graph of reference points, Height of CS1, CS2, CS3 and CS4. . 53
Figure 59. GPS location on the area of interest. 54
Figure 60. GPS100ITA data. 55
Figure 61. GPS200ITA data. 55
Figure 62. GPS300ITA data. 56
Figure 63. GPS400ITA data. 56
Figure 64. GPS500ITA data. 57
Figure 65. GPS600ITA data. 57
Figure 66. GPS700ITA data. 58
Figure 67. GPS800ITA data. 58

Figure 68. EGMS data (C-band Sentinel-1) for the Via Lago landslide area of interest in ascending (top) and descending (bottom) orbits. 59
Figure 69. SAOCOM point density for the Via Lago side area. Ascending data at the top, descending data at the bottom. 60
Figure 70. SAOCOM reflectors in SqueeSAR mode with unique reference code, with analysed points highlighted in magenta..... 60
Figure 71. Deformation/time graphs for two points, SAOCOM A9XTKFJ and A9YF015 in the landslide centre area. 60
Figure 72. Comparison between SAOCOM (left) and ALOS-2 (right) point densities in the vicinity of the Via Lago landslide. 62
Figure 73. SAOCOM descending data of the slop upstream. 63
Figure 74. SAOCOM descending data of the slope downstream..... 63
Figure 75. Vertical (blue arrow) and horizontal (yellow arrow) displacement vectors of GPS devices..... 70
Figure 76. ALOS-2 points discussed in comparison with SAOCOM, highlighted in magenta..... 71
Figure 77. Comparison between SAOCOM-ALOS2 time series on points A7OUMA2 (red) and A7VEC1S (blue)..... 72
Figure 78. Results recorded by the weather station for precipitation from 1 January 2025 to 1 December 2025..... 76
Figure 79. Effects of water pressure and reinforcement. F represent the safety factor, from Hoek and Bray 1977. 77

List of Tables

Table 1. Daily precipitation on 1st and 2nd, May 2023 in the province of Forlì-Cesena, near the landslide. 9
Table 2. Daily precipitation >70 mm on May 16, Forlì-Cesena province. 10
Table 3. Monitoring methods categorized by data acquisition technique. 17

Introduction

In the last decades, hydrogeological instability has emerged as one of the most environmental issues affecting the Italian territory, particularly in geologically complex and morphologically articulated contexts such as those of the Apennines. Landslides, debris flows and mudflow can be triggered or possibly reactivated by intense and localized meteorological events, whose frequency and severity are increasing in relation to climate change.

In this scenario, monitoring unstable slopes and understanding the dynamics, that link precipitation with landslide kinematics, become fundamental for risk mitigation and land management. In May 2023, between the 1st and 17th, two meteorological events of extraordinary intensity affected large areas of Emilia-Romagna, generating a significant number of gravitational movements which caused serious damages to infrastructure, environment and local communities. This highlighted, once again, the vulnerability of some territories and the need to deepen the relationships between rainfall conditions and the mechanical response of the slopes.

This thesis focuses on the analysis of a specific landslide that occurred in the Modigliana municipality, located in the Forlì-Cesena province. After an initial general overview of the phenomenon, incorporating a detailed characterization of the meteorological conditions that triggered it and the resulting impacts on the territory, the geological context of the area involved is outlined, paying a particular attention to the lithostratigraphic and structural features of the slope. Subsequently, the landslide monitoring systems currently employed along the slope is reviewed, with specific reference to the correlation between rainfall and landslide movements.

Result obtained from the different monitoring techniques, which include a weather station, extensometers, reflectors and a GPS system, are critically analysed, enabling a comparative assessment of the different techniques, to evaluate their potential, limitations and possible complementarities.

The aim of the thesis is to provide a useful cognitive contribution to the understanding of the activation and evolution processes of landslides in Apennine contexts, through an integrated approach that combines direct field observation and high-resolution instrumental monitoring. The findings are expected to provide a robust scientific basis for subsequent research and the development of more effective strategies for hydrogeological risk management.

1. Frameworks of May 2023 events

1.1 Study area

The province of Forlì-Cesena covers an area of approximately 2,378 km², Figure 1. It extends across the south-eastern part of Emilia-Romagna region, characterised to the north by the presence of the Po Valley, a predominantly flat area, and to the south by the Tosco-Romagnolo Apennines. Only a small portion of it overlooks the Adriatic Sea to the east.

From a geological perspective, the central hilly belt consists of Pliocene and Miocene sedimentary substrates made of clay, marl and sandstone, soils of incoherent nature. Exactly due to these, widespread instabilities are recorded throughout all the examined area. Instead, rocks of sedimentary origin from the Mesozoic and Cenozoic eras, along with outcrops of limestone, sandstone and clay schists, make up the reliefs of the Northern Apennines, forming peaks that exceed 1,200 meters. These lithotypes, in combination with the high steepness of the slopes and the intense meteoric activity, made the area particularly vulnerable to landslides and gravitational mass movements.

The southeastern part of the province presents a temperate humid climate that entails hot summers with subcontinental-like tendencies towards the hinterland and maritime influences along the coast (classified as Cfa according to the Köppen climate system). Average annual temperatures fluctuate depending on altitude and distance from the sea. In flat areas they differ between 13-14°C, while in the Apennines they can drop to 10°C. Summers are characterized by high temperatures that exceed 30°C during the day in July and August, especially in the interior. In contrast, winters exhibit cold but moderate conditions, in fact temperatures in the plain fall below zero during December and February.

The annual precipitation regime does not exhibit a uniform distribution across the territory since they are dependent on altitude and exposure to moist air masses. Throughout the year, in the Apennine region, total average precipitation ranges from a maximum of 1,400 mm to a minimum of 1,200 mm, while downstream, rainfall varies from 700 mm to 800 mm per year.

Figure 1. Borders of the province of Forlì-Cesena.

Therefore, the hilly area receives significantly higher rainfall than the plains and coastal areas. In the seasonal cycle two relative peaks in precipitation distribution can be identified, one between October-November and the other between April-May, and two minimums in the summer and winter periods. Statistics confirm that November is often the wettest month, while July is the driest one. Generally, annual rainfall fluctuations in the Forlì-Cesena area are linked to extensive atmospheric movement systems, such as Mediterranean cyclonic paths and broader European climatic irregularities. This diversity in rainfall distribution is important for understanding hydrological reactions, slope equilibrium conditions and geomorphological changes within the province, especially in the southern Apennine areas.

1.2 Meteorological context of the extreme events

Between 1 and 3 May, a polar trough created a low-pressure system over the central Tyrrhenian Sea, Figure 2, which remained nearly stationary due to the blocking of a promontory over eastern Europe. The associated cyclonic circulation favoured the influx of humid southeastern air from the Adriatic sector and colder northeastern currents, generating widespread and persistent precipitation across the region. Interaction with the Apennine relief intensified precipitation on the windward side, with accumulations exceeding 200 mm between Modena and Romagna. The rainfall, predominantly stratiform and moderate in intensity (2–4 mm/h), lasted approximately 48 hours, until gradually improving on May 3rd due to the advance of the western promontory.

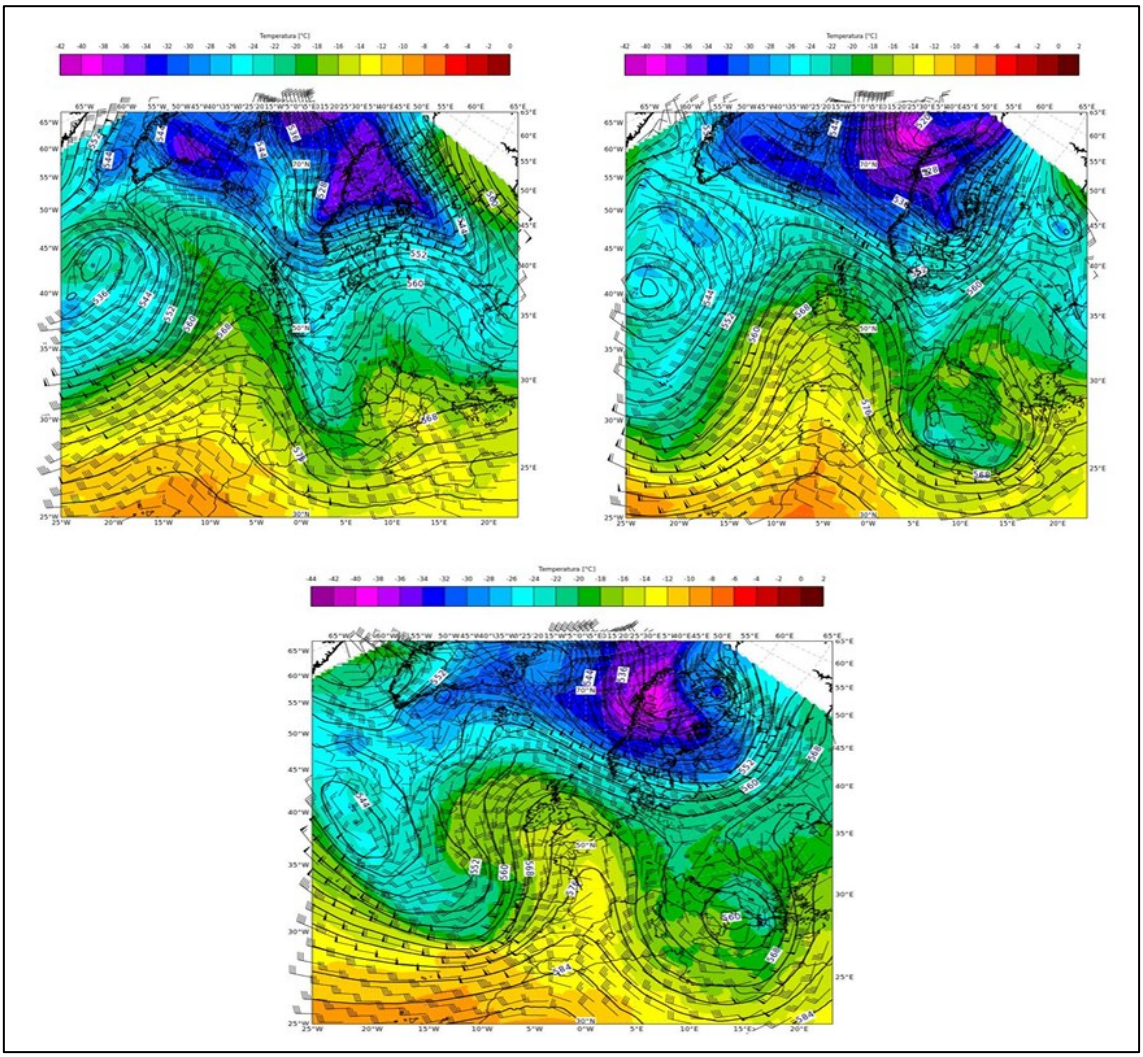

Figure 2. Geopotential, temperature and wind analysis map at 500 hP from the IFS-ECMWF model at 12 UTC on 1 May 2023 (top left) and at 12 UTC on 2 May 2023 (top right) and at 12 UTC on 3 May 2023 (bottom center).

On 15 May morning, the European synoptic scene was dominated by the presence of an anticyclone, located precisely between the Atlantic Ocean and the Iberian Peninsula. To the east, however, a promontory extends which rises north from the Mediterranean. Between the pressure structures there was a trough that feeds a depression vortex between Tunisia and Sicily designated, by the Italian Air Force Meteorological Service, “Minerva”. The latter had generated the instability that has affected the Emilia-Romagna region.

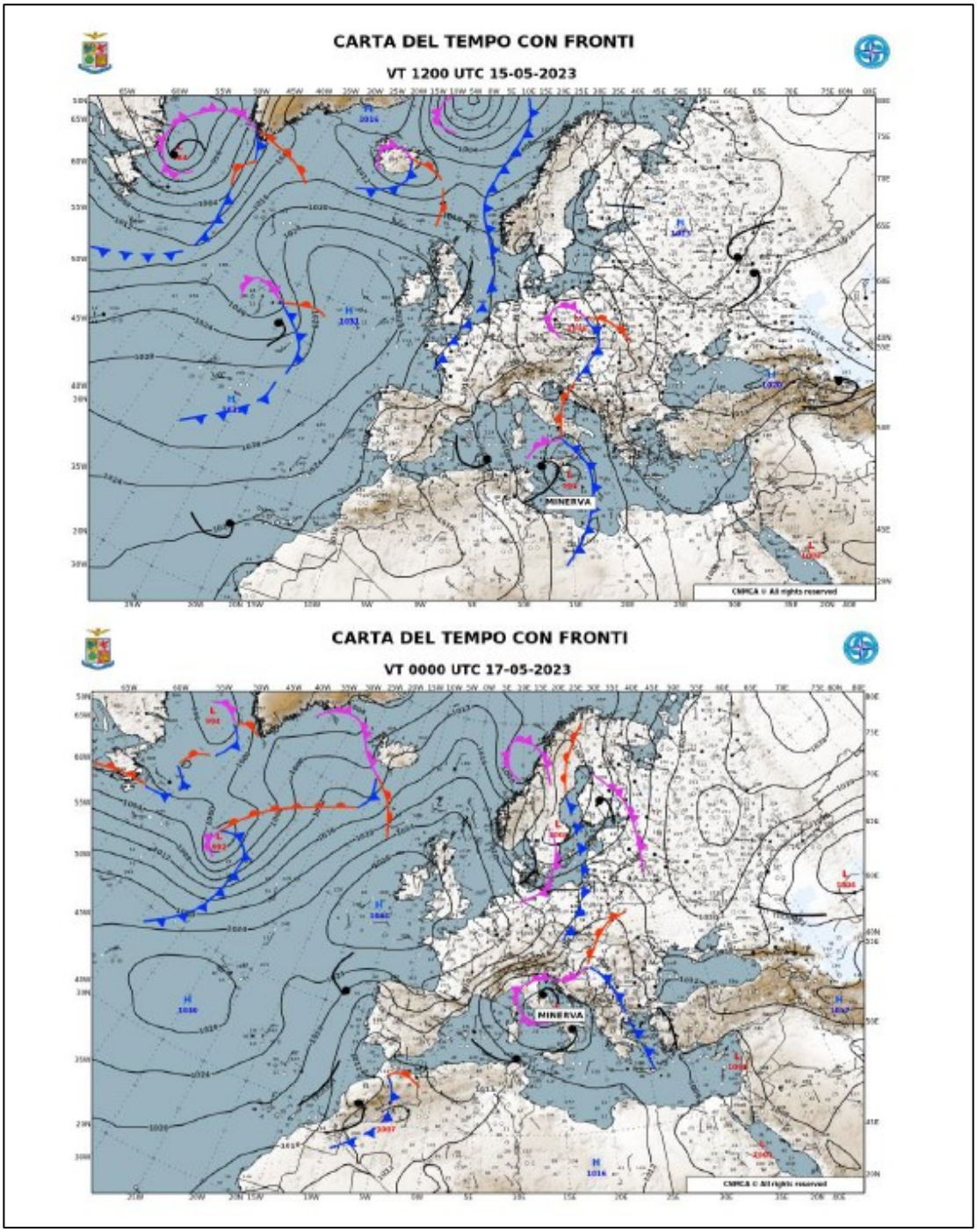

Figure 3. Weather map with fronts, showing the surface pressure values and the synoptic subjects identified on the Euro-Atlantic scenario, at 02 (00 UTC) on 15 May (top) and at 02 (00 UTC) on 17 May (bottom).

A strong cyclonic circulation intensified as the low-pressure vortex moved towards central Italy, causing a significant shift of moist air masses from the south-eastern Adriatic and channelling strong low-level winds towards the northern Adriatic basin. The interaction between these distinct air flows, as well as convergence near the surface over the Romagna area, enhanced uplift mechanisms on a mesoscale, thus facilitating the development of intense precipitation, including convective rain cells. The cyclonic core remained almost stationary over central Italy, continuing to bring humid air towards the Po Valley and maintaining constant rainfall, especially central-eastern Italy. The extraordinary intensity of this synoptic configuration is demonstrated by its long duration, followed only by a gradual attenuation of both the intensity of the vortex and the continuous convergence of moisture along the northern side of the Tuscan-Emilian Apennines. Under these conditions, the heavy rain was mainly caused by orographic lifting and forced ascent, despite the absence of the strong atmospheric instability commonly associated with convective events. In the final phase of the event, between 13:00 and 15:00 local time on 17 May, the precipitation changed to intermittent rain, mainly light to moderate, which gradually decreased in the central part of the region, as shown in Figures 4 and 5.

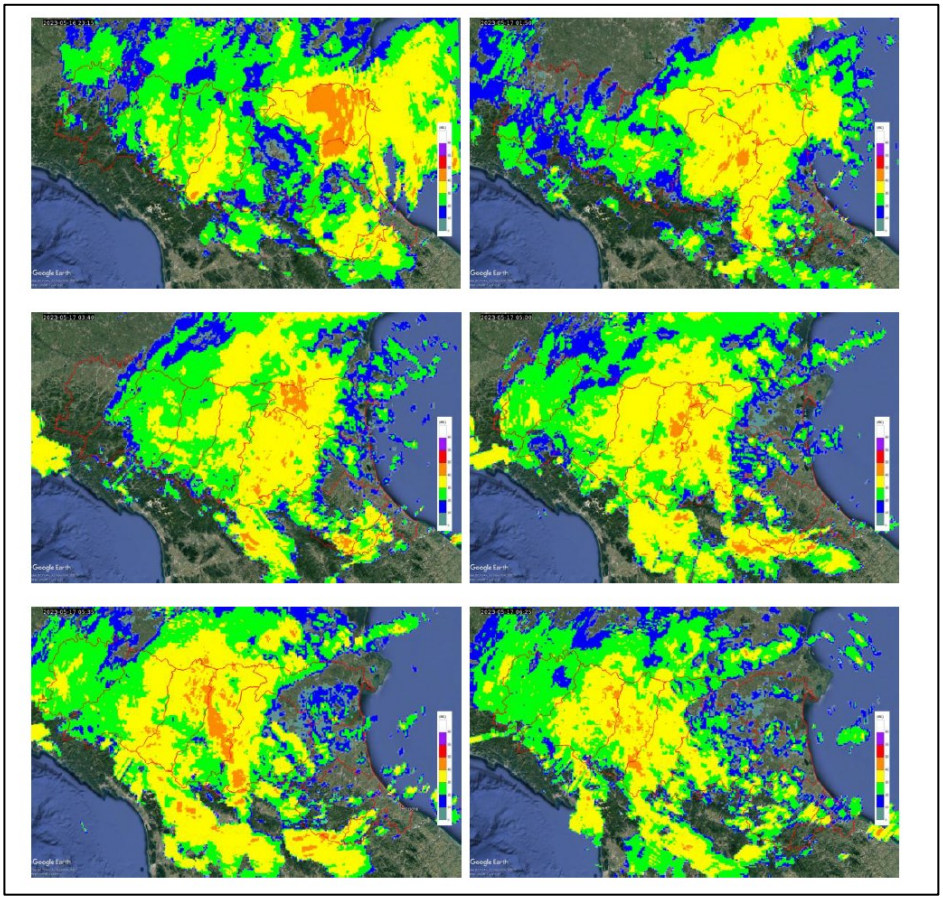

Figure 4. Radar composite reflectivity maps for May 17 at 01:15 (23:15 UTC 16/05/2023) top left, 03:50 (01:50 UTC) top right, 05:40 (03:40 UTC) center left, 07:00 (05:00 UTC) center right, 07:35.

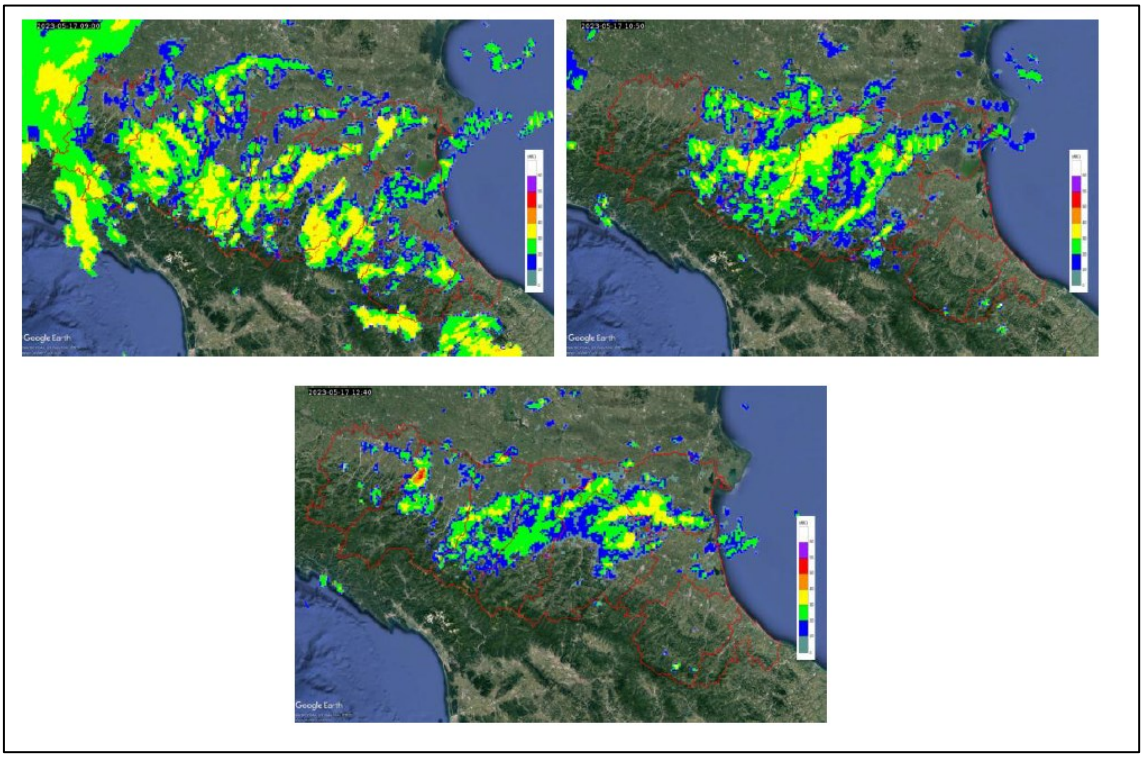

Figure 5. Radar composite reflectivity maps for May 17 at 11:00 (09:00 UTC), top left, 12:50 (10:50 UTC), top right, and 14:40 (12:40 UTC), bottom.

1.3 Framework of the rainfall events and occurred landslides

Intense rainfall that widely affected May 2023, can be distinguished into two distinct events: the first one between 1 and 3 and the second one between 16 and 17. At the onset of the first event, low cumulative rainfall values were recorded during the initial phase, then increased considerably on the second day, during which cumulative daily rainfall values above 100 mm were measured in some areas of the region central-eastern sector, ad depicted in Figure 6. Although these magnitudes do not reach the maximums recorded in recent years this episode stands out for its duration and the extent of the affected territory.

DAY	PREC (mm)	STATION NAME	MUNICIPALITY	PROVINCE	BASIN
1	55.4	Trebbio	Modigliana	FC	Lamone
2	187.6	Trebbio	Modigliana	FC	Lamone

Table 1. Daily precipitation on 1st and 2nd, May 2023 in the province of Forlì-Cesena, near the landslide.

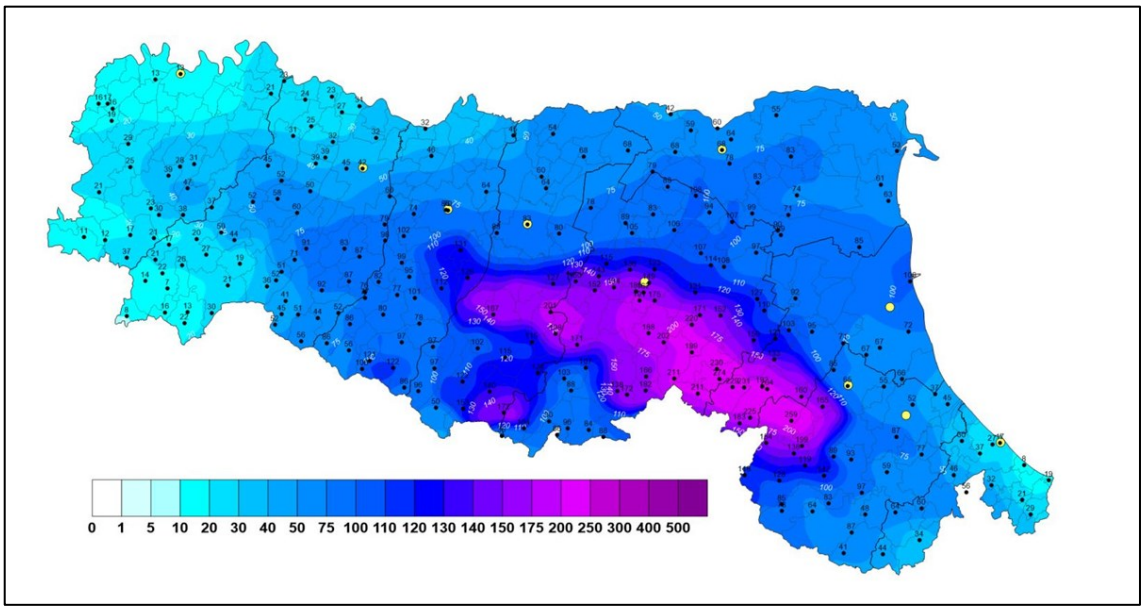

Figure 6. Cumulative precipitation observed in the event from 1st to 3rd May 2023, with indication of the specific values and the boundaries of the municipal territories

In particular, the Trebbio (Modigliana municipality) monitoring station recorded 55.4 mm on 1st May and a further increase to 187.6 mm on 2 May, as shown in Table 1.

This sharp increase in the amount of rainfall over a short interval represents significant hydrological stress on the slope, in line with the instability mechanisms caused by saturation.

The event that occurred on 16 and 17 May broadly affected Emilia-Romagna region, exhibiting exceptional rainfall both in terms of intensity and territorial extent involved.

PREC (MM)	STATION NAME	MUNICIPALITY	PROV.	BASIN
205,6	Trebbio	Modigliana	FC	Lamone
167,3	Castrocaro	Castrocaro Terme e Terra del Sole	FC	Montone
158,6	Monte Grosso	Rocca San Casciano	FC	Montone
157,9	Tredozio	Tredozio	FC	Lamone
151,4	Civitella	Civitella di Romagna	FC	Ronco
144,4	S. Paola	Roncofreddo	FC	Rubicone
137,4	Roversano	Cesena	FC	Savio
135,2	Voltre	Civitella di Romagna	FC	Ronco
129,8	Rullato	Civitella di Romagna	FC	Savio
128,2	S. Zeno	Galeata	FC	Montone
126,4	Premilcuore	Premilcuore	FC	Savio
122	Cusercoli	Civitella di Romagna	FC	Ronco
121,2	Capaccio	Bagno di Romagna	FC	Ronco
118,6	Pratacci	Portico e San Benedetto	FC	Montone
114,8	Corniolo	Santa Sofia	FC	Ronco
113,2	Martorano	Cesena	FC	Pianura tra Savio e Rubicone
106,8	Lastra	Bagno di Romagna	FC	Ronco
101,4	Montriolo	Santa Sofia	FC	Ronco
99,4	Ponte Braldo	Forlì	FC	Montone
97,0	Corsicchie	Bagno di Romagna	FC	Savio
96,6	Diga di Ridracoli	Bagno di Romagna	FC	Ronco
92,4	Lama	Bagno di Romagna	FC	Ronco
88,4	Monte Iottone	Mercato Saraceno	FC	Savio
87,1	Vergherato	Vergherato	FC	Savio
86,4	Forlì Urbana	Forlì	FC	Ronco
85,6	Diga di Quarto	Sarsina	FC	Savio
77,0	S. Maria Nova	Bertinoro	FC	Bevano
72,0	Mesola	Cesenatico	FC	Pianura tra Savio e Rubicone

Table 2. Daily precipitation >70 mm on May 16, Forlì-Cesena province.

Cumulative precipitation on 16 May largely exceeded 100 mm, with daily peaks of 205.6 mm at the Trebbio station and 196.8 mm at the San Cassiano station (municipality of Brisighella, Ravenna), both located in the Lamone basin. Table 2 reported all stations that recorded a daily precipitation greater than 70 mm on May 16th (data has been validated). Precipitation on 17 May was generally lower, as the event subsided in the afternoon. A spatial analysis of total precipitation over the two days highlights a strong concentration of rainfall peaks along the central-eastern Apennine range, with measurements exceeding 250 mm in several locations: 260.8 mm in Monte Albano (Senio basin), 254.8 mm in Trebbio, and 254.6 mm in San Cassiano (Lamone basin). Even more western areas, such as Modena and Ferrara, recorded significant, albeit lower, values. The significance of this event is clear from a detailed examination of extreme rainfall data, measured over various time periods (1, 3, 6, 12, 24 hours, and even 2 days). This analysis was conducted using the GEV (Generalized Extreme Value) distribution, and the results obtained were compared with those derived from the TCEV (Two Component Extreme Value) distribution. The data shows return periods exceeding 200 years for intense 24-hour rainfall events at various stations located in the Santerno, Senio, Lamone, Montone, and Ronco river basins. It is worth noting that most intense events recurred: the rainfall of 16 and 17 May hit the same areas already affected by a previous, equally intense event between 1 and 3 May 2023. On that occasion, the two-day rainfall accumulated broke previous records at more than half of the stations in the hilly areas of Bologna, Ravenna and Forlì hilly areas with return periods exceeding 100 years at many stations in the Idice, Sillaro, Santerno, Senio, Lamone, and Montone basins. Between May 1st and 17th, several further light showers and thunderstorms occurred, contributing to an unprecedented total accumulation: 80% of the rain gauges located in the basins between the Samoggia and Ronco rivers recorded cumulative values above 300–400 mm, with maximums of 609.8 mm in Trebbio and 563.4 mm in Le Taverne (Fontanelice, Santerno basin). In a regional scale, the average cumulative precipitation in the period 1st–17th May reached 221.4 mm. In some areas, rainfall reached 60% of the annual average, emphasizing the serious hydro-climatic impact of the event, as reported in Figure 7.

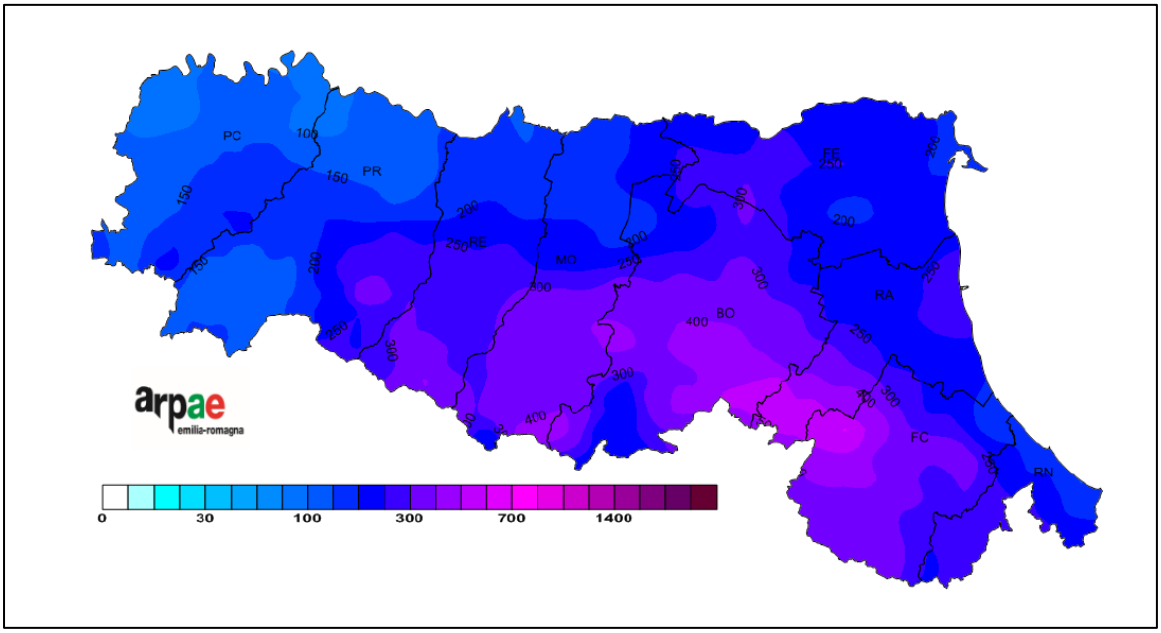

Figure 7. Cumulative precipitation of May 2023.

In response to the sever pluviometric event described above, Emilia-Romagna was widely affected by numerous slope failures. The most impacted areas were the provinces of Bologna, Ravenna, and Forlì-Cesena, while Reggio Emilia, Modena, and Rimini were less affected, though still significantly. The frequency and distribution show a notable correspondence, predictably, with areas where the most intense rainfall occurred: the most affected sectors concerned the hilly areas and the low-altitude mountains between the Reno and Setta valleys in the Bologna area and those of Bidente and Savio in the Forlì area. These landslides aggravated an already precarious situation, adding to those triggered at the beginning of the month. The observed landslides can be classified into three main types: earth slides, earth flow and mud flow.

A total of 65,598 landslides were recorded, affecting a total area of 72,21 km². Most of them were small, averaging 1.100,9 m², specifically, the smallest landslides numbered 47.556, representing 72.5% of the total, while the largest, exceeding 1 hectare (10.000 m²), amounted to 576. The landslide affected six out of nine provinces: Reggio Emilia, Modena, Bologna, Ravenna, Forlì-Cesena, and Rimini, as reported by Figure 8.
The most vulnerable geomorphological areas are those characterised by sandy substrates or sequences composed of sandstone and marl, i.e. soils essentially formed by mechanically cohesive sandstones alternating with marls with varying degrees of cementation. These lithological assemblages belong to the Marnoso–Arenacea Formation, whose stratigraphic and geomechanical properties make slopes highly susceptible to landslides and surface instability processes under conditions of intense and

prolonged hydrological stress. In contrast, the area of the Emilia-Romagna Apennines is characterized by clayey soils, common in the Ligurian and some epi-Ligurian geological units, normally prone to frequent landslides, especially during the rainy season, suffered less damage in this circumstance. The difference in response to meteorological phenomena is attributable to a combination of geological and morphological factors, in particular the lithological composition, slope gradient and soil permeability. This is supported by an original, manually mapped inventory produced in 2023 by Maria Francesca Ferrario and Franz Livio. The new dataset produced contains 47,523 landslides within the Forlì-Cesena province, mapped using pre- and post-event satellite imagery with the addition of limited on-site surveys. Some predisposing factors such as rainfall, slope, land use, lithology, and distance from roads were analysed. It was found that there is a strong correlation with steep slopes and some land use categories, while a weaker positive influence is found with respect to lithology.

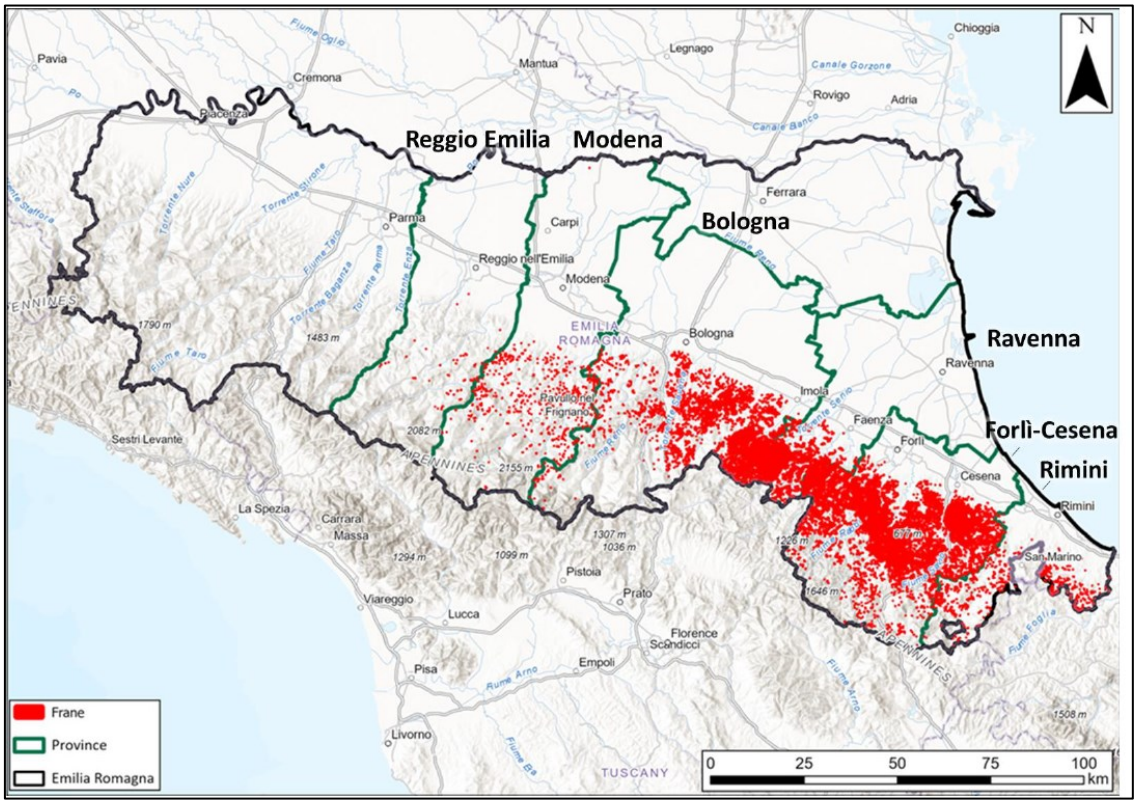

Figure 8: Geographic distribution of landslides inventoried by the Emilia-Romagna Region.

1.4 Geology of the area

From a geological-structural standpoint, the Emilia-Romagna Apennines owns a complex configuration, Figure 9, consisting of various superimposed units, several of which are allochthonous and composed of well-defined stratigraphic characteristics. Among these, the Ligurian Domain stands out as particularly significant and is placed in a stratigraphically higher zone, extending extensively between Pavia and Bologna. Dating back to the period between the Upper Jurassic and the Lower Eocene, the Ligurian formations encompass the Scaly Clays, also defined as "tectonic *melanges*": chaotic complexes of heterogeneous lithological fragments submerged in a clay matrix intensely deformed by tectonic processes. These formations have a high clay content and poor cementation; therefore, they are often subject to instability phenomena, weathering and water swelling. Above the Ligurian geological structures, turbidite sedimentary layers are present, composed of limestone and/or sandstone. All layers, generally less subject to deformation, are dated between the Upper Cretaceous and Lower Eocene. The most important formations include Upper Cretaceous Ligurian Flysch, Helminthoid Flysch, and Ligurian Tortonian Flysch. These formations appear as thick and stratified slabs, with less pronounced deformations than the previous ones but still susceptible to instabilities, especially along the slopes. The Epiligurian succession lies above the Ligurian units, delimited by a tectonic contact. It is primarily composed of resistant sandstones, well-organized into layers, slightly folded, and characterized by high mechanical strength. However, mixed layers of clay and breccia, reminiscent of the underlying melange, can trigger extensive or complex landslides.

In the eastern part of the Apennine chain, the Marnoso-Arenacea Formation extends over a wide area, originating during the turbidite cycle of the lower and middle Miocene. This formation is composed of a succession of alternating of marl and sandstone layers, which often appear well-stratified but sometimes deformed. This geological formation plays a key role in the development of deep landslides and localized erosional phenomena, when the strata are arranged downward. The most numerous landslides documented in the area are those characterized by a velocity ranging from rapid to extremely rapid. Furthermore, deeper slides of both rotational and translational nature were observed. Another rather widespread type of landslide are mud, earth or debris flows, which developed preferentially on clayey substrates, in this case belonging to the Ligurian Domino. Rockslides and composite landslides have been found in correspondence with the Ligurian Flysch, which, due to their intensely fractured arenaceous-pelitic alternations, are predisposed to the development of deep failures.

Keeping in mind this geological context, the rocks constituting Landslide 1 - Via lago, in Modigliana fall from a lithostratigraphic point of view, within the Modigliana Member, a well-defined sub-unit belonging to the Marnoso-Arenacea Formation previously introduced. A more comprehensive characterization of the landslide slope will be presented subsequently.

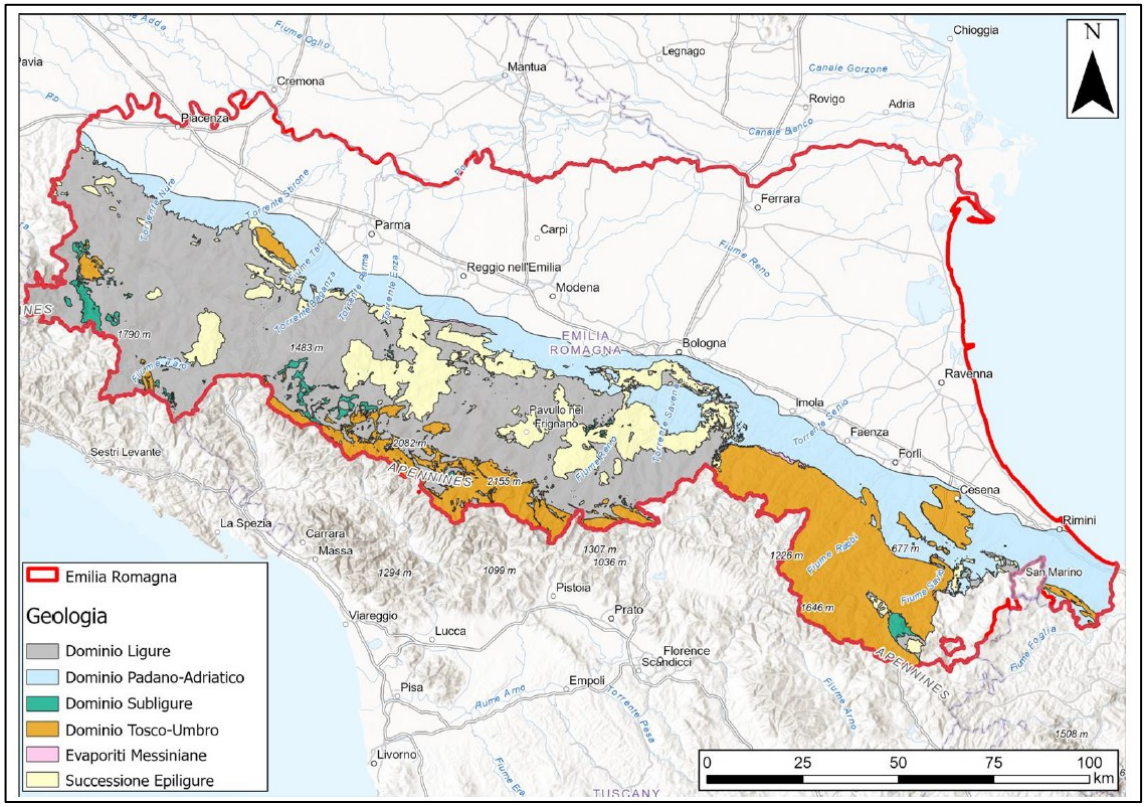

Figure 9: Map of the Geological-Structural Domains of the Emilia-Romagna Region - General Directorate for Land and Environmental Care, Land Protection Sector.

1.5 Introduction to landslide monitoring systems and rainfall-landslide correlations

Landslide monitoring is a mandatory step within the broader context of landslide risk assessment and management. This phase provides the necessary evidence to fully understand the triggering factors, mechanisms, and potential short and long-term developments. In fact, monitoring activities have the primary objective of collecting and analysing temporal and spatial features, as areal extent, speed of movement, surface topography, soil humidity, failure surface data that reveal how landslides can behave under different environmental and geotechnical conditions.

Recently, the constant development of new technologies in the methodological and instrumental fields allowed to develop multiple monitoring systems which can be classified according to different criteria. Below, a classification based on data acquisition method is proposed. The complete breakdown is shown in Table 3.

Remote sensing includes a series of techniques that allow to collect information about the Earth surface through various methodologies that do not require physical contact, by analysing the electromagnetic radiation reflected by the observed elements.

To investigate the physical properties of soil, geophysical techniques are used providing indirect, but detailed, information on the internal structure, composition and behaviour of the constituent materials.

Geotechnics include approaches used to directly observe the mechanical and hydraulic properties of soils and structures in the field. These tools enable both point and continuous measurements, essential for studying slope stabilities, foundations and public infrastructure.

Other techniques that can be apply are GNSS (Global Navigation Satellite System), satellite techniques used to accurately establish a geographic position, and Core Logging or the extraction of soil or rock cores. The techniques used to monitor the Modigliana landslide will be explained in detail later.

Following the data collection phase and subsequent in-depth analysis, it will be possible to more precisely define the relationship between rainfall trends and the information obtained from the various monitoring systems installed across the territory. The primary objective of this analysis is to understand the extent to which rainfall variability influences the parameters measured by the sensors and whether these systems can respond consistently and promptly to meteorological events.

Furthermore, the analysis process is not allowed only to establish whether the monitoring systems respond effectively to rainfall, but also to identify the technology best suited to the needs of the study context, thus promoting a general improvement in management and interpretation of environmental data.

Category	Subcategory	Description	Main applications
Remote Sensing	Passive optical sensors	Measure the natural emission of Earth surface (e.g. photographs, satellite images)	Land use, landslides, vegetation, environmental monitoring
	Active optical sensors	Generate their own energy emissions which then is measured back after reflection (ALS, TLS, EDM)	DTM (Digital Terrain models), topographic surveys, deformations
	Active microwave sensors	Radar antennas with fixed or synthetic aperture (InSAR, PS, GBInSAR)	Millimeter-level monitoring of landslides, subsidence, volcanoes
Geophysics	Ground-Based	Electromagnetism, micro-seismicity, etc.	Fractures, faults, structural monitoring
	Airborne	Aircraft detection (electromagnetic, gamma-ray)	Geological mapping, mineral exploration, contamination
	Offshore	Multibeam, 3D seismic	Seabed, offshore tectonics, sedimentology
Geotechnics	Exstensometer	Measures the variation in distance between points (wire, probe, fixed)	Deformations in landslides and dams
	Inclinometer	Measures inclinometer displacements in the ground (probe, in-place)	Stability of slopes, embankments, structures
	Other geotechnical instruments	Piezometers, contact pressure cells	Pore pressure, stress in soils
Other	GNSS	Satellite positioning system (differential, RTK)	Costal deformations, surface movements
	Core Logging	Extraction and visual/geotechnical analysis of soil/rock cores	Stratigraphy, mineralogy, discontinuities, geotechnical properties

Table 3. Monitoring methods categorized by data acquisition technique.

2. Materials and methods

2.1 Landslide 1 - Via Lago Characterization

Landslide 1 – Via Lago, outlined in Figure 10, is a landslide that occurred in the Modigliana municipality during the intense rainfall event, discussed extensively previously, recorded between 1 and 2 May 2023. The landslide appears to be a slippage of a sheet-like rock block with a thickness of approximately 6-7 metres which generated a rapid mass movement at a speed of a few metres per second, data supported by geomorphological evidence. The entire landslide body travelled about 75 m towards the valley bottom, blocking the riverbed of Rio Signano. A distinctive feature of this phenomenon is the substantial integrity of the mobilized mass: no signs of dynamic fragmentation or disintegration, typical of high-energy rockslides or collapses, are observed. The absence of internal deformations suggests rigid kinematics along a pseudo-planar sliding surface, currently unexposed because it is covered by chaotic detrital deposits. Considering the total area involved, nearly 5.500 m^2, and the almost constant thickness, the volume of the main body has been estimated between 30.000 and 40.000 m^3, to which should be added 5.000–10.000 m^3, deriving from small secondary landslides and from deposits present between the detachment zone and the landslide body. Coinciding with the same rainfall event, a second landslide was triggered exhibiting a mechanism similar to the first one in the upper part of the slope. Its detachment zone widened towards the north-west by 400 m, forming a trench 5-10 meters wide and 5–8-meters depth. Moreover, the second rainfall event triggered a third landslide, albeit smaller, located halfway up the slope on the southern side of Via Lago characterized by a drop of 6 m. These occurrences together highlight the slope's marked sensitivity to intense precipitation and suggest the presence of deep layers prone to failure, influenced by the geological and geomorphological conformation of the area. This kind of structure contributes to the frequent precariousness of the entire zone, making the slope extremely vulnerable.

A relevant consequence linked to the disaster was the damage to a gas pipeline, which was impacted by the landslide. Following the interruption, Snam Rete Gas S.p.A, a leading European gas infrastructure operator, implemented a temporary diversion to ensure service continuity.

The project "METANODOTTO AREZZO - MINERBIO: VARIANTE DEFINITIVA FRANA 1 IN COMUNE DI MODIGLIANA (FC)" has finalized the creation of the methane pipeline 6101008 Met. Arezzo – Minerbio DN 1050 (42"), MOP 75 bar variant, using trenchless technology. In this way, the constructed deviation allows for the safe crossing of Frana 1.

Another important factor to consider is the upper trench opening may indicate the initial stage of a landslide with characteristics similar to Frana 1 but of larger magnitude. The maximum possible scenario could mobilize a total volume of up to 4.000.000 m^3 of soil with a thickness ranging from 5 to 10 m. To investigate this possibility, the University of Florence, with the assistance of the Civil Protection Competence Centre, has developed a new numerical model based on the hypothesis that trench formation is completely independent of the detachment at the base of the slope. Instead, it appears be associated with a specific stratigraphic condition and tensile stresses that developed in the slope during the rainfall event between the 16 and 17 of May.

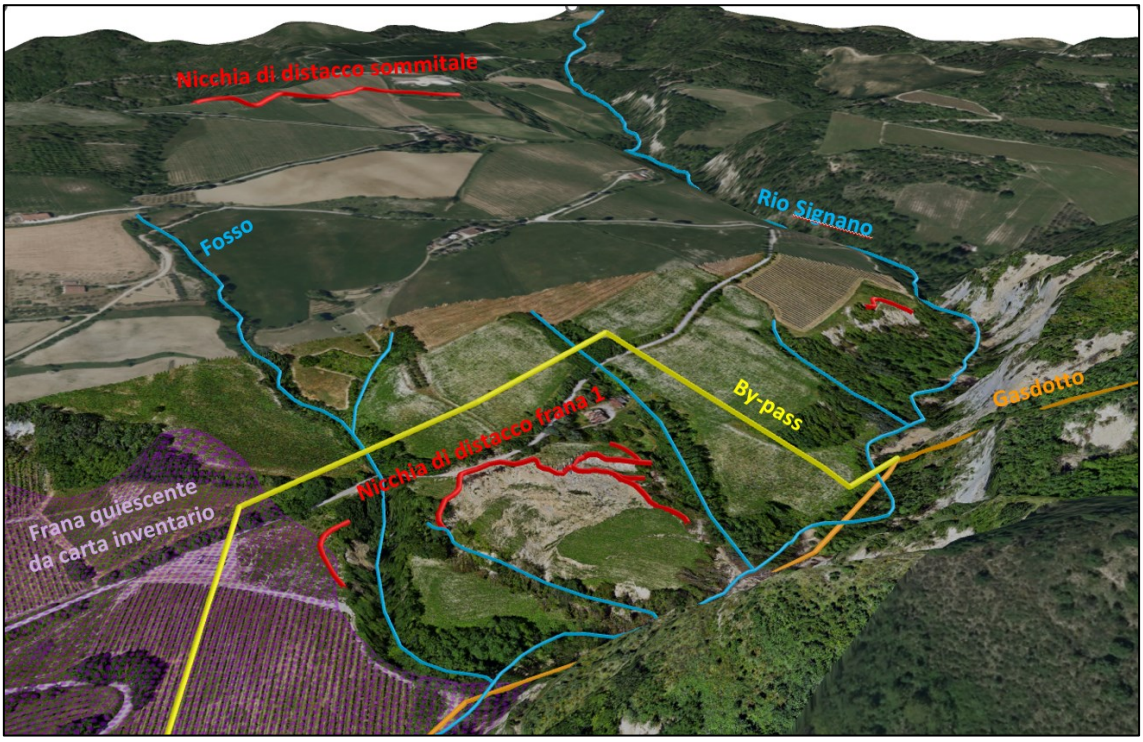

Figure 10: Landslide 1 – Via Lago landslide orthophoto.

To define properly the surrounding terrain affected by the landslide, Snam Rete Gas S.p.A has commissioned a series of geognostic surveys and two geophysical survey campaigns.

In addition, four continuous core drilling geognostic surveys were carried out at the points shown in Figure 11, to obtain information about the stratigraphic and lithological nature of the soil at the different depths investigated.

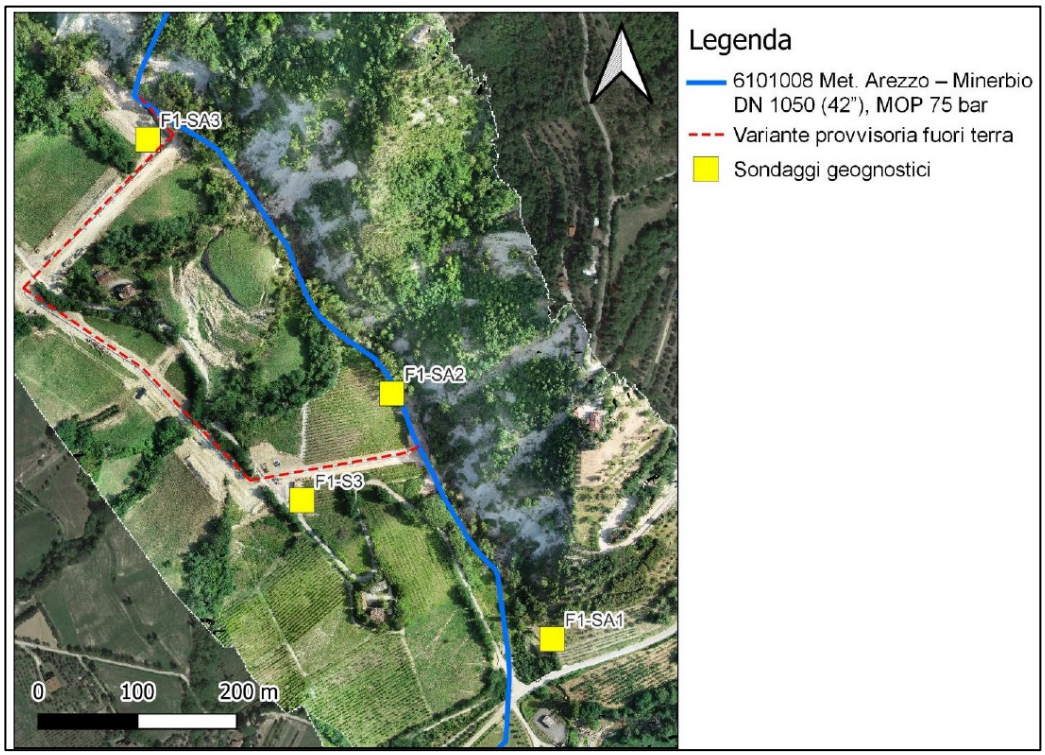

Figure 11: location plan with position of geognostic surveys.

Three geophysical surveys were also conducted, the last of which includes the following types of surveys:

- Electrical resistivity tomography (ERT): it allows to measure the distribution of electrical resistivity underground thorough a source that generates an electric current of a certain power to special electrodes embedded in the ground. By quantifying the electrical potential that is created and knowing the distance between the electrodes, it is possible to evaluate the apparent resistivity of the soil. In this case a multiple gradient array device was utilized.

- Seismic refraction tomography (SR): the various geophones of the array use the arrival time of P-waves (compression waves) to detect lateral and vertical velocity changes in the subsurface.

- MASW survey: Multi-Channel Analysis of Surface Waves or rather analysis the phase velocity dispersion of Rayleigh (R) type surface waves by means of seismographs.

- HVSR (Horizontal to Vertical Spectral Ratio) survey: it utilizes the effects of environmental seismic noise to identify resonance phenomena and the location of the local rigid substrate. Furthermore, noise measurements can be used to determine the properties of the medium.

The geophysical survey's location points are outlined in Figure 12 and 13.

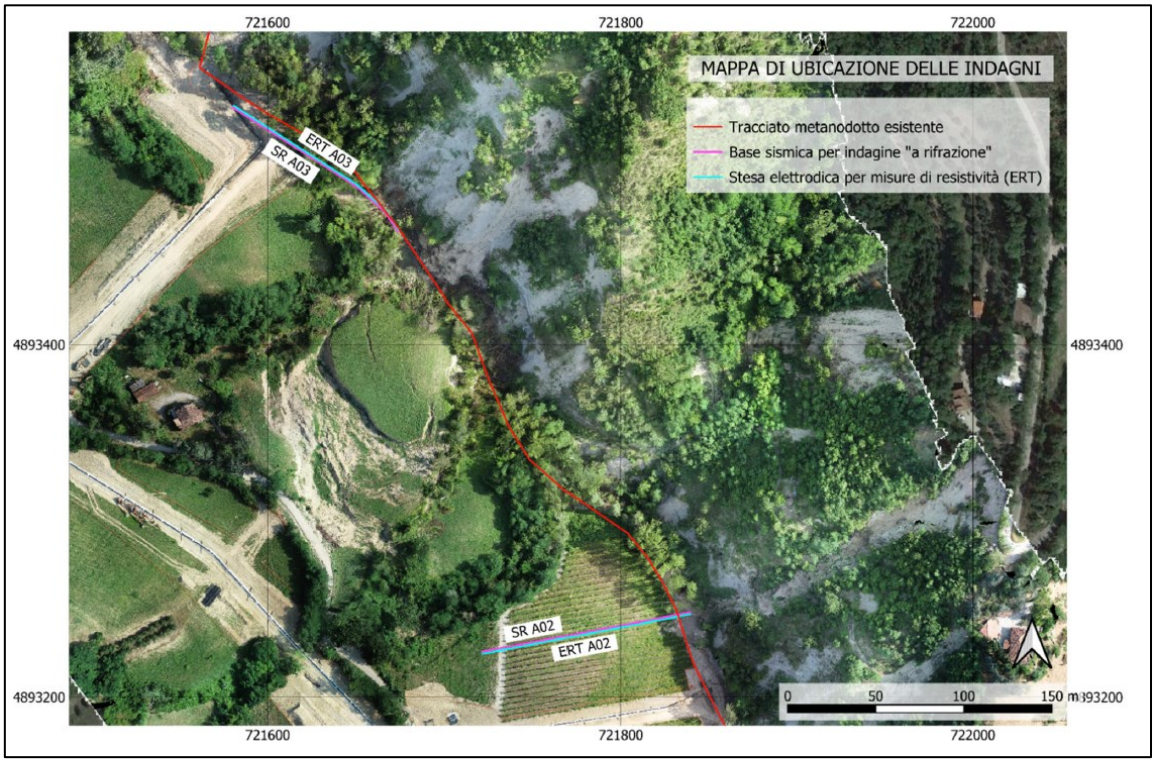

Figure 12: location plan with position of ERT and SRT surveys.

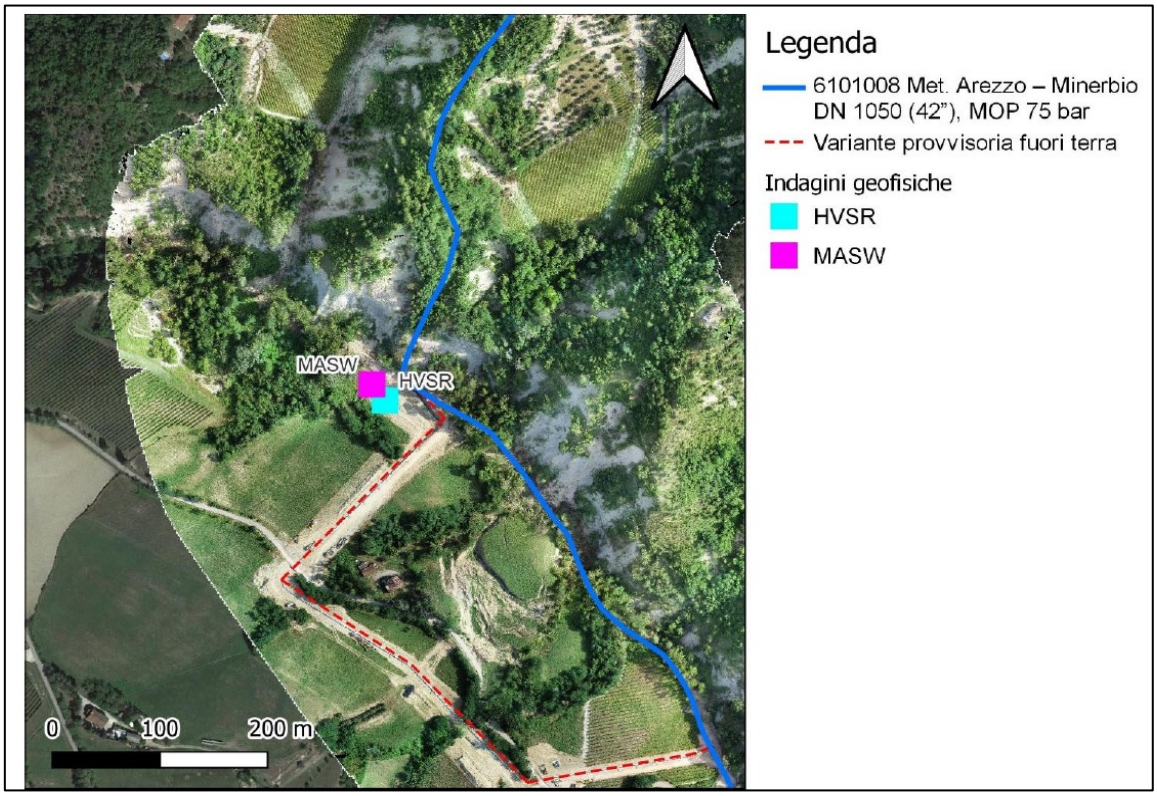

Figure 13: location plan with position of HVRS and MASW.

Geoelectric resistivity surveys confirm the presence of clayey marls, compact marly clays, and arenaceous marls, even from the processing in P and S waves shown a similar result. In addition, three sliding surfaces were identified.

The geophysical surveys conducted have provided significant information for understanding the geological and seismic composition of the area. To begin with, resistivity geoelectrical surveys enabled the developer an electro-stratigraphic map of the soil, facilitating the identification of the main resistivity areas and, consequently, the lithofacies analysis. The P and S waves velocities, crucial data for delineating the seismic stratigraphy of the sedimentary deposits, are estimate with the aid of seismic refraction studies. Thanks to the integration of the acquired data was possible to identify at least three slip planes within the slope, causing instability phenomena such as landslides and mudslides. These elements led to the classification of Frana 1 as a "complex" landslide, characterized by both rotational and translational movements. From a lithological point of view, it has been observed that the formations made up of marl and arenaceous marl present greater stability.

The results of the surveys commissioned are supported by the cartographic documentation available on the Emilia-Romagna Region geoportal and the explanatory notes on sheet 254 of the Geological Map of Italy, Figure 14. The geological map shows the presence of the Marnoso-Arenacea Formation, which extends across the entire area subject of research. From the same image it is possible to extrapolate important information regarding the slope of the layers and their orientation.

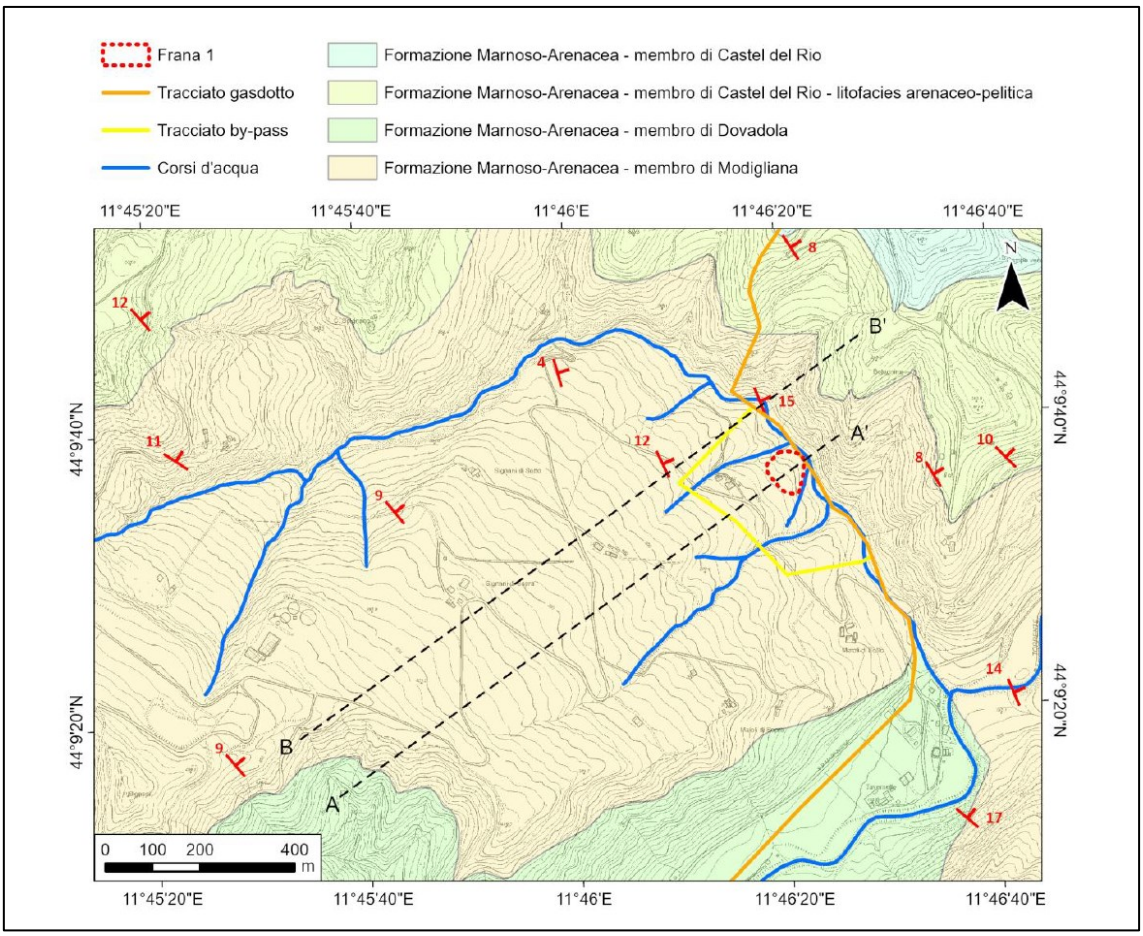

Figure 14. Extract from sheet 254 of the Geological Map of Italy, corresponding to the Via Lago slope.

The structural framework of the area highlights uniformly oriented bedding joints, characterized by a north-east slope, with gentle inclinations ranging between 9° and 15° along the BB' section, with overall values narrowed around an average of approximately 12°. This configuration allows us to consider the Via Lago slope as a pseudo-monoclinal system, in which the direction and inclination of the strata are primarily parallel to the conformation of the terrain. In this scenario, the origin of Landslide 1 can be attributed to the movement of a rock block along a sliding surface located on a weak layer, primarily clayey, saturated, and therefore mechanically unfavourable. This weak layer crosses the current morphology at the site where the Rio Signano streambed has undergone sustained erosive activity.

This erosion progressively increased the local slope steepness, creating conditions of geometric release at the base and compromising the stability of the area, to the point of favouring the activation of gravitational movement. From this configuration, it is possible to hypothesize the development of a generalized planar slide that would affect the entire slope, starting from the summit detachment zone. However, this catastrophic possibility has been refuted by some aspects observed in situ. Investigations carried out in the upper part of the slope have shown that the stratigraphy obtained are not compatible with those detected further downstream, thus denoting the non-continuity of the sliding surface, making a single and extensive planar kinematics difficult. Secondarily, in the approximately 200 meters downstream section, several undulations and uplifts of the ground can be observed, which can be interpreted as signs of compressive deformation. These morphological features appear more consistent with flexural-compressive behaviour of the material attributable to the lack of adequate geometric release at the base of the landslide body, rather than simple, constant planar sliding. This movement is called buckling failure, Figure 15, which denotes a local, almost-plastic deformation of the ground broken by tension upstream and folded by compression in the middle, without giving rise to generalized instability at low topographic gradient angles. This hypothesis is also supported by the local topography, which highlights bulges and deformations.

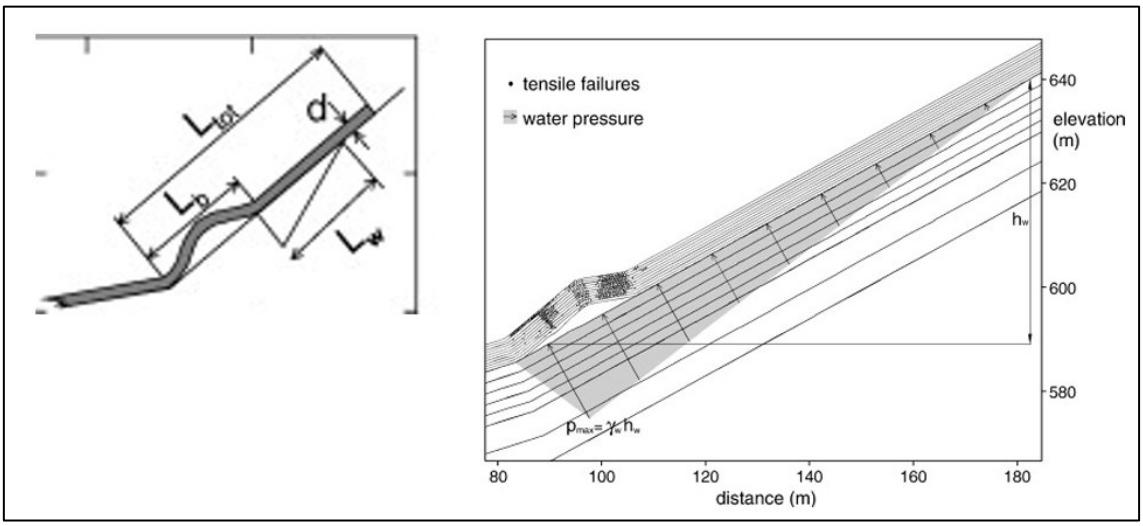

Figure 15. Schematic representation of a buckling failure (left) and the role of water pressures (right) in determining limit stresses (from Tommasi et al., 2009).

2.2 Monitoring system description

The Modigliana landslide monitoring project was implemented using a multi-technology approach, integrating topographic, geotechnical, hydrogeological, and meteorological instruments to ensure comprehensive and continuous monitoring of the phenomenon. The precise location of each individual device for every system type is reported thoroughly in Figure 16. The landslide complexity required the establishment of an instruments network capable of providing data on both surface movements and deep-seated deformations, as well as the hydraulic and environmental conditions that directly impact slope stability. The overall system is composed of several devices: topographic technologies (automated total station, reflectors, and GNSS network) which allow for high-precision measurement of potential surface slope movements, geotechnical and hydrogeological instruments (inclinometers, extensometers, piezometers) that permit for analysis of deeper movements and pore pressure fluctuations, crucial for understanding the dynamics and evolution of the landslide. To gain a more comprehensive understanding, a meteorological station monitors weather conditions, enabling correlation between rainfall events and slope reaction, while specific extensometers positioned along the pipeline ensure surveillance of critical infrastructure in the area. The simultaneous use of these various technologies offers a complete and multidisciplinary perspective on landslides, minimizing the uncertainties associated with the use of individual detection tools and increasing the ability to forecast and manage risk. The approach adopted also can record real-time updates of analytical models and warning systems.

.

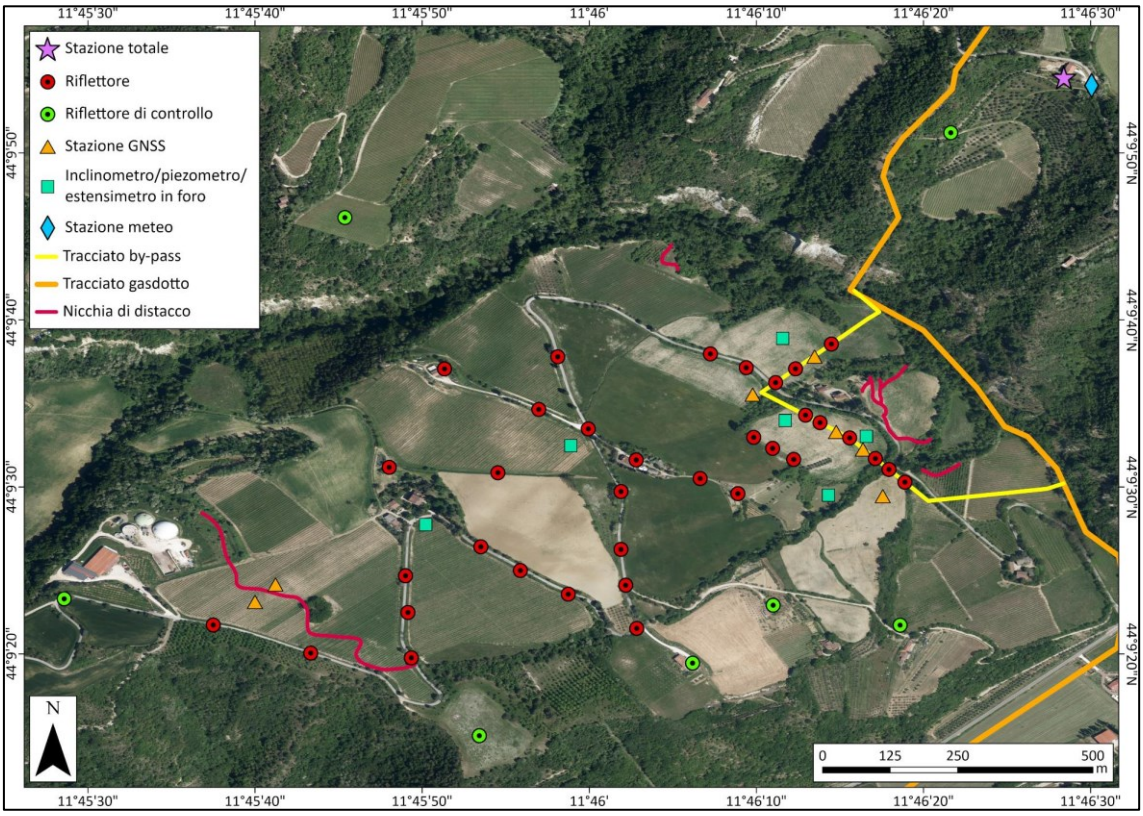

Figure 16. Location of the different monitoring systems.

A robotic total station is a topographic high-precision instrument capable of measuring distance with an IR distance meter, and zenital (vertical) and azimuth (horizontal) angles to a target from a known location. The automation of the instrumentation enables data acquisition without the need for an on-site operator, ensuring high temporal resolution and continuity over time. The targets, called also prisms, are made of various materials and sizes, however they are all made of reflective material that refocuses incoming IR and reflects it back to the station with high coherence and precision: distances (±1 mm + 1 ppm) and angles (0.5 arc seconds). This method has several advantages; indeed, it allows for the detection of three-dimensional displacements with great precision, and it is a proven and cost-effective technique thanks to the low cost of reflective prisms. Furthermore, data processing using the least squares method minimizes systematic errors, ensuring precise and reliable results. Using a total station has limitations, especially depending on the operating environment. When it rains, is foggy, or dusty, or if the reflecting prisms become dirty or slightly altered, surveying can be challenging. Furthermore, placing prisms at every point on the slope is not always possible due to organizational issues or hazards, and measurements do not provide immediate data between prisms.

Data accuracy is also affected by distance and weather, but some of the interference can be solved in post-production. In Figure 16 the total station is marked with a purple star while the 35 reflectors are marked with red circles, distributed evenly. The spatial distribution of the reflectors was planned to cover the entire slope, with particular attention to the zones most subject to possible movements. This grants to identify areas with uniform behaviour from those with independent or more rapid motions, facilitating the understanding of the fragmentation and complexity of the landslide phenomenon. These reference elements play a fundamental role in calibrating and monitoring the quality of data obtained from the total station, Figure 17. The presence of fixed targets empowers for the geometric stability of the survey network to be ascertained, isolating possible shifts due to instrumental or environmental factors, or measurement errors.

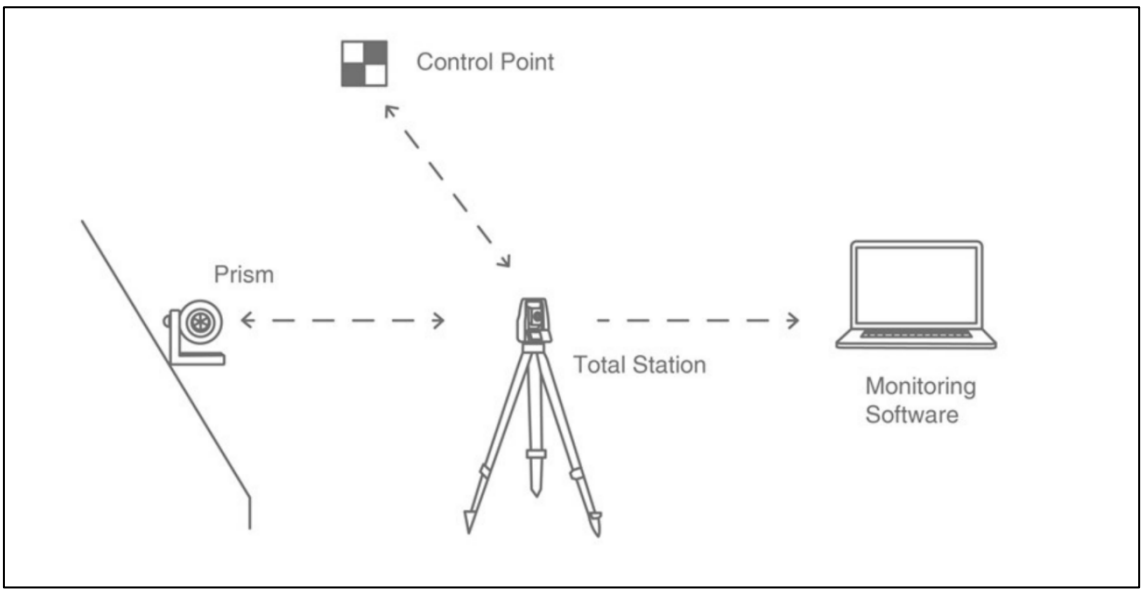

Figure 17. Schematic representation of the total station.

The GNSS (Global Navigation Satellite System) system, Figure 18, is employed for landslide monitoring as an alternative to direct measurements using a topographic total-station. It consists of a constellation of satellite in orbit that receive real-time positional data of a given point enabling precise geospatial positioning. The costs to install this system are still high due to the high precision required. Integrating GNSS data with measurement from automated total station allows for the develop of a more robust and complete deformation model, capable of reducing uncertainties and validating the reliability of the assessments. In total, 7 GNSS stations have been installed, marked by the orange triangles in Figure 16.

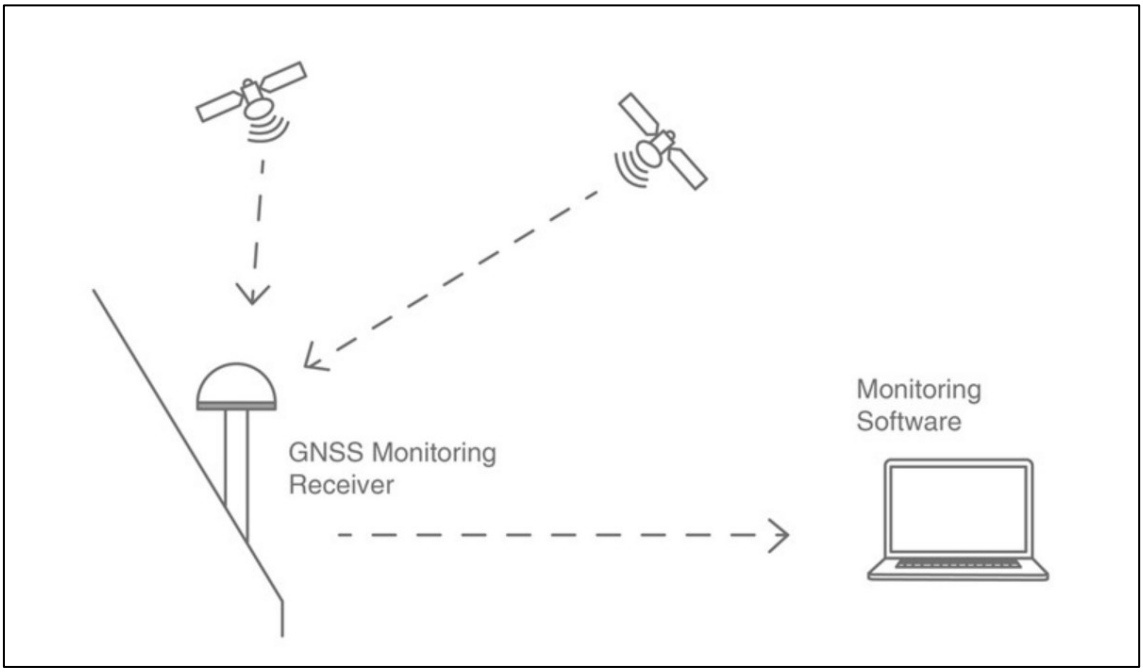

Figure 18. Schematic representation of GNSS system.

Automatic in-hole extensometers, Figure 19, are instruments designed to measure the relative displacement between two fixed points, typically with one located within the unstable zone and the other positioned in a stable area outside the landslide movement. The most recent models integrate digital data acquisition and telemetry systems, enabling continuous and automatic collection of displacement data. Their main limitation is that they provide only one-dimensional measurements, confined to the axis of the borehole or sensor cable, and that their range is limited, as excessive deformations can damage the instrument. Extensometers on the other hand offer several advantages: they are available in a wide range of models, often at affordable prices, can be easily installed under varies conditions, and enable for long-term monitoring with high measurement frequency.

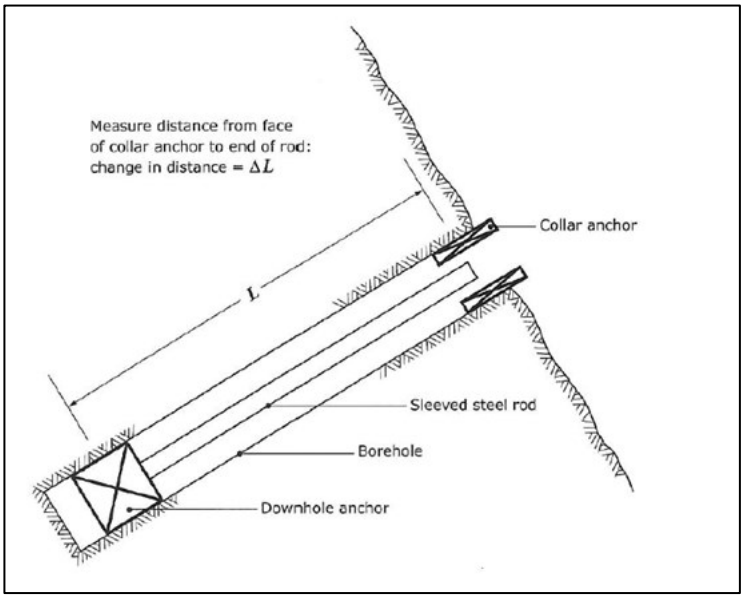

Figure 19. Borehole exstensometer.

Inclinometers, Figure 20, are devices for monitoring deformation normal to the axis of a borehole by means of a probe passing along the pipe encasing. In average, the accuracy is of about ± 8 millimetres every 30 meters of depth.

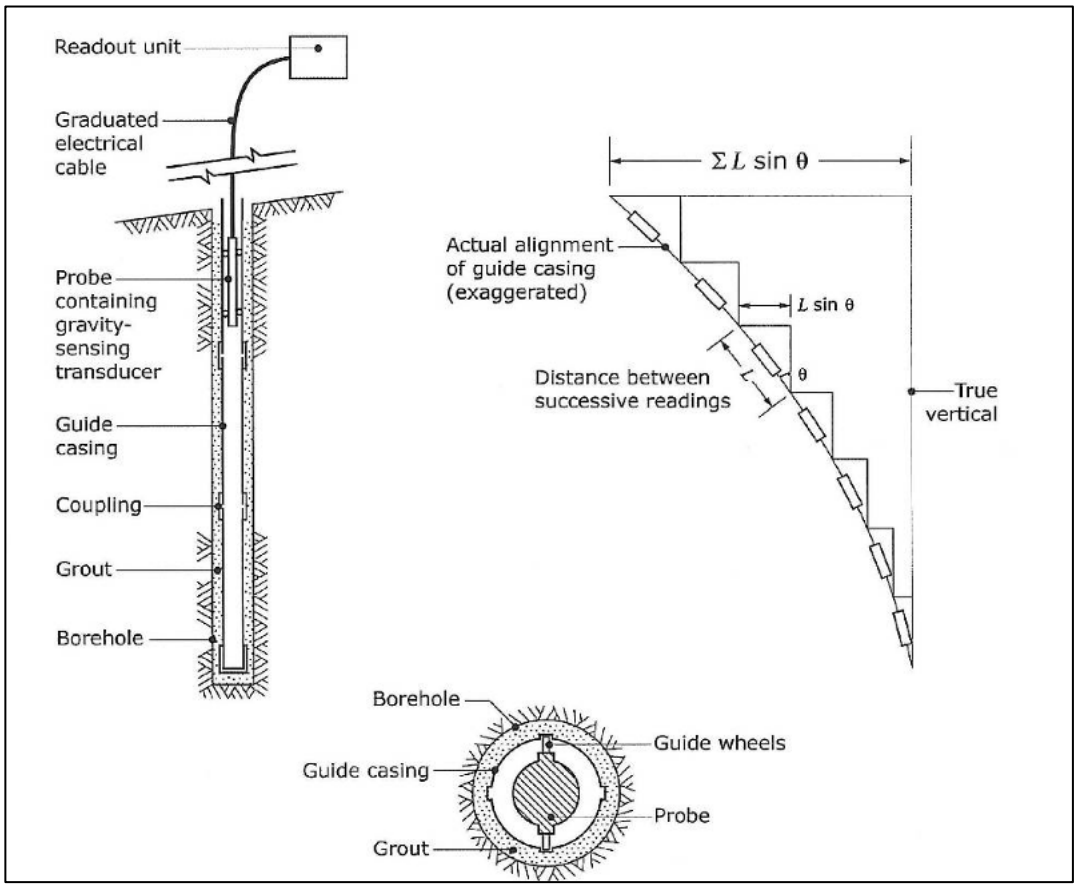

Figure 20. Schematic representation of an inclinometer.

Two Casagrande automatic-reading piezometers, Figure 21, are used to measure groundwater levels and soil water pressure within the soil. Because fluctuations in pore water pressure are crucial to slope instability, these devices are particularly important as early warning system. Rather than monitoring the direct movements of a landslide, they provide essential data on the hydrogeological conditions that could trigger mass movements.

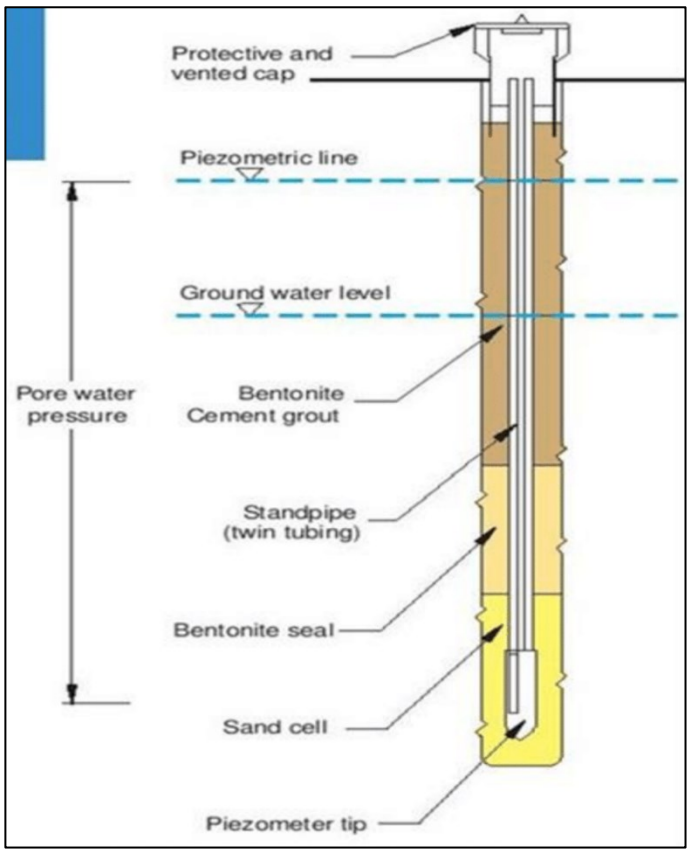

Figure 21. Casagrande piezometer.

The monitoring system is complemented by the installation of a meteorological station near the total station. It is equipped with various instruments to provide continuous data on precipitation, temperature, humidity and other atmospheric parameters. This information is essential for correlating rainfall events with the triggering of landslides and then assessing the hydro-meteorological conditions that trigger or accelerate slope movements.

In addition, SNAM RG commissioned a research group from the University of Padua who drafted an interim report regarding the landslide that affected the area around the gas pipeline. Pre-event deformations were analysed to verify possible precursors with the aid of SAOCOM InSAR data. The project has highlighted the versatility of radar and synthetic aperture remote sensing (SAR), as microwaves are not affected by atmospheric conditions and are able to penetrate clouds, thus allowing continuous monitoring even when the sky is overcast. Moreover, it is possible to perform a back analysis of the movement dynamics with continuous observation starting from a pre-event time to a post-event time without interruptions. The electromagnetic waves emitted by these instruments hit the Earth's surface, are reflected, and then picked up by the receiver. Acquisition from satellites mounted on SAR sensors occurs by observing the Earth's surface at an angle less than 90°, not NADIR, necessary condition to distinguish reflected signals coming from different distances and correctly reconstruct the observed scene. The final image is generated by combining a sequence of partially overlapping acquisitions, thus creating the "synthetic aperture". A schematic representation of the SAR satellite acquisition mode is shown in the Figure 22. Parallel strips parallel to the orbit at different distances can be separated based on the arrival times of the reflected signal, given that the line of sight (LOS) of the sensor is inclined with respect to the vertical. The angle θ is called the off-nadir angle.

Unfortunately, SAR images are subject to geometric deformations, especially in mountainous areas, caused by the observation angle, requiring a correction to be applied.

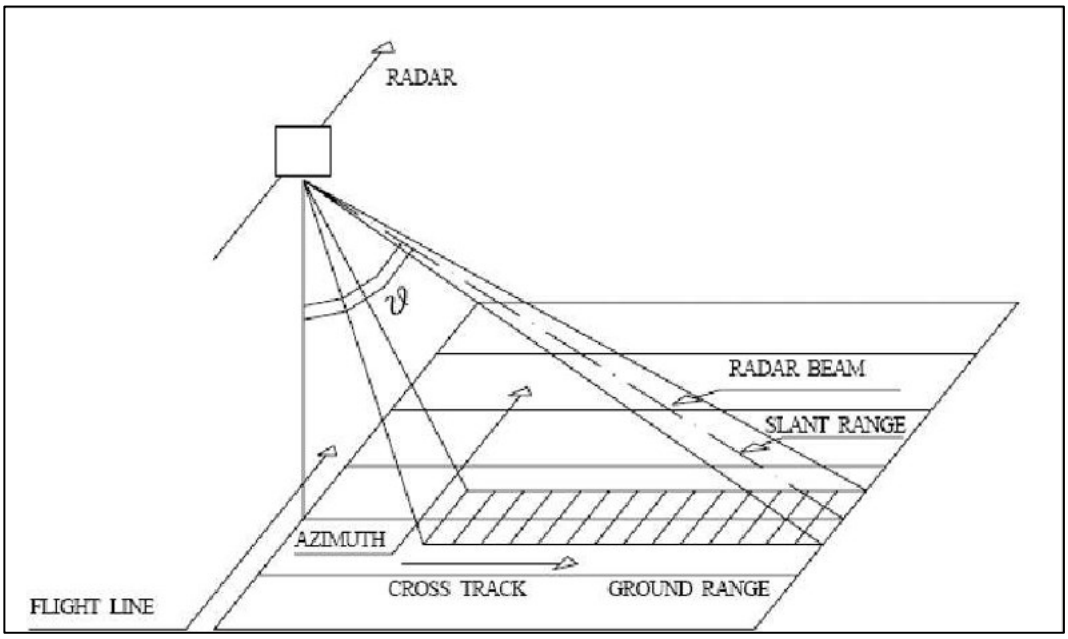

Figure 22. Representation of the acquisition mode of SAR satellites.

By analysing two SAR images acquired from the same viewing geometry at different times, an interferogram can be generated, highlights phase variations associated with potential ground displacement. This methodology, known as SAR interferometry, allows for the identification of deformations even on the order of a few millimetres. The basic principle of the technique is illustrated in the Figure 23.

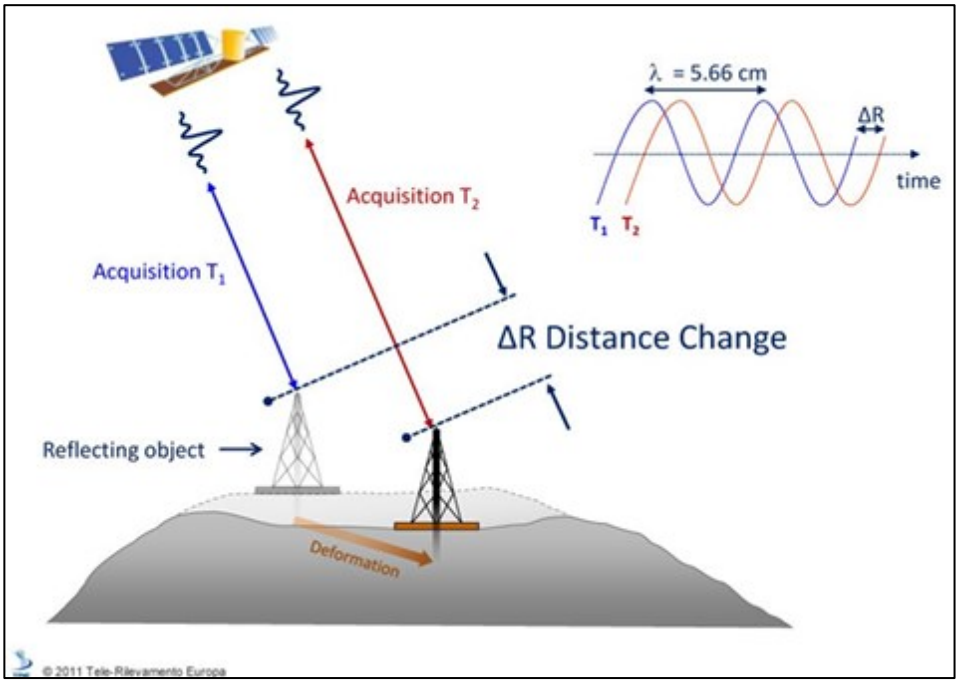

Figure 23. Basic principle of phase difference radar interferometry.

However, the phase difference can be affected by multiple factors including variations in acquisition geometry, atmospheric conditions, noise, and ground motion. To isolate the deformation component, correction and differential analysis techniques are applied, using image pairs or time series of multiple acquisitions.

The report mentioned above proposes InSAR images from the Argentine satellites of the constellation called SAOCOM, from those operated by ESA (Sentinel-1) and from those of the COSMO-Skymed constellation operated by ASI. To make these radar data more complete, multispectral optical images acquired by the PlanetScope satellites were also used, for the rapid mapping and detection of ground effects in the areas of interest and in the surrounding areas. The area defined by the red line in Figure 24 is the area investigated by satellite analyses with MT-InSAR interferometric techniques.

Figure 24. Google Earth aerial view of the focus area for the satellite survey.

The SAOCOM constellation, or Argentine Microwave Observation Satellite, is one of the most important data sources in this system. It was created and managed by the Argentine space agency CONAE (National Space Activities Commission) with the main objective of supporting environmental monitoring and the prevention of natural disasters such as floods, hydrological emergencies and landslides.

SAOCOM satellites are equipped with a SAR radar working in the L-band, with a central frequency of 1275 MHz and a wavelength of approximately 23.6 cm. This configuration allows for accurate images to be obtained without any influence from weather conditions, as microwaves can pass through clouds and partly even vegetation. Furthermore, the greater penetration capacity compared to radars operating in the C-band (such as Sentinel-1) or in the X-band (COSMO-SkyMed) makes SAOCOM data ideal for interferometric analyses (D-InSAR and MT-InSAR) in natural or partially vegetated areas, where other sensors have significant limitations.

A key feature is the SAOCOM ability to provide data on soil moisture, a critical parameter not only for agricultural management and crop forecasting, but also for modelling and predicting shallow landslides. The ability to calculate this parameter is, in fact, a key element in models that predict mass movements, given that soil moisture levels directly impact its stability.

Similar to other SAR satellites designed for interferometric applications, SAOCOM operates in two modes: ascending, Figure 25, and descending, Figure 26, determined by the correlation between Earth's rotation and its orbital trajectory. This dual viewing geometry enables partial reconstruction of the LOS displacement vector along both the vertical axis (nadir) and the horizontal axis (E-W in planer projection).

Satellite	Wavelength	Satellite geometry	Sensor mode	Satellite track
SAO	23.51 cm	ASCENDING	S3	213

Acquisition geometry

Line of sight angle	θ:	33.43°	δ:	12.58°		
Line of sight versors	V:	0.835	N:	-0.12	E:	-0.538

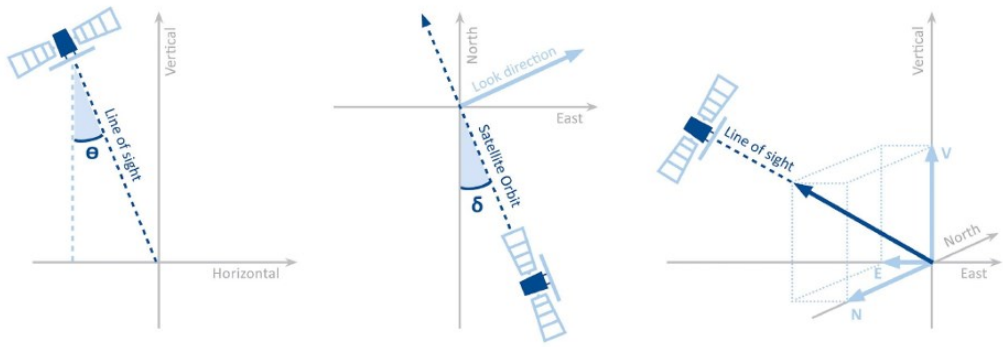

Figure 25. Technical data of SAOCOM acquisitions in ascending orbit.

Satellite	Wavelength	Satellite geometry	Sensor mode	Satellite track
SAO	23.51 cm	DESCENDING	S4	110

Acquisition geometry

Line of sight angle	ɵ:	36.5°	δ:	8.34°		
Line of sight versors	V:	0.804	N:	-0.086	E:	0.589

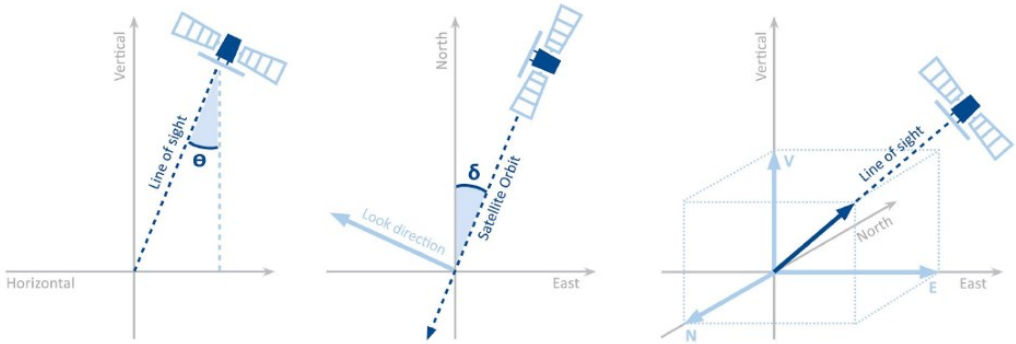

Figure 26. Technical data of SAOCOM acquisitions in descending orbit.

The Sentinel-1 satellites, part of the European Space Agency's (ESA) Copernicus programme, are designed for continuous Earth observation using C-band SAR radar (5.405 GHz, 5.5 cm wavelength). This mission includes Sentinel-1A, launched in 2014, and Sentinel-1B in 2016, later replaced by Sentinel-1C. Together, they provide a nominal six-day revisit, although effective global coverage is approximately 11–12 days. Compared to SAOCOM, Sentinel-1 offers a more consistent and reliable acquisition rate, is specifically designed for interferometric applications, incorporates automated pre-processing workflows, and has provided free, standardized data since 2016, facilitating the creation of longer and more uniform time series for deformation analysis and environmental monitoring.

Other satellites used for data collection were:

- The COSMO-SkyMed constellation (constellation of small Satellites for the Mediterranean basin Observation) is an Earth observation system developed by the Italian Space Agency (ASI) and the Ministry of Defence, designed for both civil and military applications. It consists of four first-generation satellites, now joined by a second-generation satellite (CSG) that enhances their operational performance.

In this case, the satellites are equipped with synthetic aperture radar (SAR) operating in the X-band, capable of obtaining high-resolution images in all weather and lighting conditions. The short wavelength of the X-band allows for the capture of very fine details of the Earth's surface but reduces interferometric coherence in areas covered by vegetation or in natural environments, limiting the effectiveness of D-InSAR and MT-InSAR methodologies in such situations. For this reason, data from COSMO-SkyMed are best used in urban settings, where the presence of stable surfaces allows for accurate observation of small deformations in the ground and buildings. Another strength of the constellation is its rapid observation intervals.

- The PlanetScope constellation, created by Planet Labs, consists of numerous microsatellites known as Doves, designed to observe the Earth's surface through multispectral optical imagery. Thanks to their orbital position, these satellites offer near-daily coverage of the entire planet, providing images with high spatial resolution (3-5 meters per pixel). The sensors installed on the satellites collect information in four spectral bands (blue, green, red, and near-infrared - NIR), enabling multispectral analysis useful for activities such as land use classification, vegetation monitoring, environmental change mapping, and object and infrastructure detection. By virtue of its high detection frequency and excellent radiometric resolution, the PlanetScope constellation is proposed as a useful tool for the rapid mapping and analysis of ground impacts in situations of hydrogeological instability or large-scale environmental changes.

A comparison was also conducted with the ALOS-2 (Advanced Land Observing Satellite-2) dataset, a satellite belonging to the Japanese space agency JAXA that operates a PALSAR-2 sensor in the L-band with a frequency of 1.2 GHz. To compare the data with those obtained by SAOCOM, the data were subjected to SqueeSAR interferometric processing. ALOS-2, having a greater off-nadir angle than SAOCOM, is not ideally suited to observing purely mountainous areas with steep slopes, but around it shows an acceptable density of reflectors for the analysis of slow phenomena.

3. Results

3.1Results of monitoring systems

3.1.1 Extensometers and piezometers results

The results derived from the extensometers and piezometers are presented below. Figure 27 illustrates the spatial distribution of the six extensometers (C_0102, C_0103, R_0003, R_0004, R_0005, R_0006), the two piezometers (R_0006, C_0103), and the reference weather station W, equipped with an anemometer, a rain gauge, a thermometer, and a hygrometer. The time interval considered extends from the beginning of measurements on 29 February 2024, until 31 December 2024, as the devices were not active before that day. Figures 28-39 present the recorded data that will be examined in detail and interpreted in the following section.

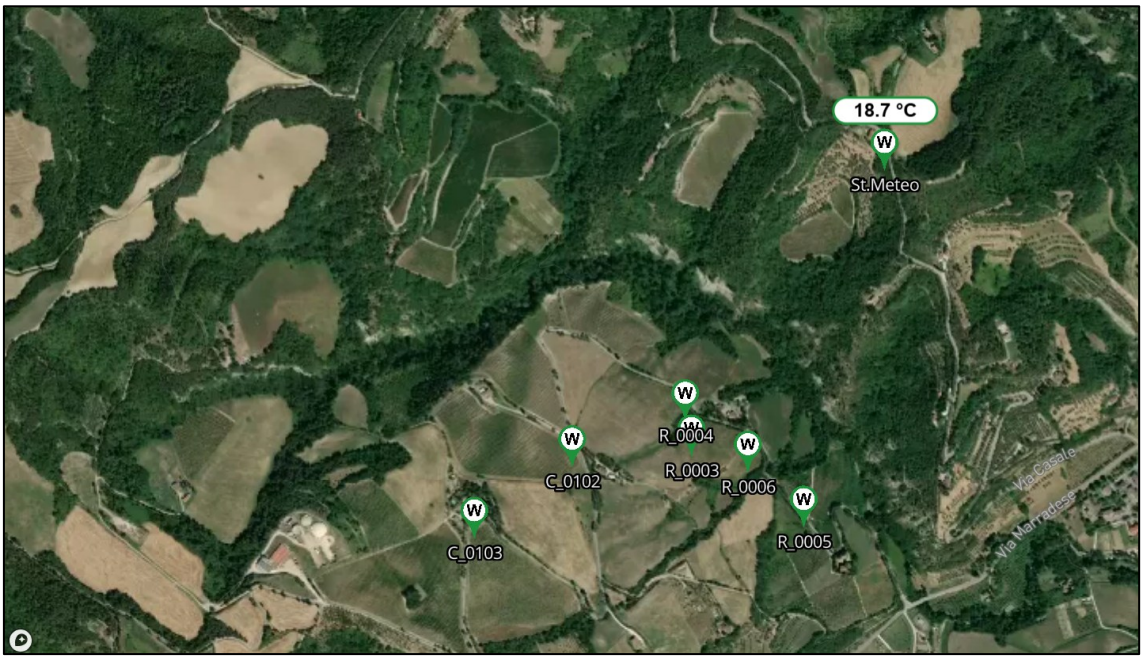

Figure 27. Location of extensometers, piezometers and weather station.

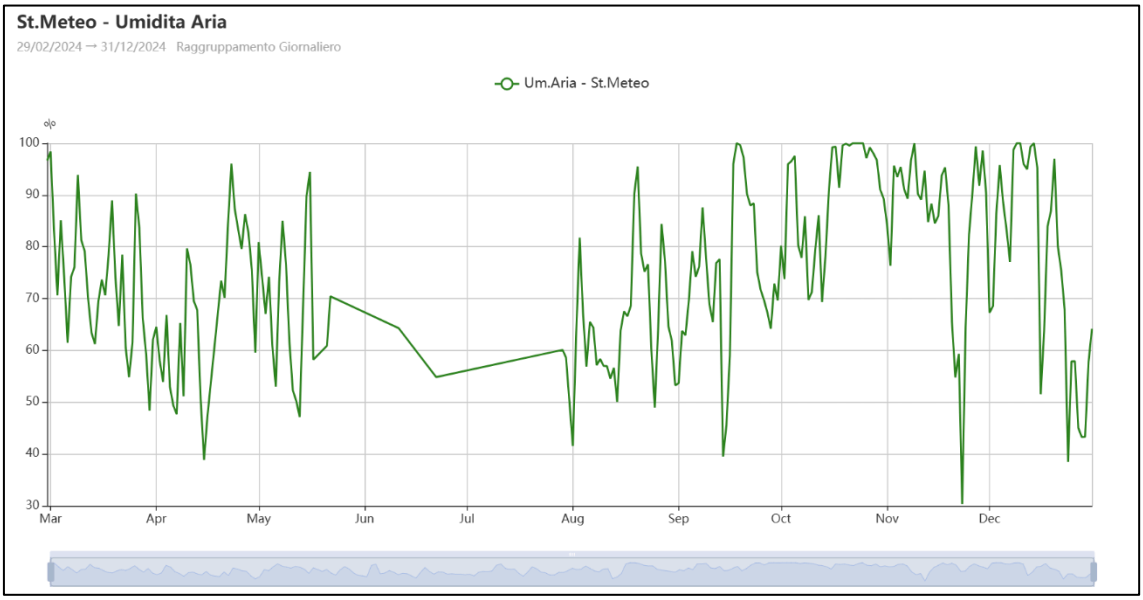

Figure 28. Results recorded by the weather station for mean air humidity from 29 February 2024 to 31 December 2024.

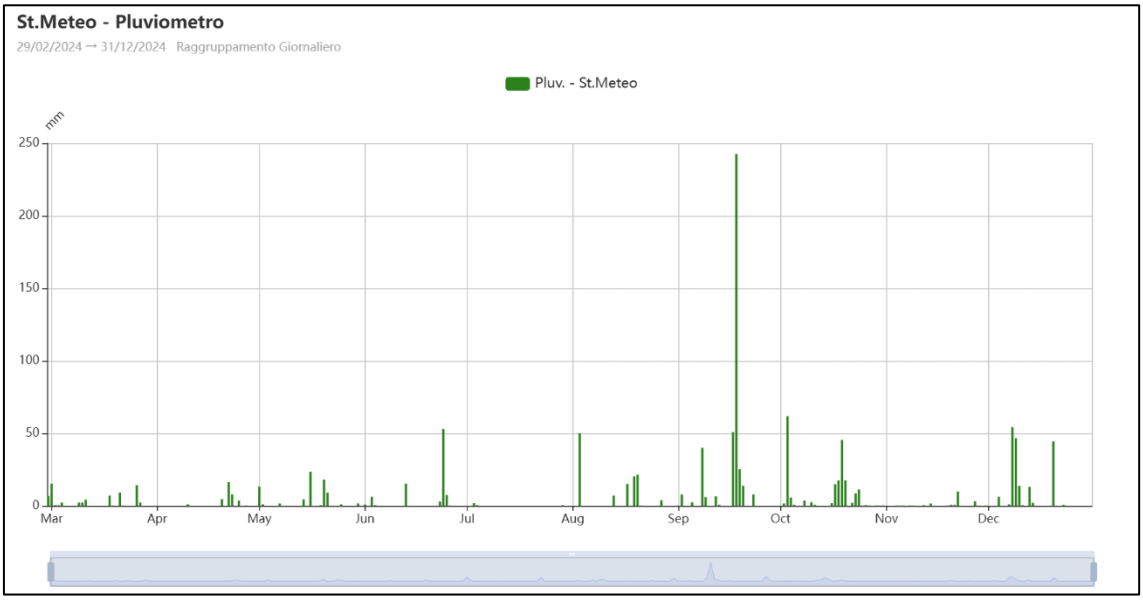

Figure 29. Results recorded by the weather station for precipitation from 29 February 2024 to 31 December 2024.

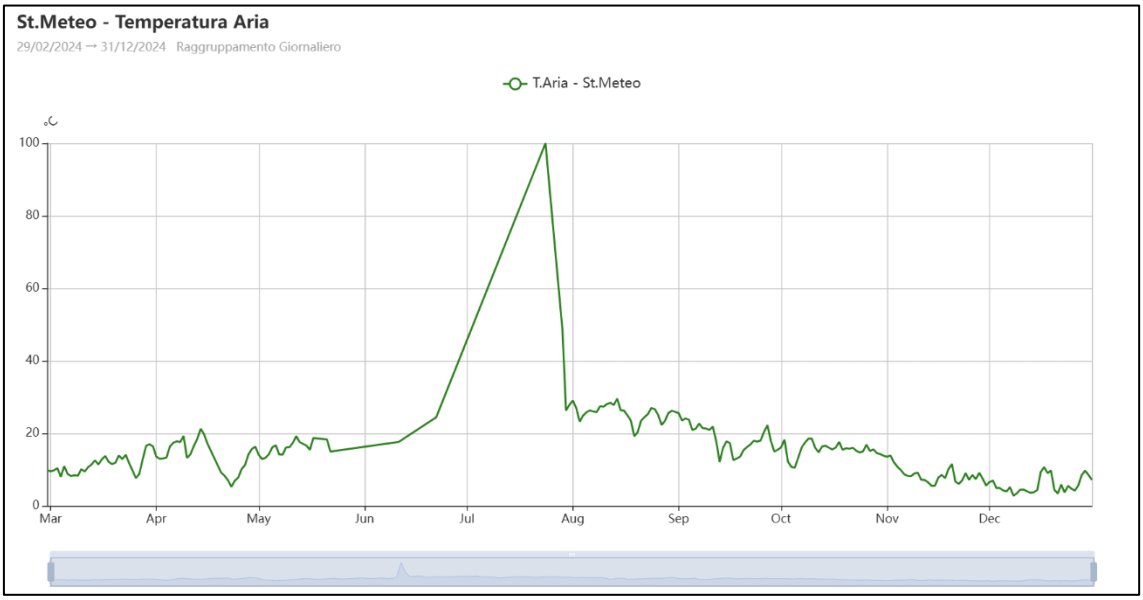

Figure 30. Results recorded by the weather station for air temperature from 29 February 2024 to 31 December 2024.

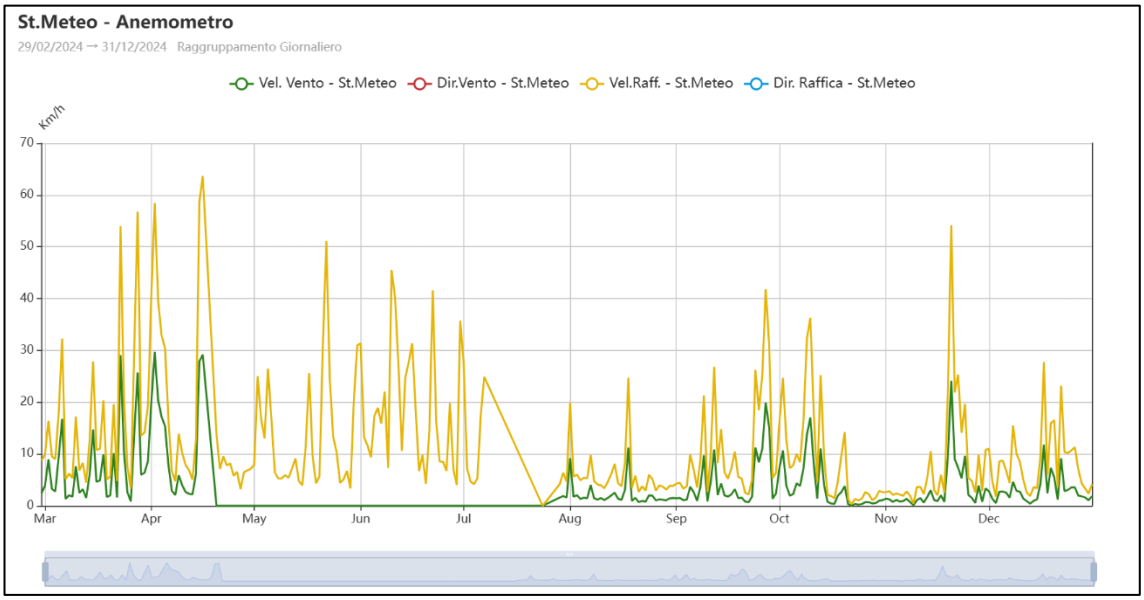

Figure 31. Results recorded by the weather station for wind velocity from 29 February 2024 to 31 December 2024.

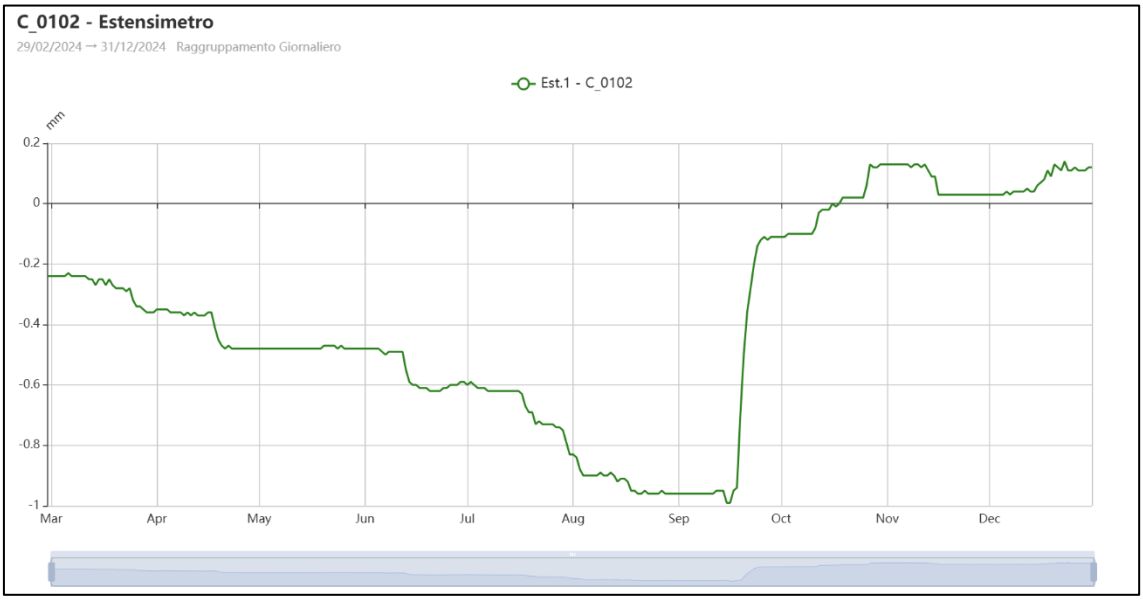

Figure 32. Exstensimeter C_0102 trend from 29 February 2024 to 31 December 2024.

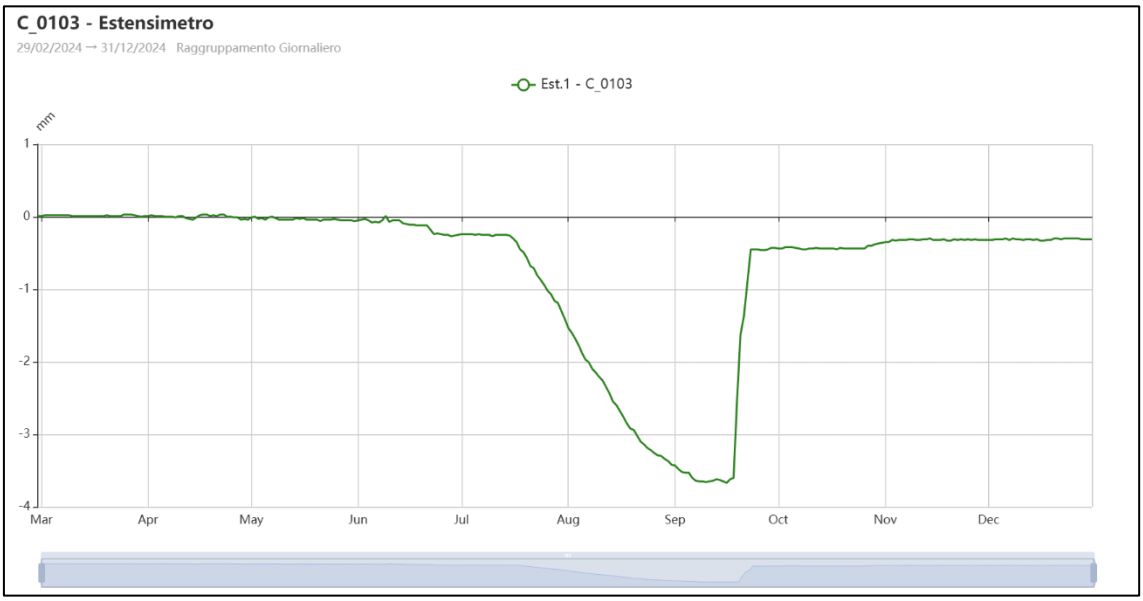

Figure 33. Exstensimeter C_0103 trend from 29 February 2024 to 31 December 2024.

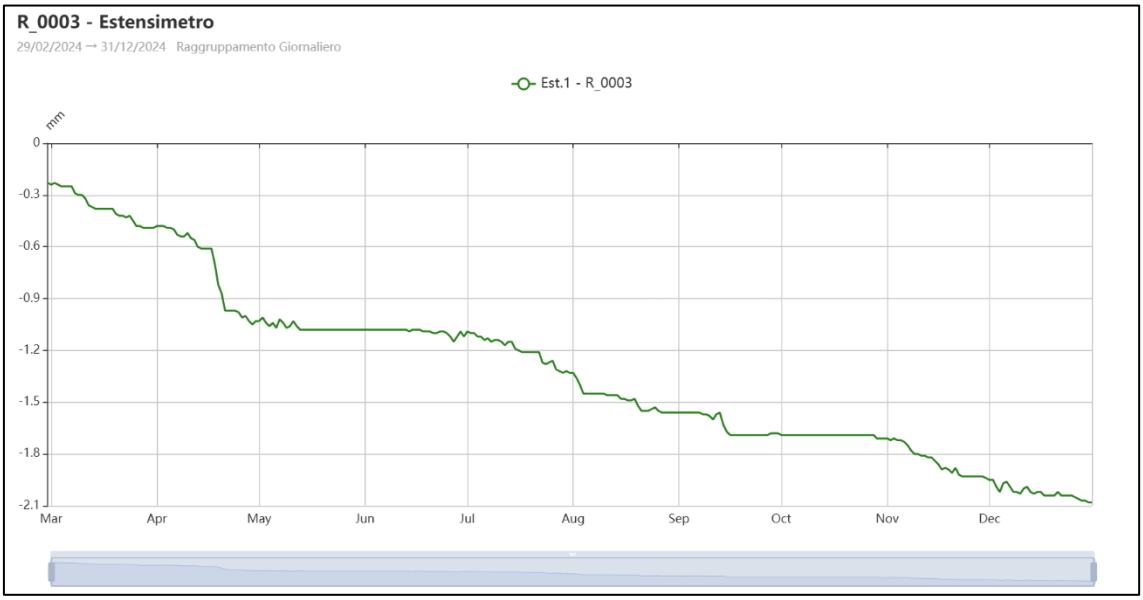

Figure 34. Exstensimeter R_0003 trend from 29 February 2024 to 31 December 2024.

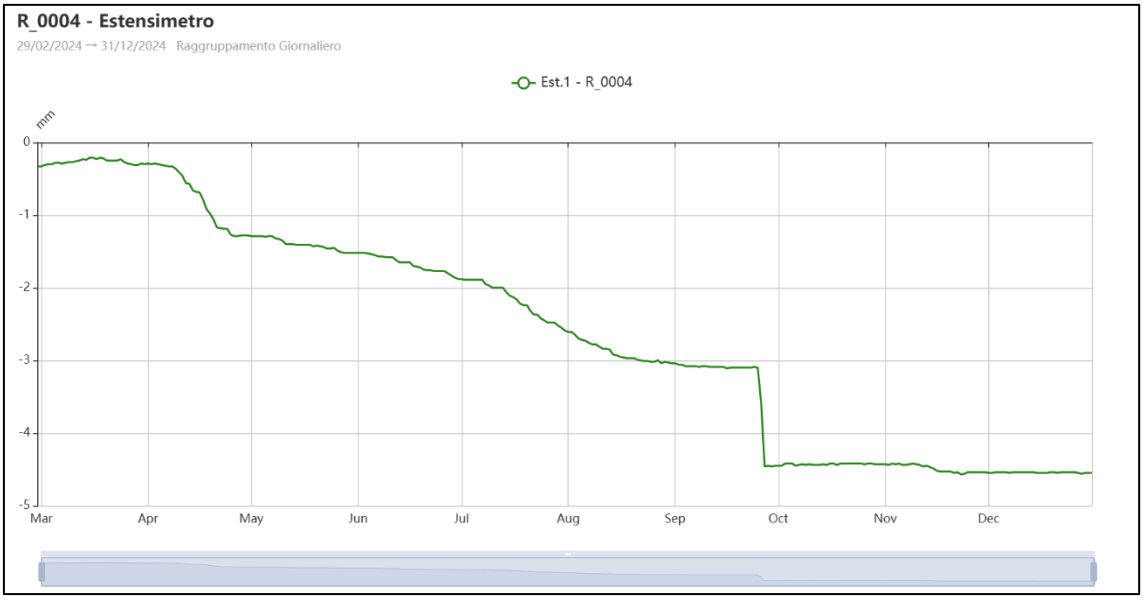

Figure 35. Exstensimeter R_0004 trend from 29 February 2024 to 31 December 2024.

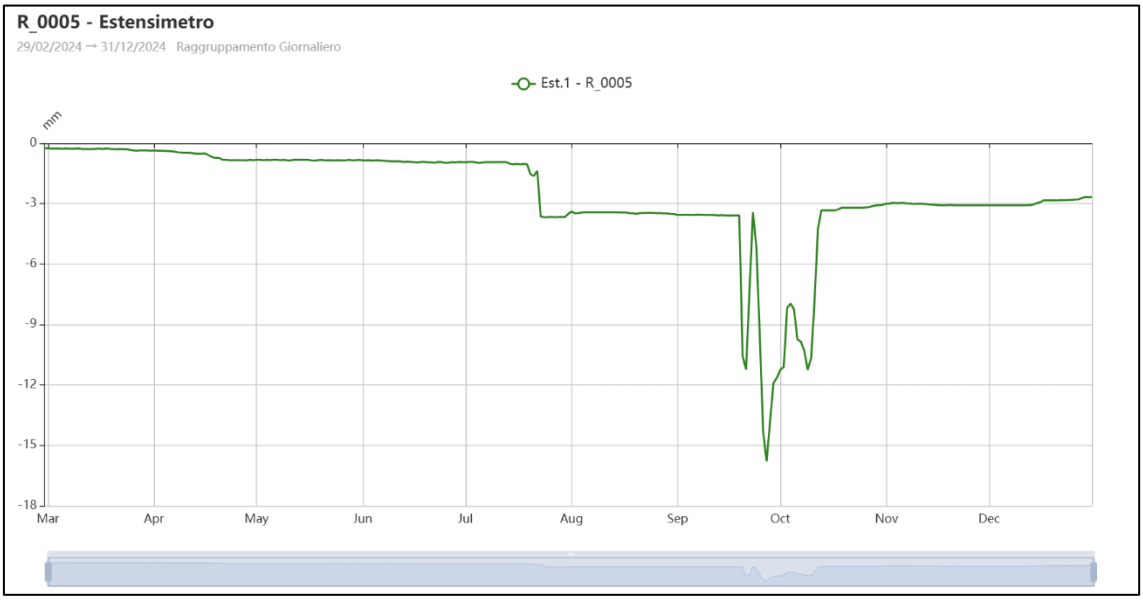

Figure 36. Exstensimeter R_0005 trend from 29 February 2024 to 31 December 2024.

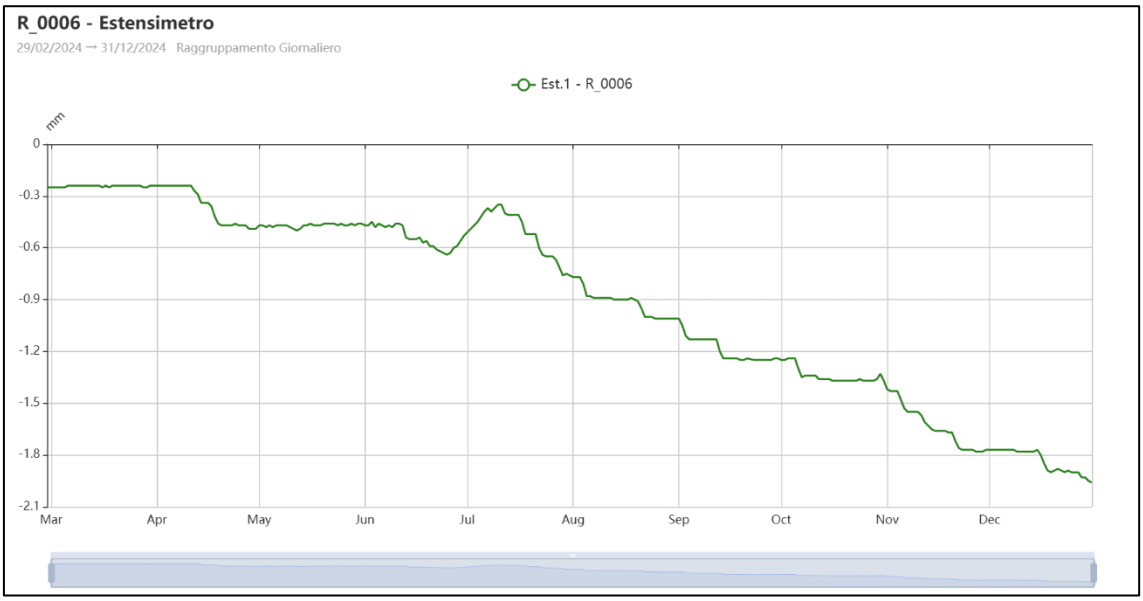

Figure 37. Exstensimeter R_0006 trend from 29 February 2024 to 31 December 2024.

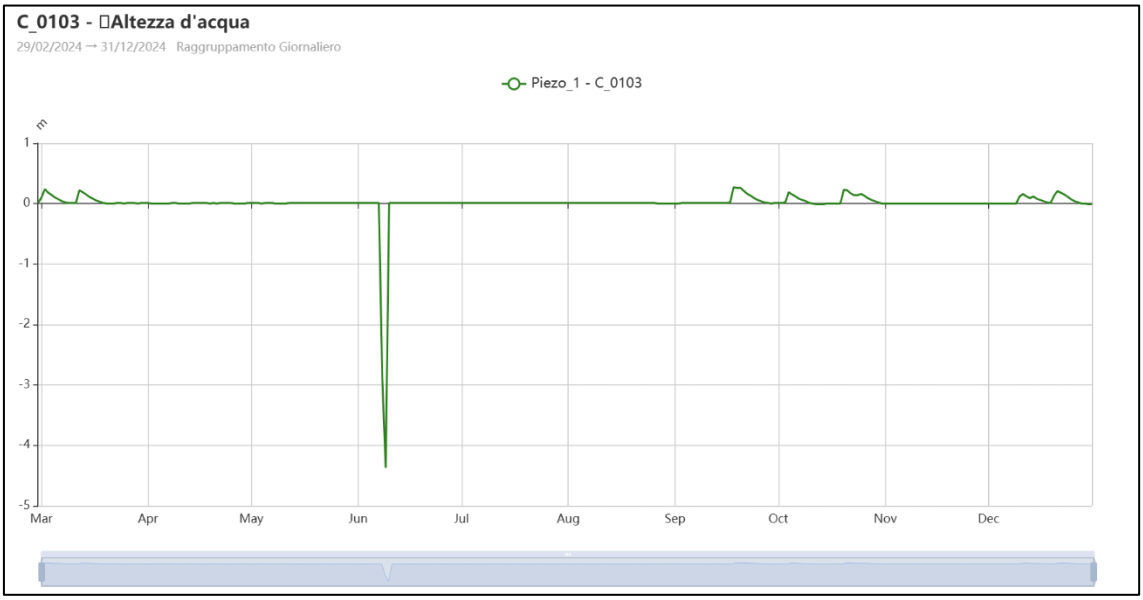

Figure 38. Water height C_0103 trend from 29 February 2024 to 31 December 2024.

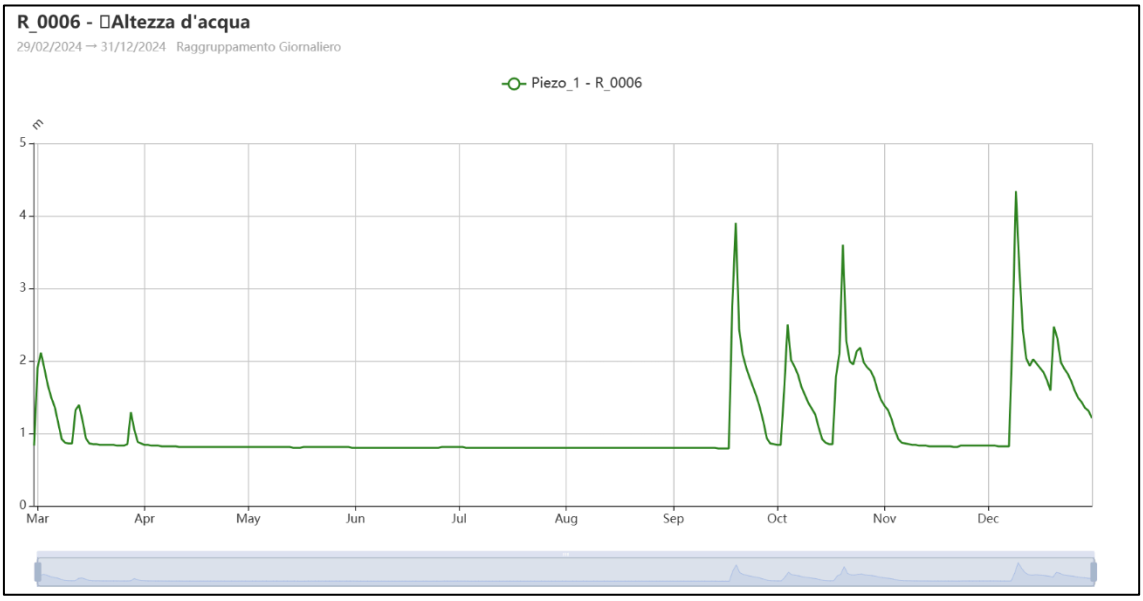

Figure 39. Water height R_0006 trend from 29 February 2024 to 31 December 2024.

3.1.2 Total station and reflectors result

Each graph below illustrates the progress of the 35 monitored devices (note: not all are operational) along with four reference points related to the height of the reflectors above sea level, the displacement towards the East (Easting), and the displacement towards the North (Northing). The available dataset begins on April 1, 2024. The total station stopped functioning in February 2025 and has not yet been restored by its operators; therefore, no additional data can be accessed beyond that date. Figures 41-58 present the recorded data that will be examined in detail and interpreted in the following section.

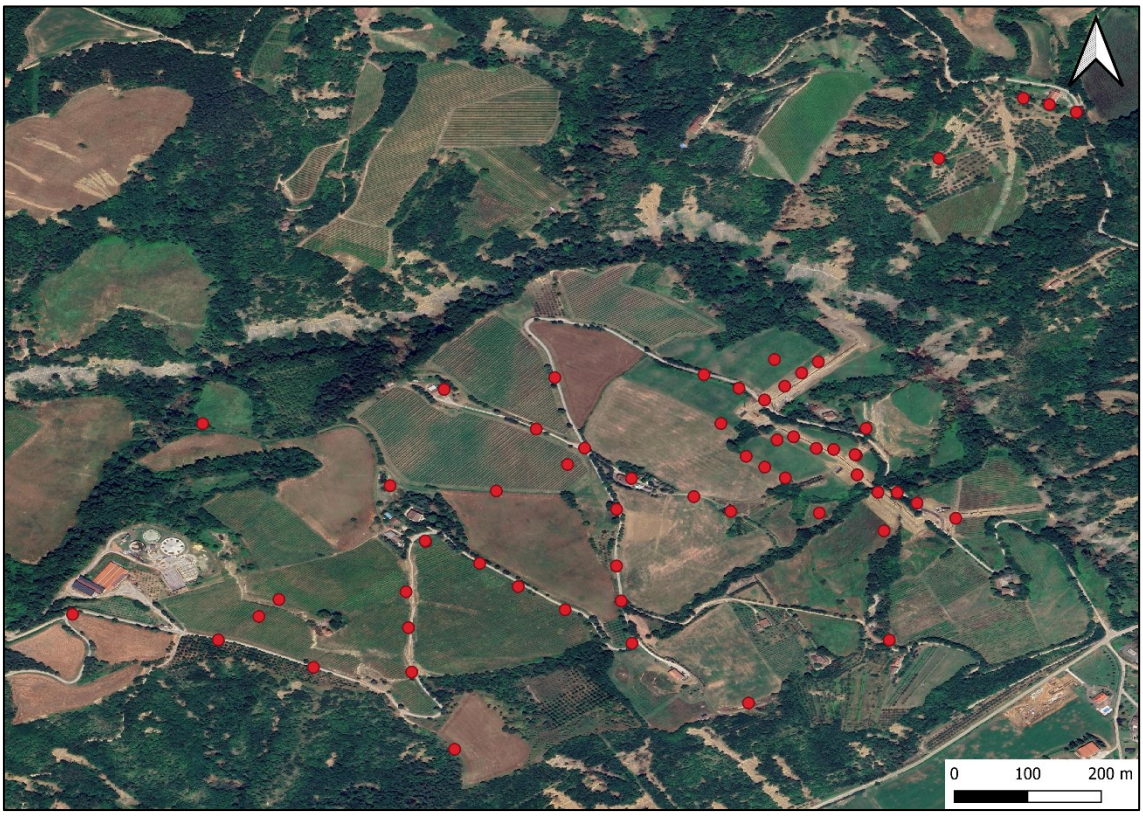

Figure 40. Reflectors position along the slope.

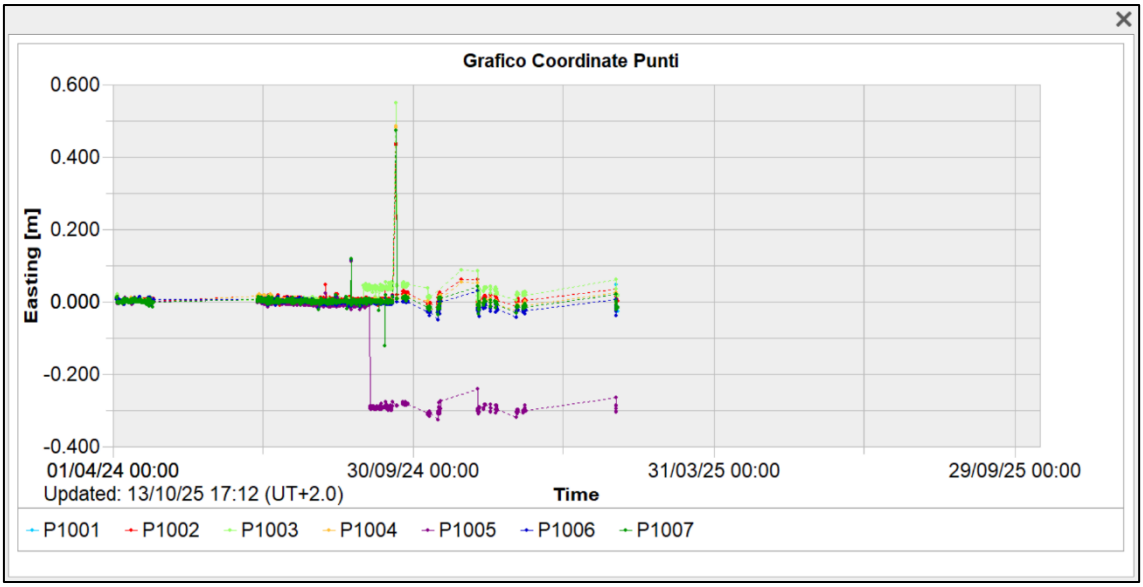

Figure 41. Point coordinate graph, Easting of P1001, P1002, P1003, P1004, P1005, P1006 and P1007.

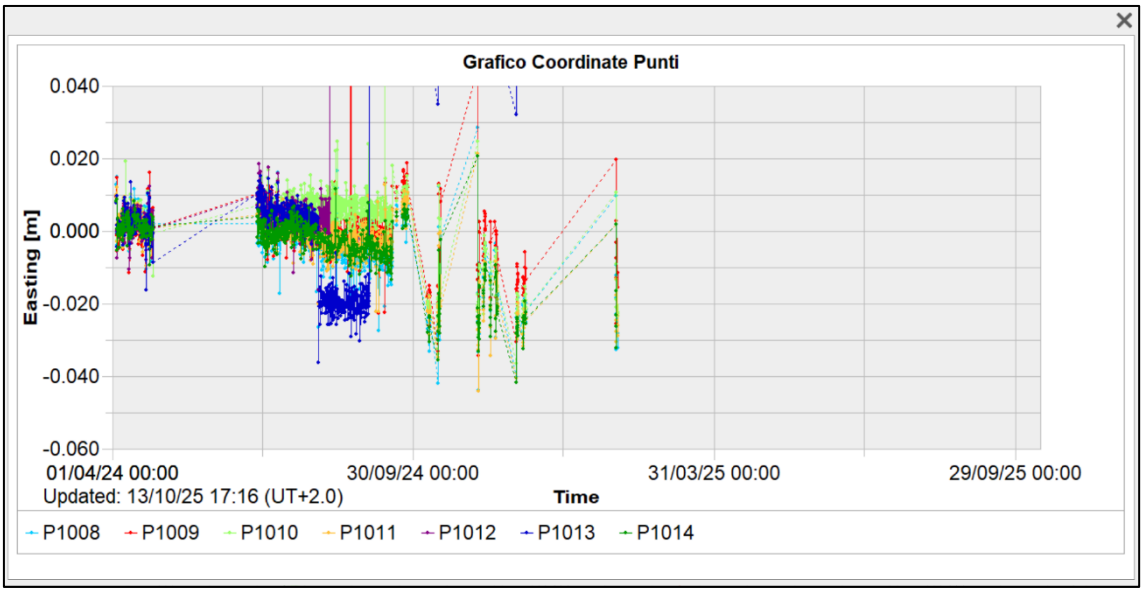

Figure 42. Point coordinate graph, Easting of P1008, P1009, P1010, P1011, P1012, P1013 and P1014.

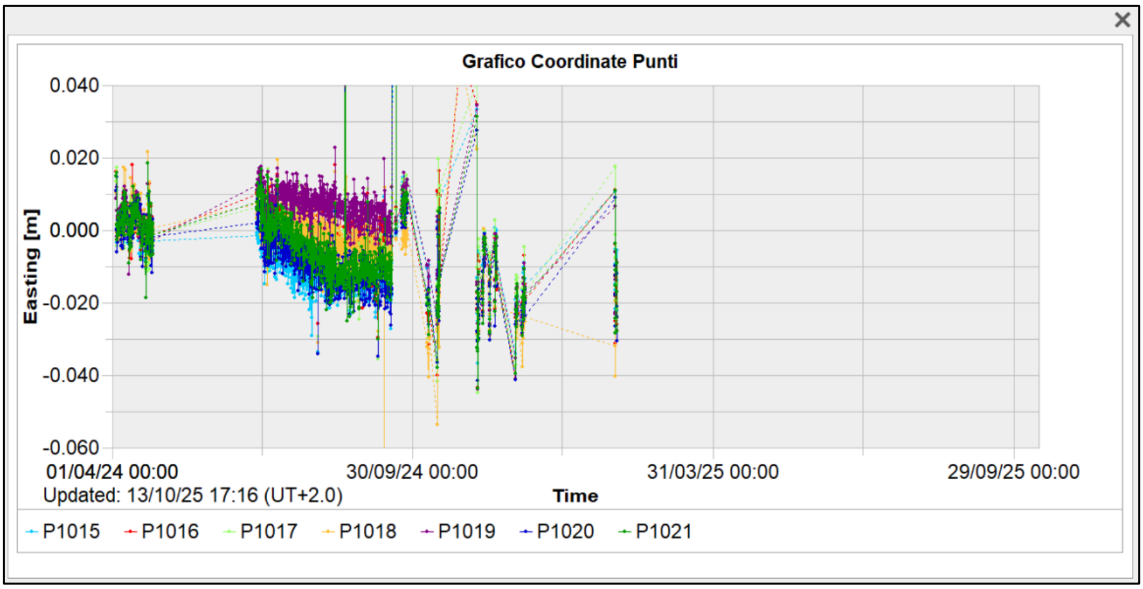

Figure 43. Point coordinate graph, Easting of P1015, P1016, P1017, P1018, P1019, P1020 and P1021.

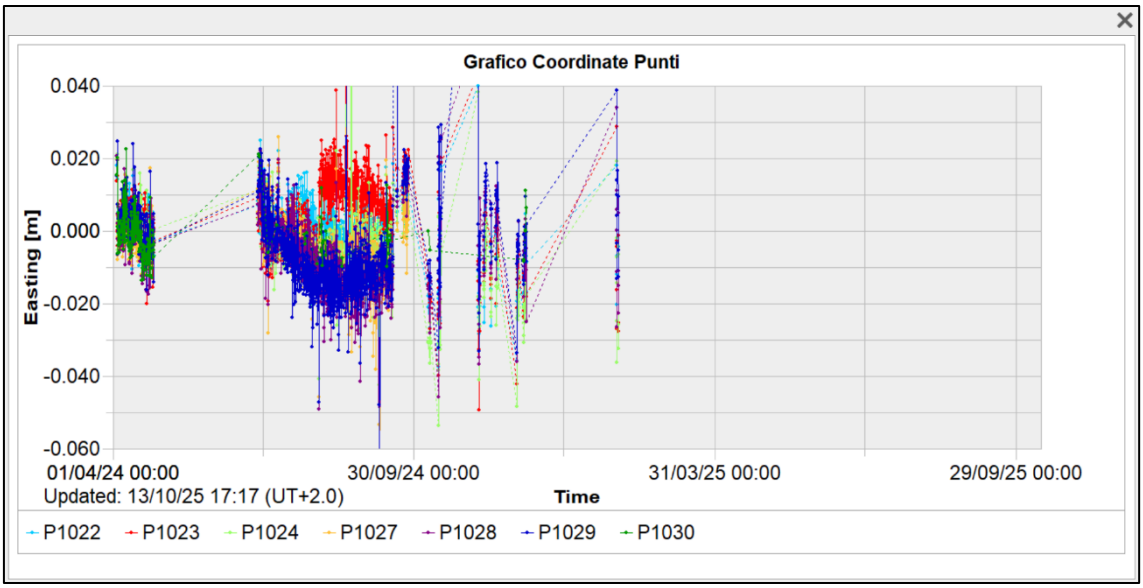

Figure 44.Point coordinate graph, Easting of P1022, P1023, P1024, P1027, P1028, P1029 and P1030.

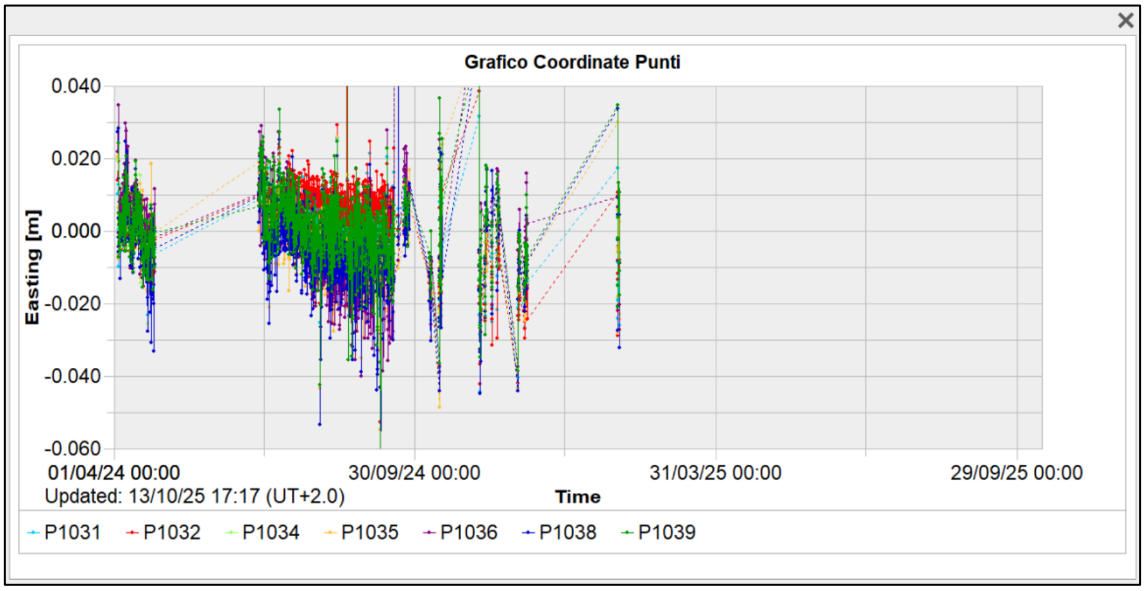

Figure 45. Point coordinate graph, Easting of P1031, P1032, P1034, P1035, P1036, P1038 and P1039.

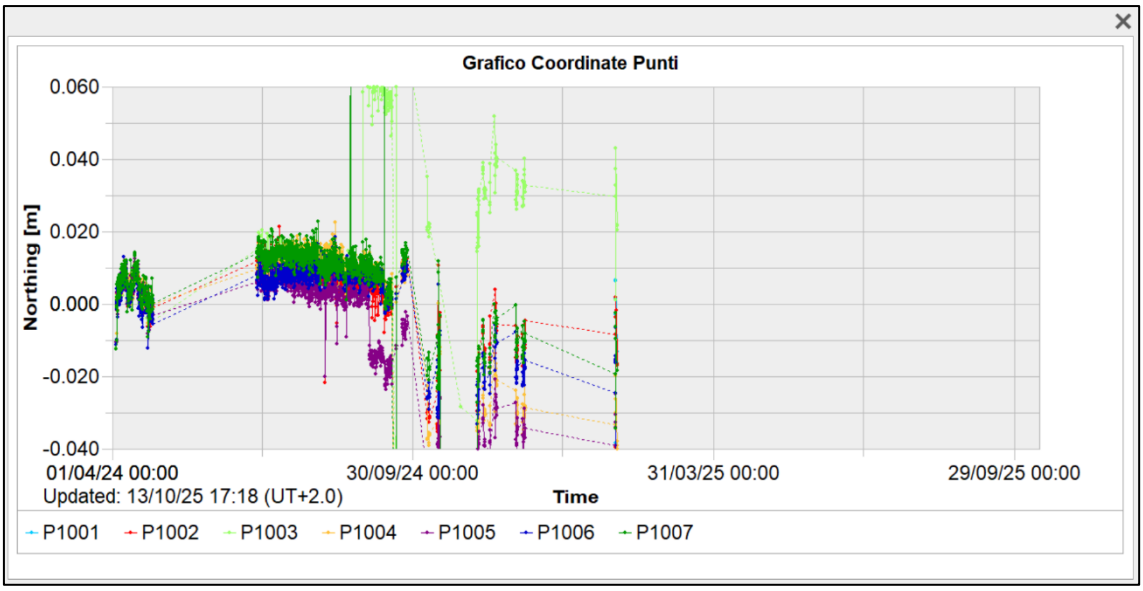

Figure 46. Point coordinate graph, Northing of P1001, P1002, P1003, P1004, P1005, P1006 and P1007.

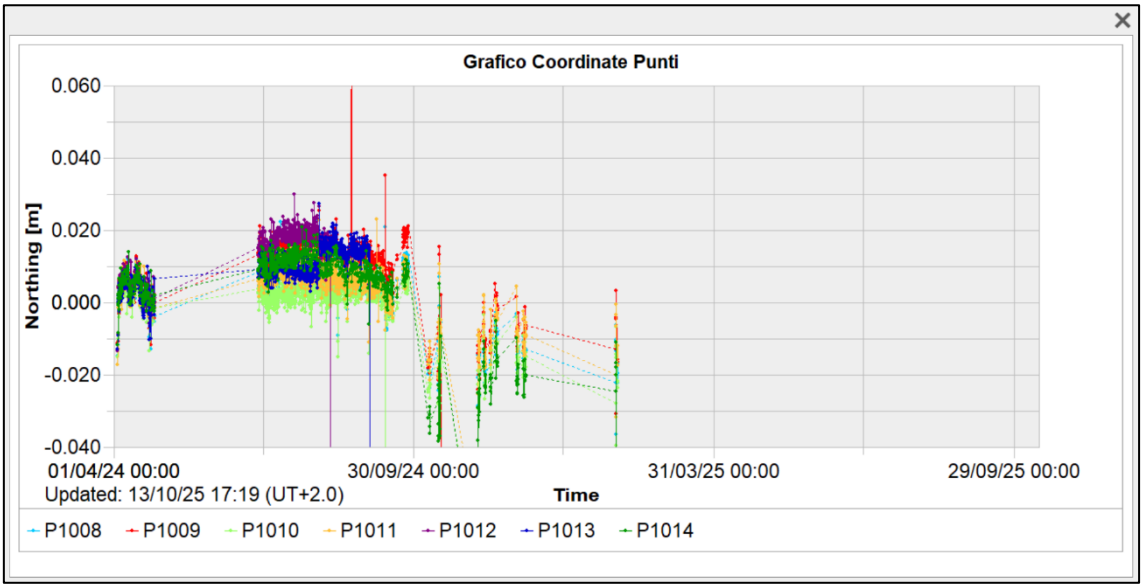

Figure 47. Point coordinate graph, Northing of P1008, P1009, P1010, P1011, P1012, P1013 and P1014.

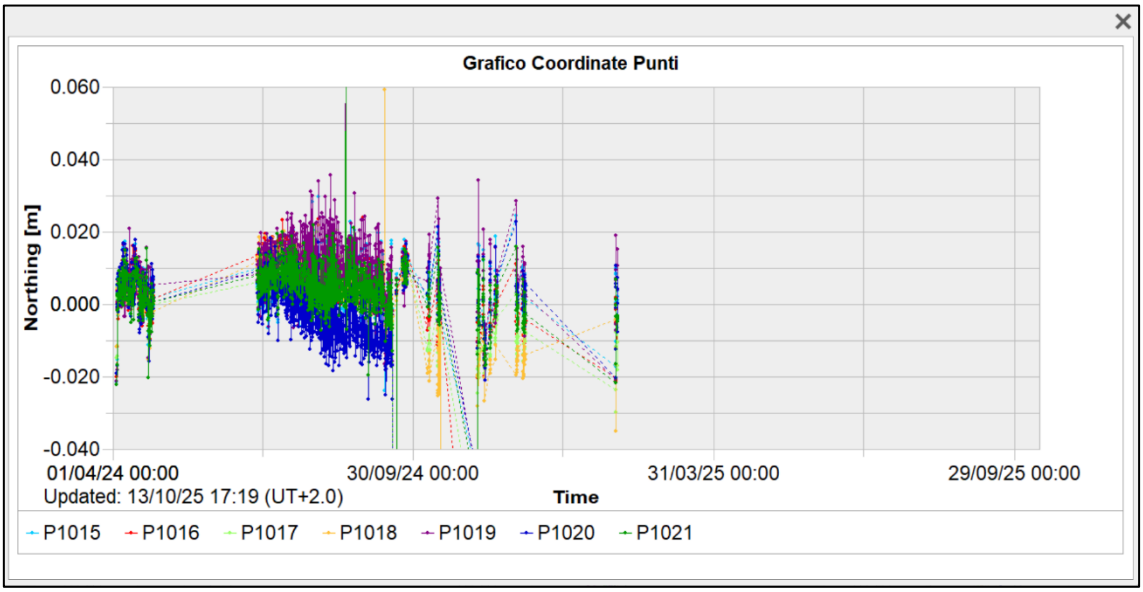

Figure 48. Point coordinate graph, Northing of P1015, P1016, P1017, P1018, P1019, P1020 and P1021.

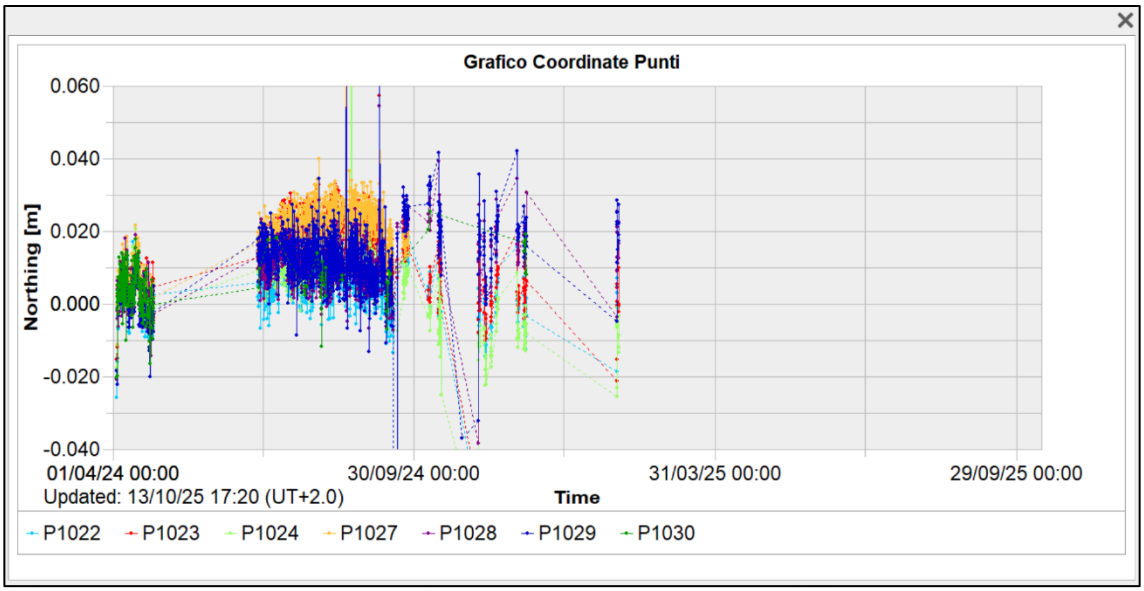

Figure 49. Point coordinate graph, Northing of P1022, P1023, P1024, P1027, P1028, P1029 and P1030.

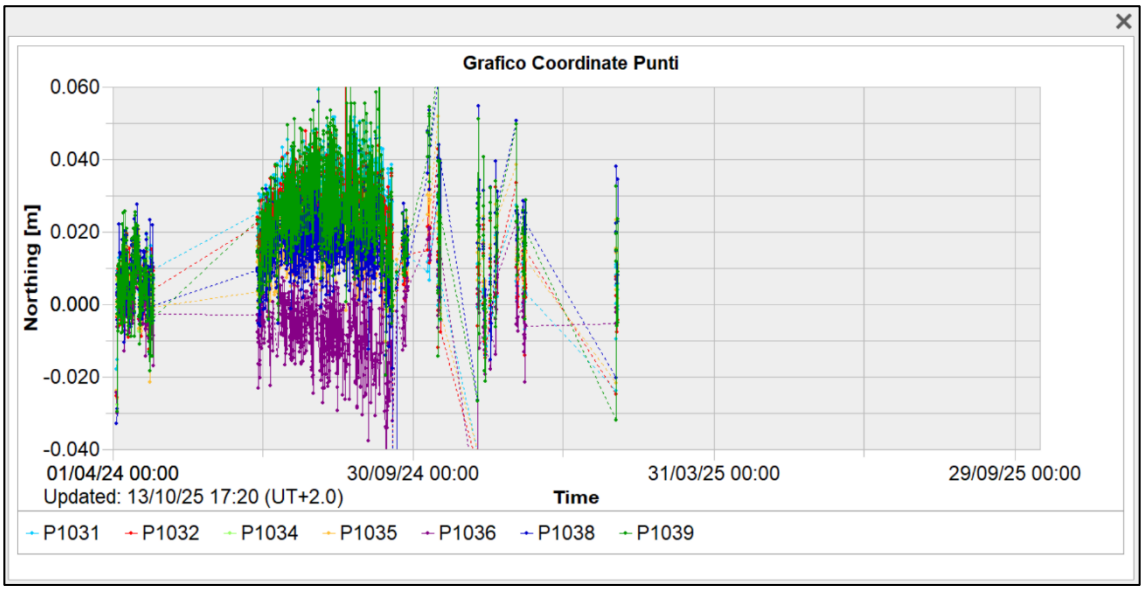

Figure 50. Point coordinate graph, Northing of P1031, P1032, P1034, P1035, P1036, P1038 and P1039.

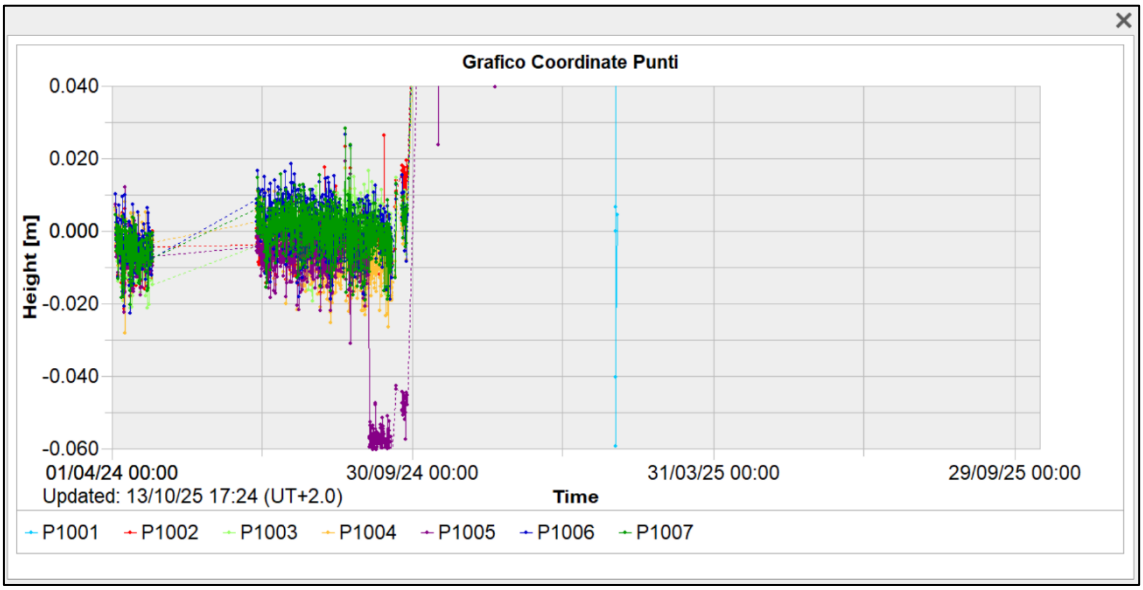

Figure 51. Point coordinate graph, Heigth of P1001, P1002, P1003, P1004, P1005, P1006 and P1007.

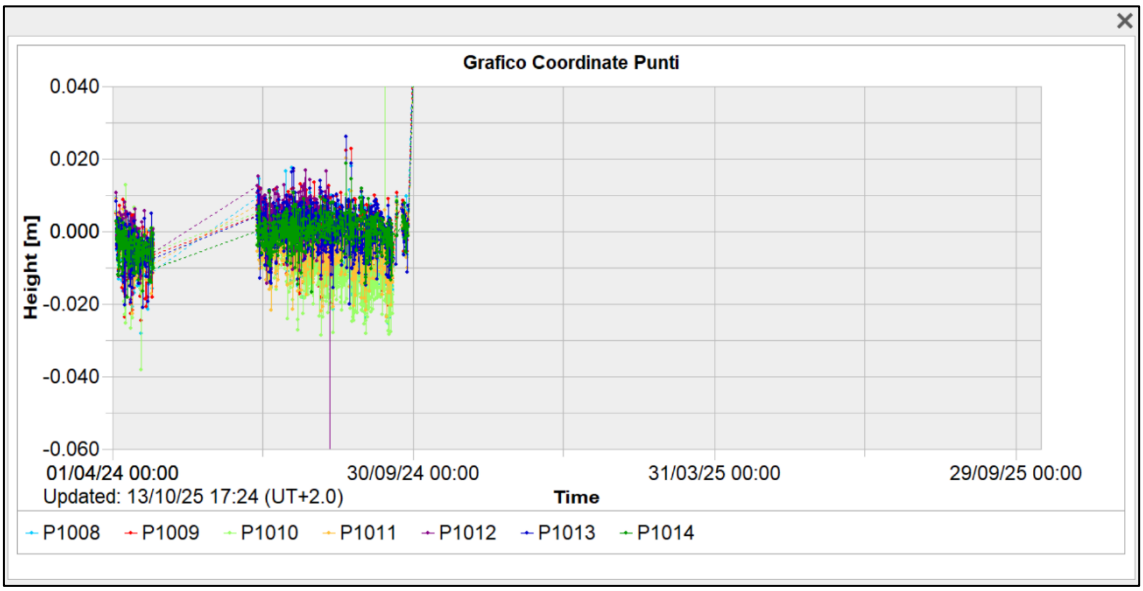

Figure 52. Point coordinate graph, Heigth of P1008, P1009, P1010, P1011, P1012, P1013 and P1014.

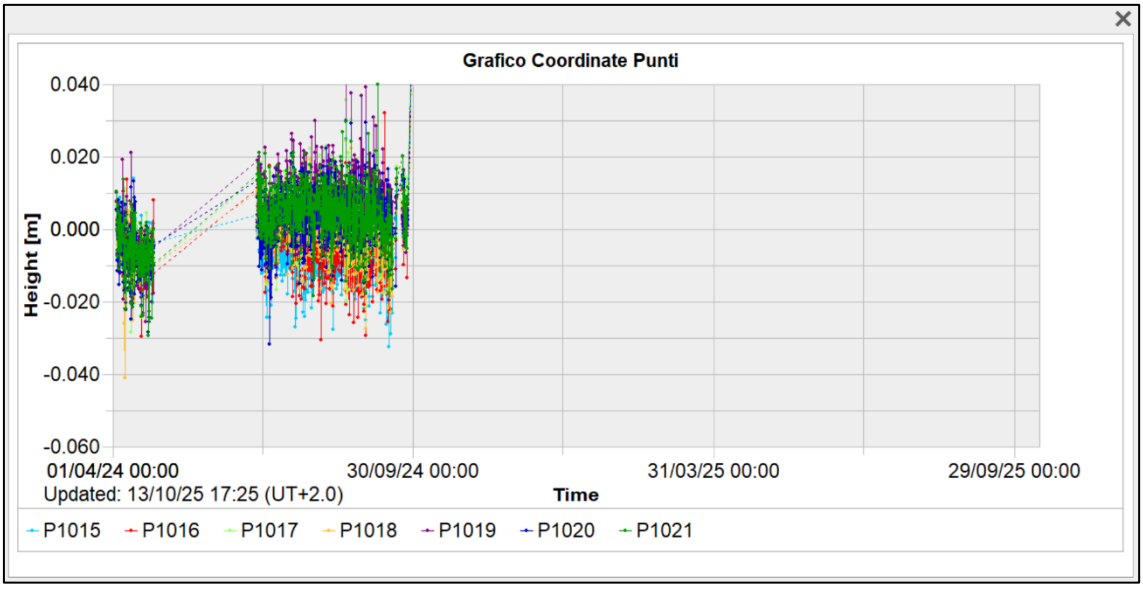

Figure 53. Point coordinate graph, Heigth of P1015, P1016, P1017, P1018, P1019, P1020 and P1021.

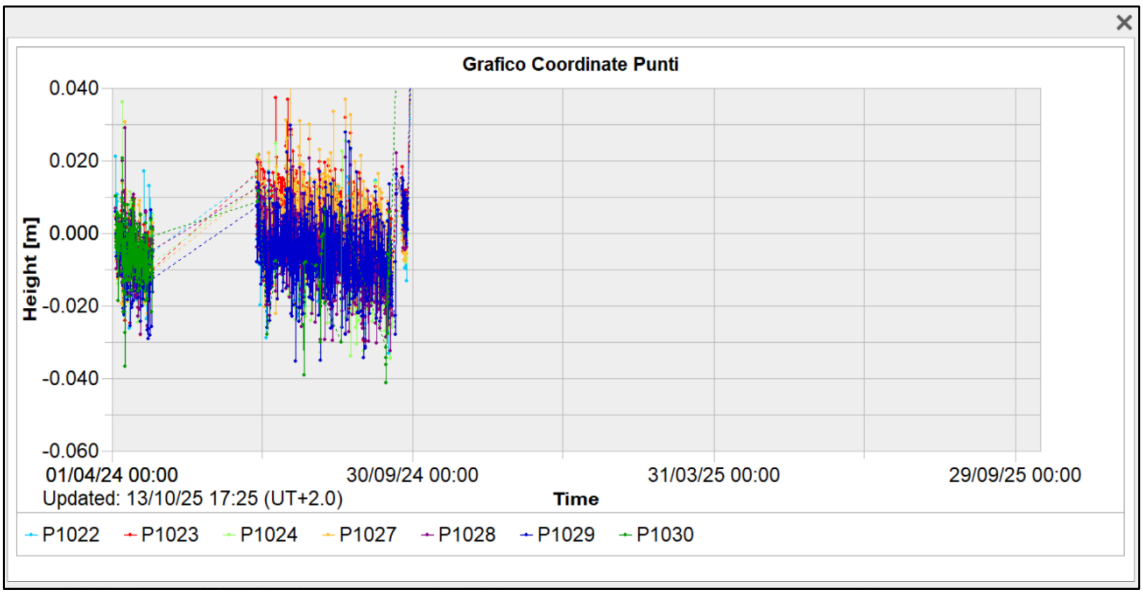

Figure 54. Point coordinate graph, Heigth of P1022, P1023, P1024, P1027, P1028, P1029 and P1030.

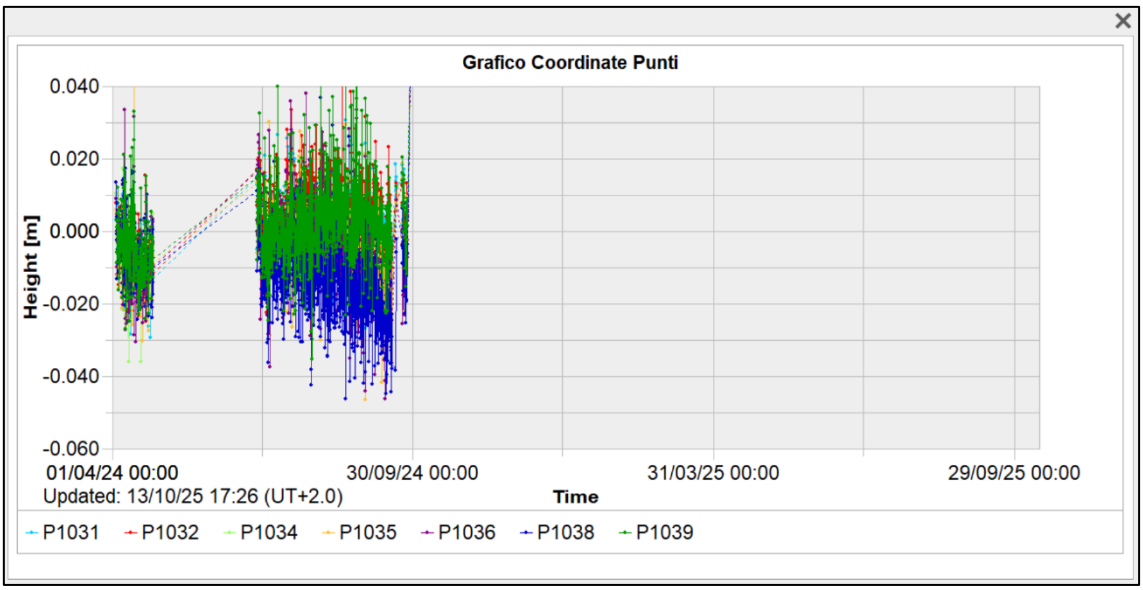

Figure 55. Point coordinate graph, Heigth of P1031, P1032, P1034, P1035, P1036, P1038 and P1039.

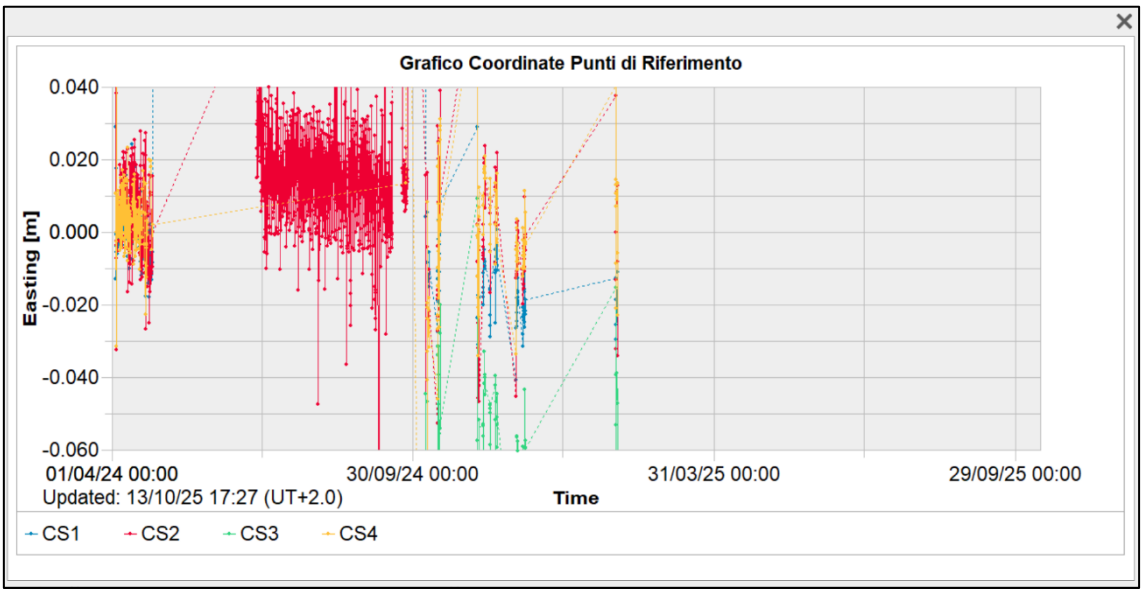

Figure 56. Coordinate graph of reference points, Easting of CS1, CS2, CS3 and CS4.

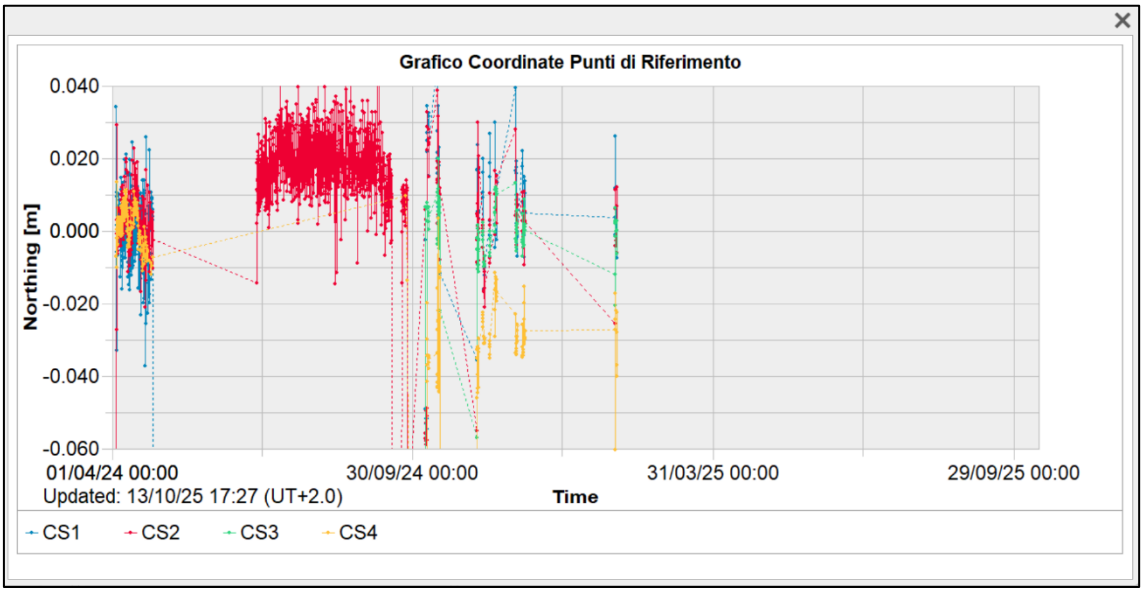

Figure 57. Coordinate graph of reference points, Northing of CS1, CS2, CS3 and CS4.

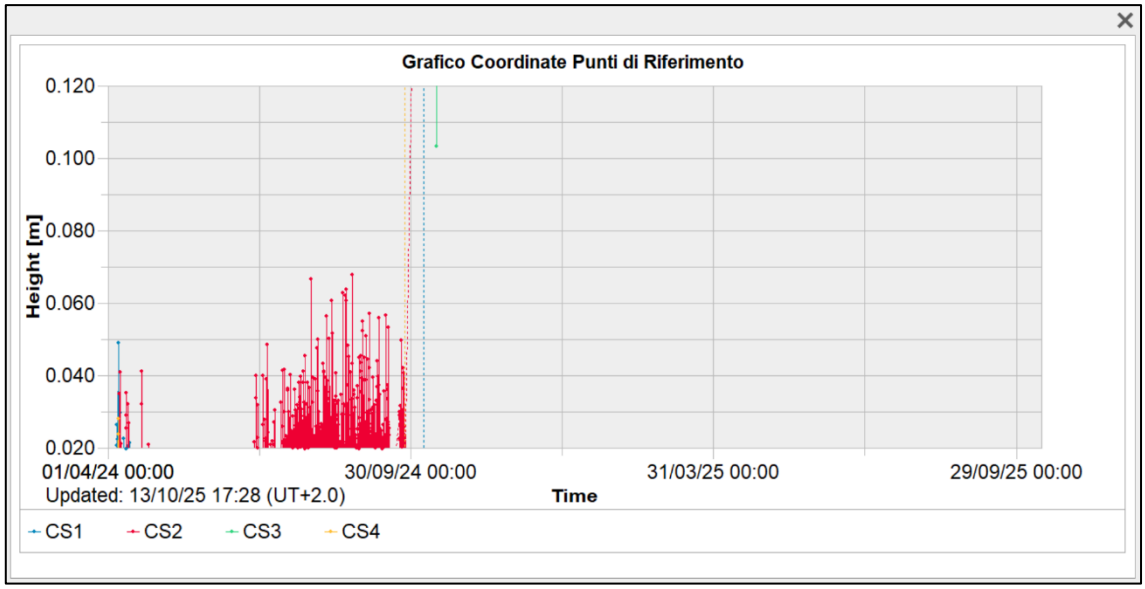

Figure 58. Coordinate graph of reference points, Height of CS1, CS2, CS3 and CS4.

3.1.3 GNSS-GPS results

Figure 59 shows the location of the eight GPS devices installed to monitor the landslide. Six GPS were installed at the bypass of the gas pipeline, while the remaining two were placed immediately above the summit trench and the other slightly further downstream.

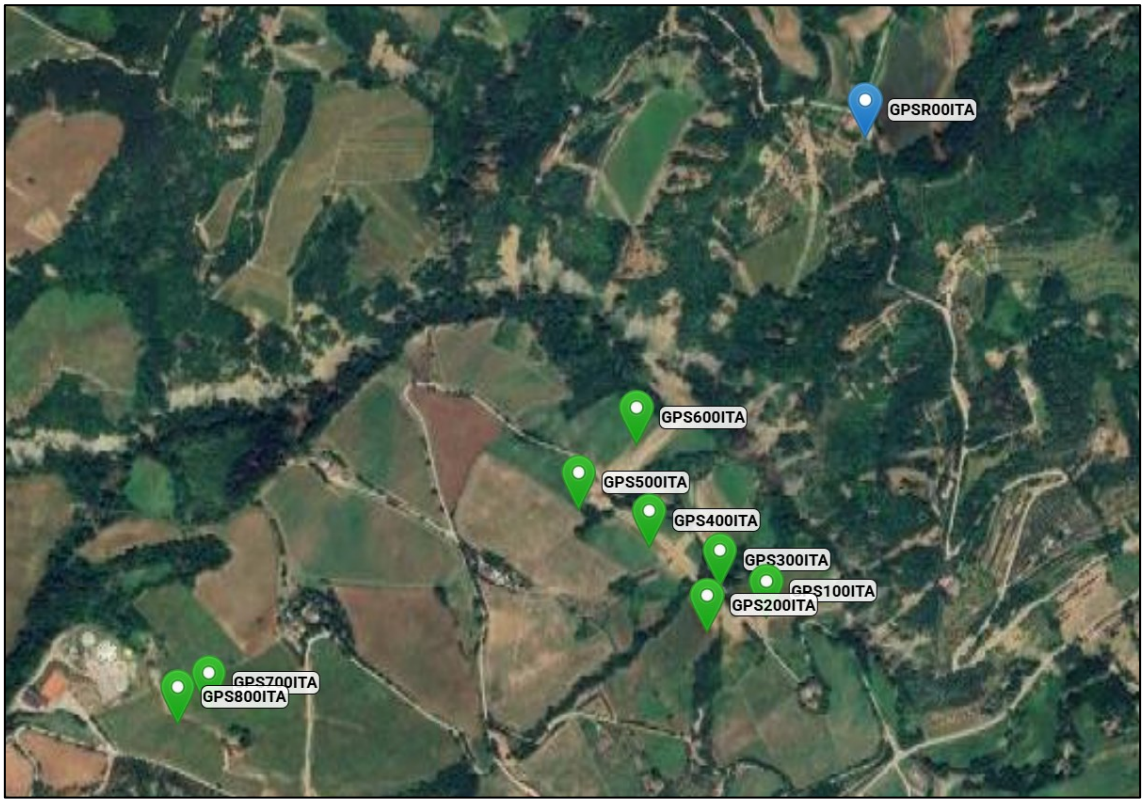

Figure 59. GPS location on the area of interest.

For each individual device, the height above sea level in meters, the displacement towards the East and towards the North, also in meters, are reported below, for a period ranging from 12 April 2024, the beginning of the instrument operation, until 30 November 2025. Figures 60-67 present the recorded data that will be examined in detail and interpreted in the following section.

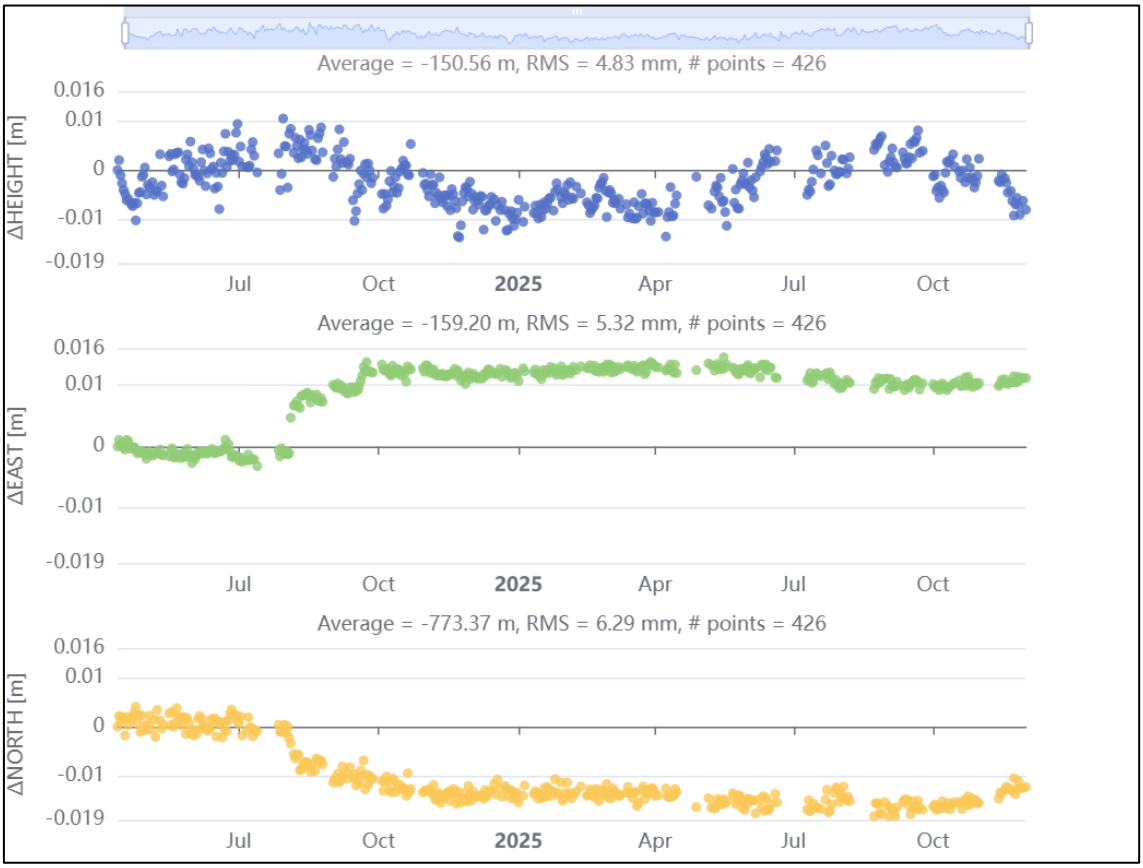

Figure 60. GPS100ITA data.

Figure 61. GPS200ITA data.

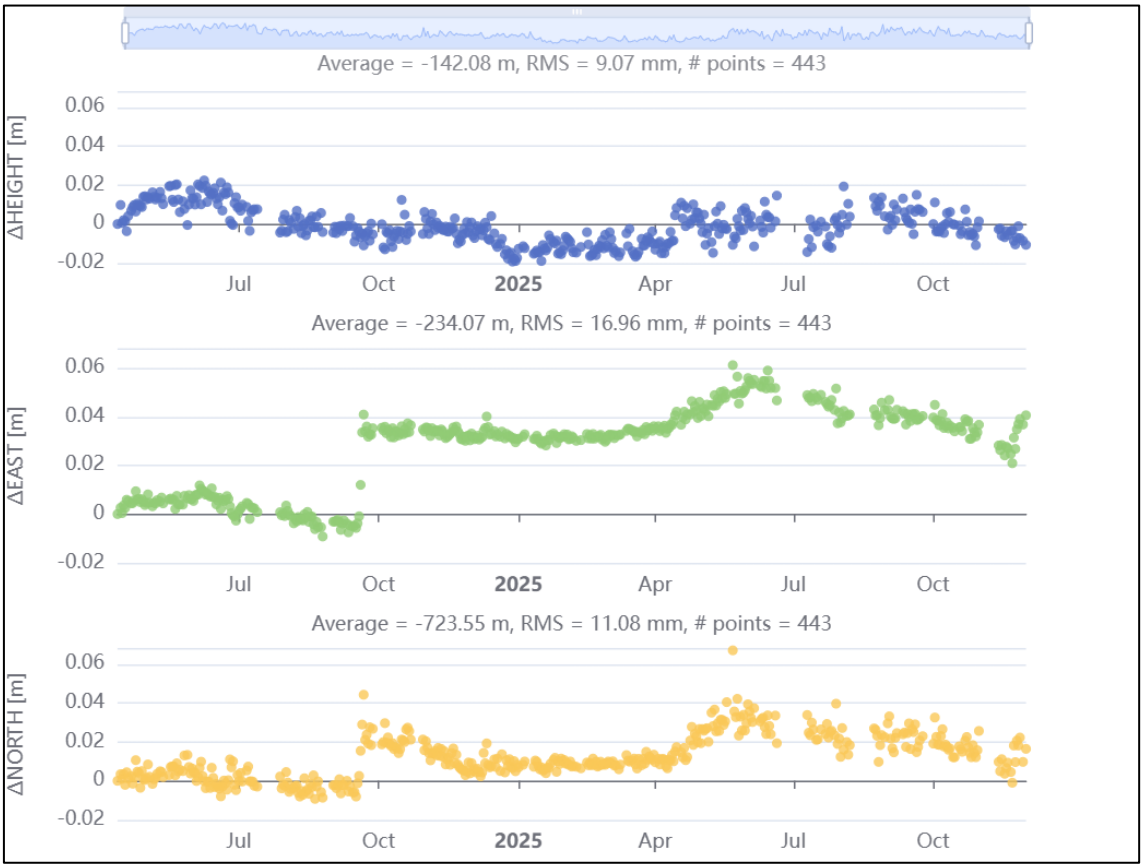

Figure 62. GPS300ITA data.

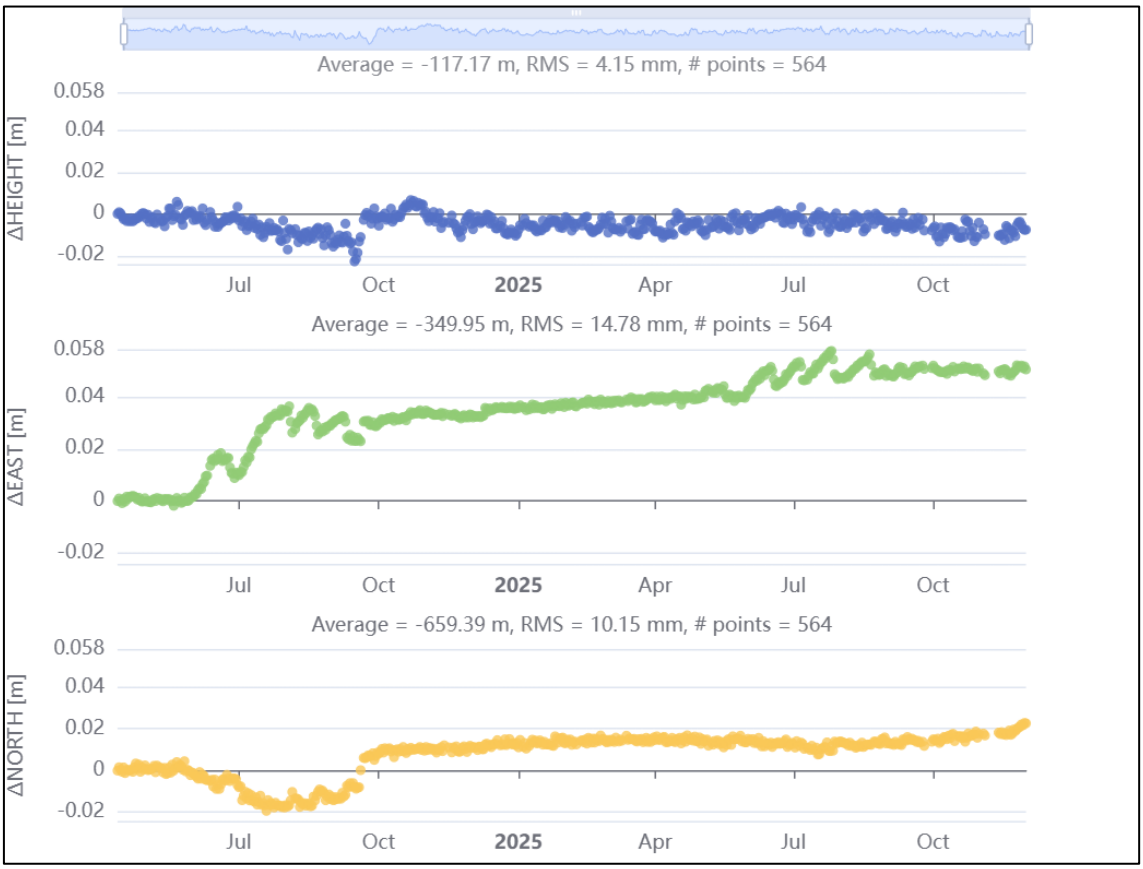

Figure 63. GPS400ITA data.

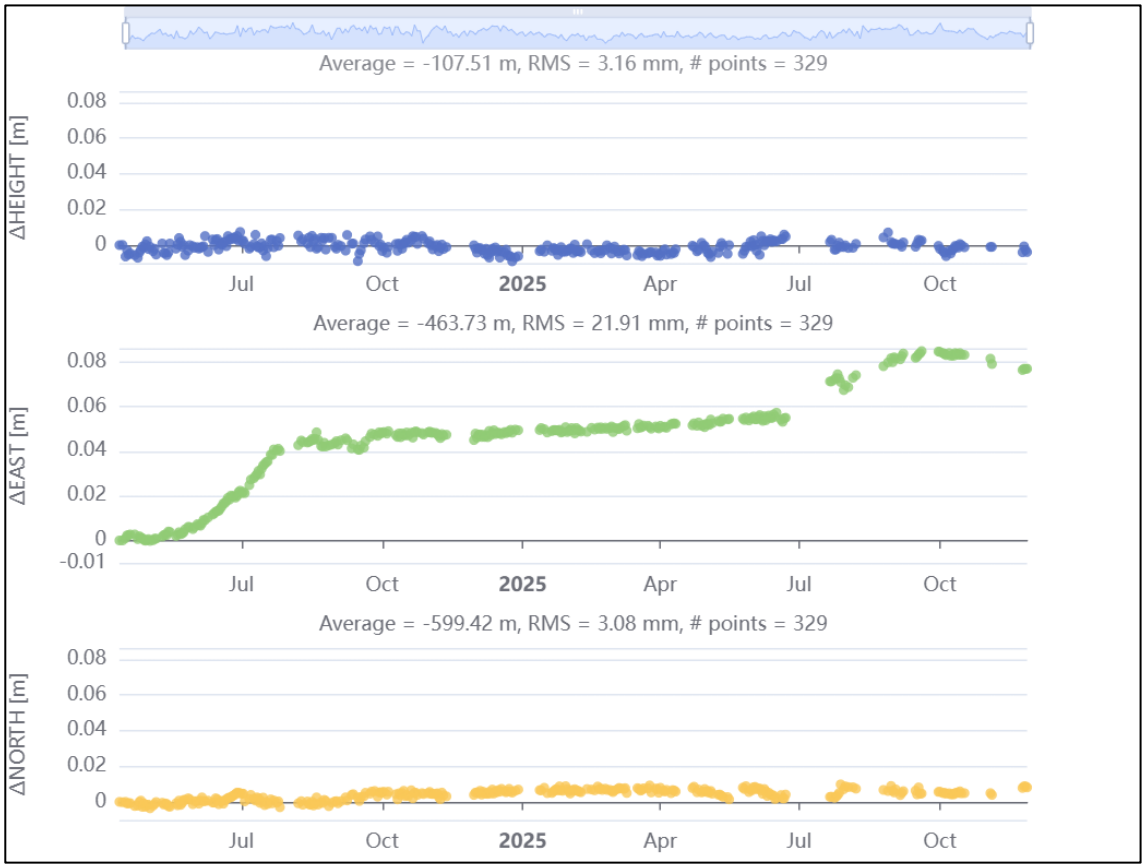

Figure 64. GPS500ITA data.

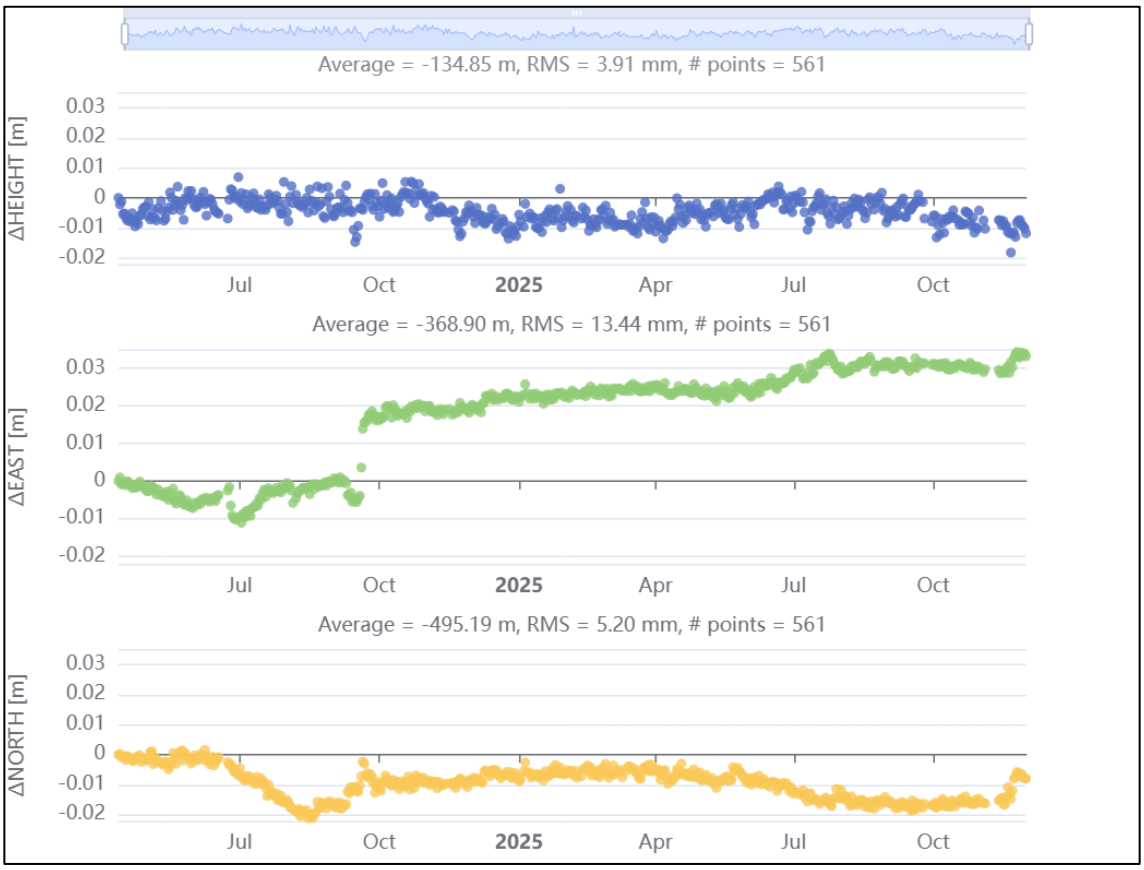

Figure 65. GPS600ITA data.

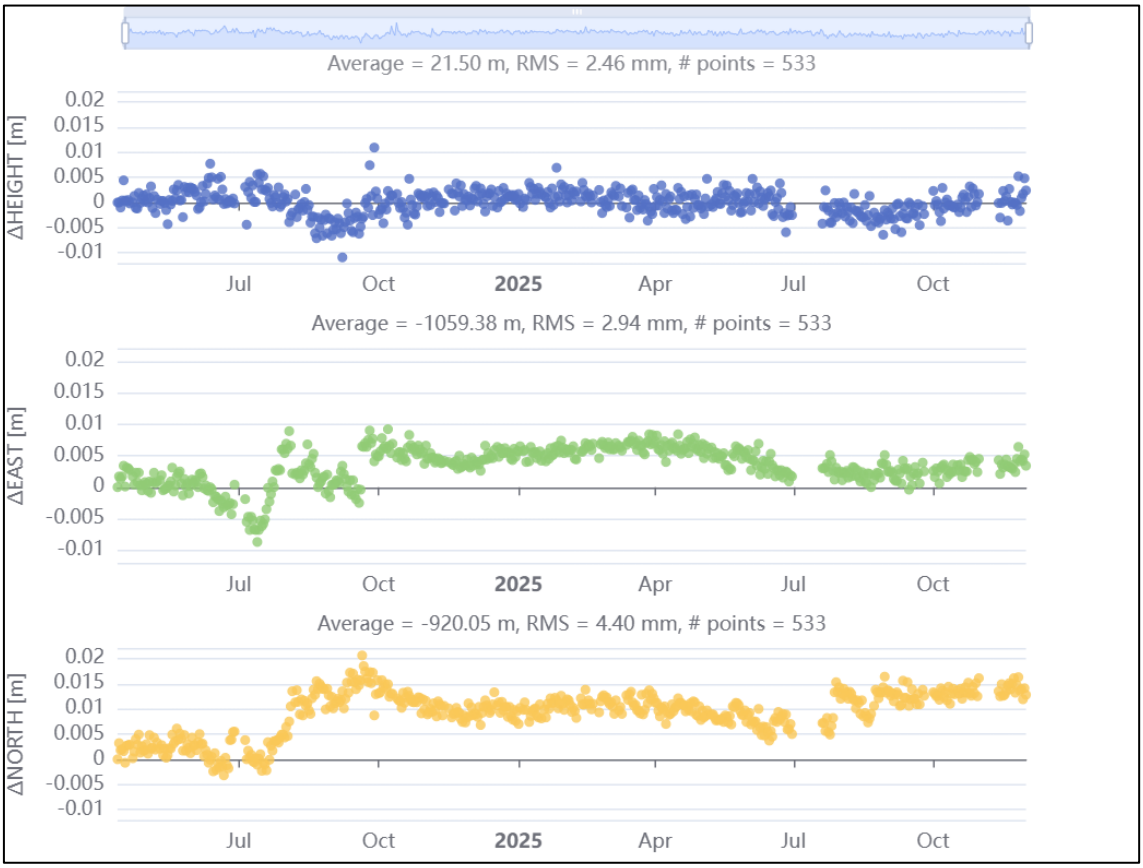

Figure 66. GPS700ITA data.

Figure 67. GPS800ITA data.

3.1.4. InSAR data results

Despite the limited dataset provided by EGMS, Figure 68, operating within the Sentinel-C band, meaningful insights can still be derived, particularly from ascending orbit acquisitions.

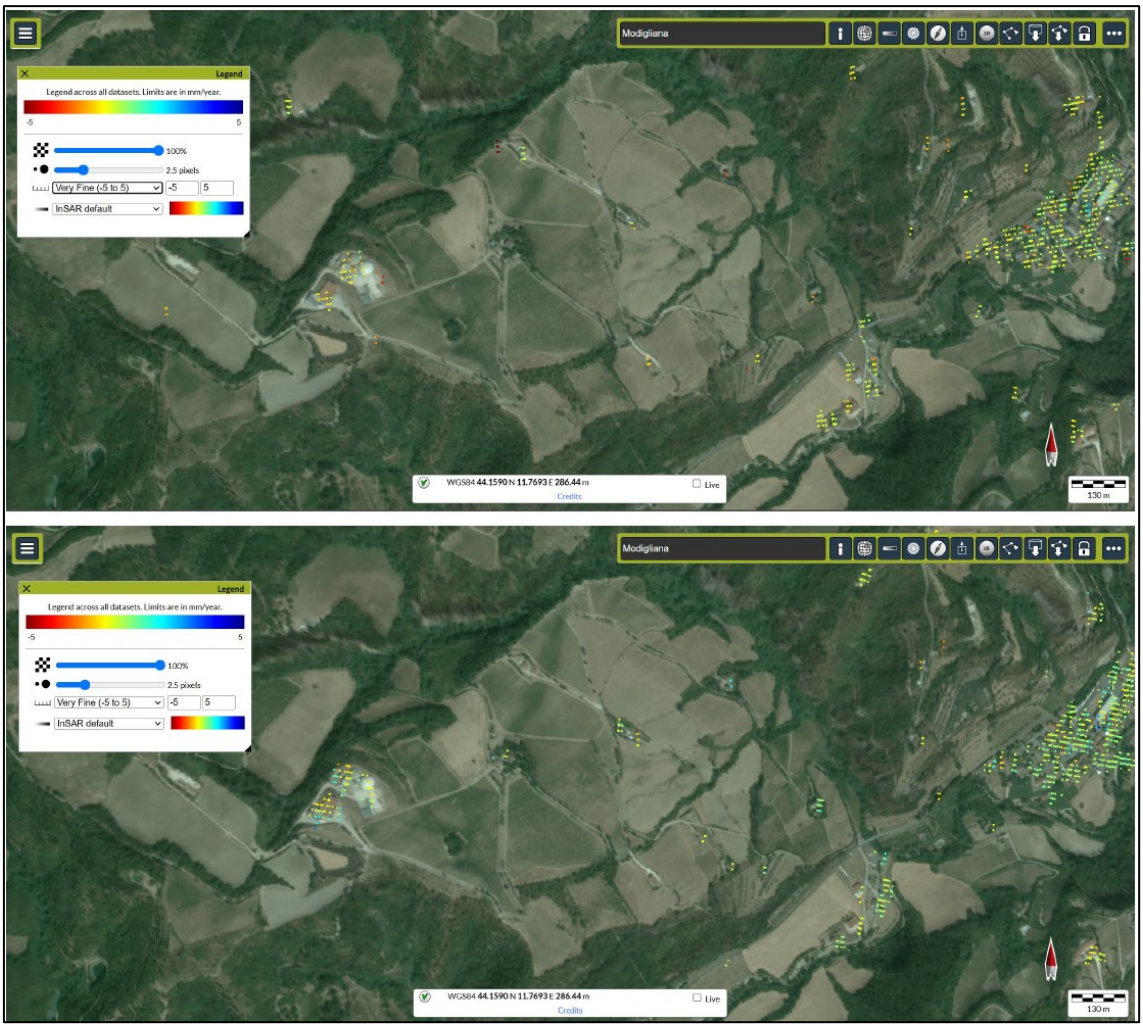

Figure 68. EGMS data (C-band Sentinel-1) for the Via Lago landslide area of interest in ascending (top) and descending (bottom) orbits.

The SAOCOM coverage is considerably more extensive, despite the relatively noisy dataset. Within the area affected by the Via Lago landslide, there are no Sentinel-1 reflectors, in contrast to the multiple SAOCOM acquisitions, as outlined in Figure 69. From this image, it is evident that the ascending and descending orbit data are distributed homogeneously both within the landslide-affected zone and the surrounding area. The colours in the legend refer to average speeds along the LOS in mm/year.

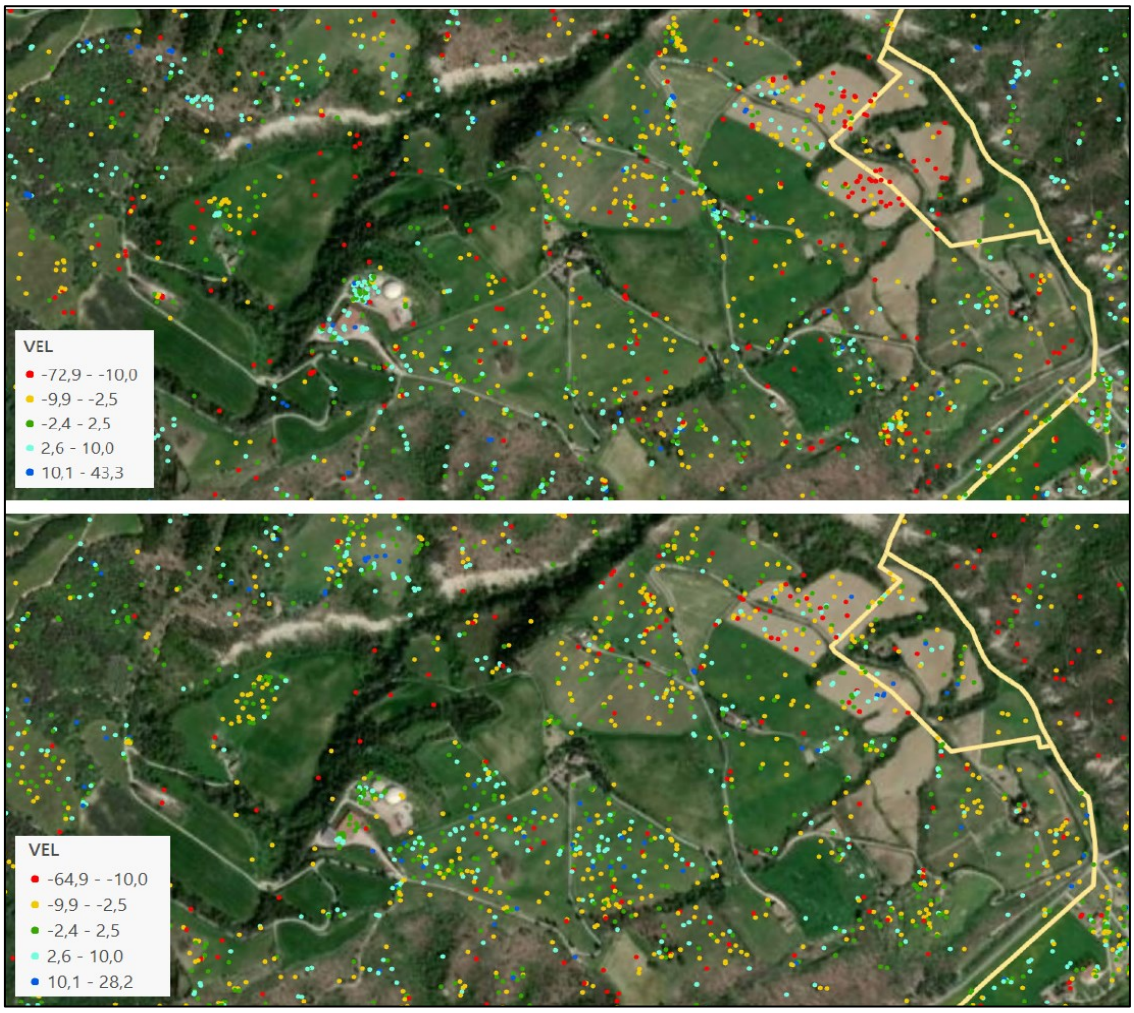

Figure 69. SAOCOM point density for the Via Lago side area. Ascending data at the top, descending data at the bottom.

Figure 70. SAOCOM reflectors in SqueeSAR mode with unique reference code, with analysed points highlighted in magenta.

.

The most interesting points analysed in the report are shown in image 70 and highlighted in magenta. For two points, A9XTKFJ and A9YF015, in the centre of the landslide area, the relative deformation/time graphs were calculated, Figure 71, again concerning the ascending orbit.

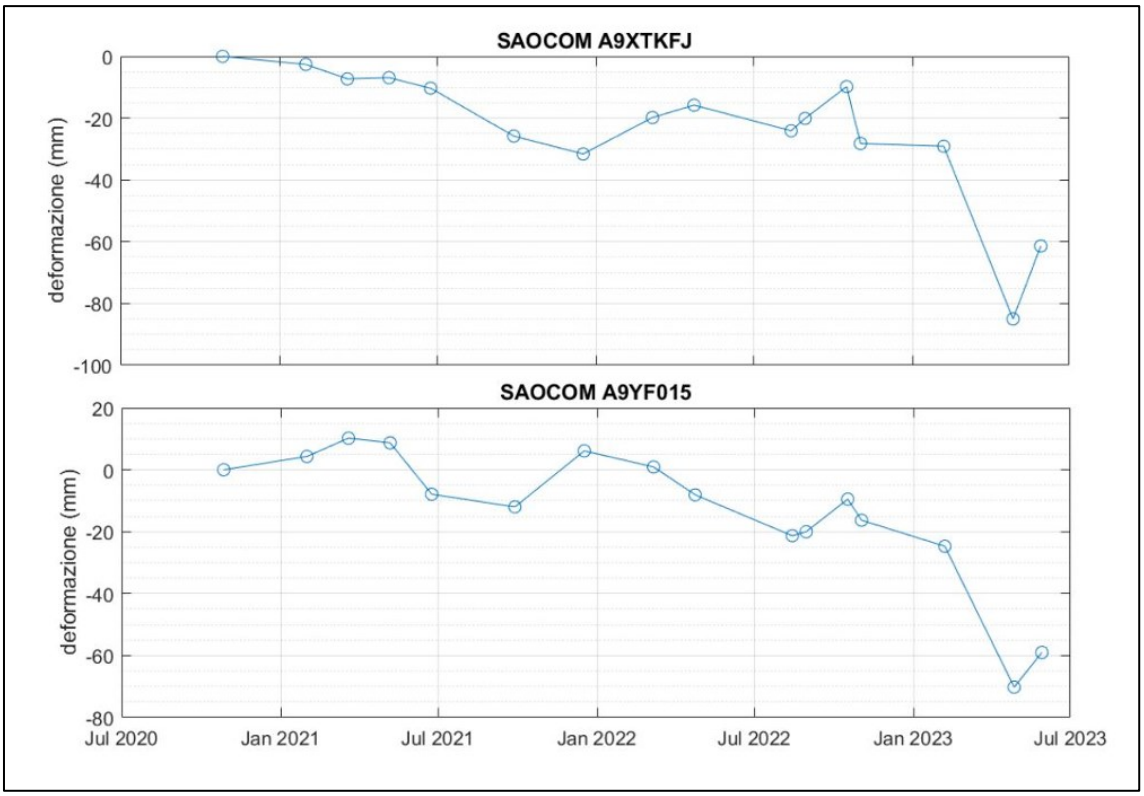

Figure 71. Deformation/time graphs for two points, SAOCOM A9XTKFJ and A9YF015 in the landslide centre area.

In order to obtain broader and more prolonged feedback, ALOS-2 data were also analysed, subjected to SqueeSAR interferometric processing as SAOCOM. The Japanese satellite observes the area of interest at a greater off-nadir angle (44.87°) than SAOCOM (36.5°), making ALOS-2 more suitable for observing low-angle hillsides, such as the one under examination. Figure 72 clearly shows that ALOS-2 displays a reduced number of reflectors compared to SAOCOM. A direct comparison of the time series is inherently difficult, as SAOCOM is based on a significantly shorter historical archive (approximately three years) than the eight years available from ALOS-2. However, the ALOS-2 dataset is characterised by irregular acquisition intervals and temporal baselines that are often longer and variable by a month. As a result, both datasets have distinct advantages and limitations.

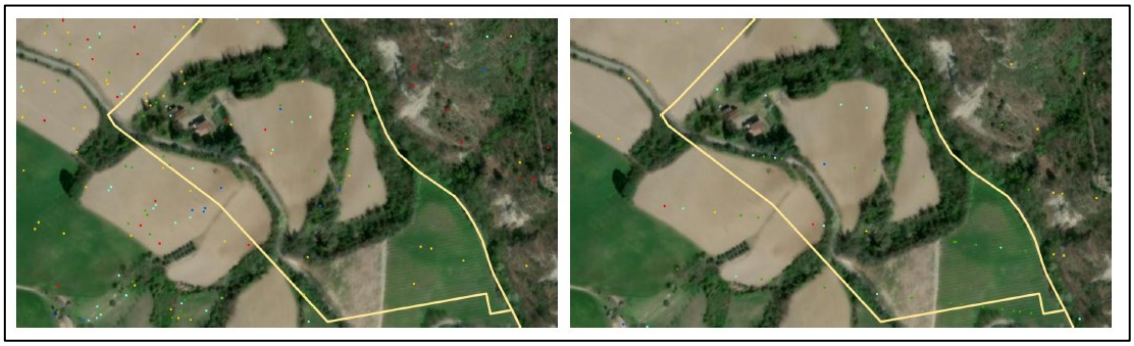

Figure 72. Comparison between SAOCOM (left) and ALOS-2 (right) point densities in the vicinity of the Via Lago landslide.

To overcome the constraint imposed by the lack of SAOCOM data after May 2023, the University of Padua provided the missing time series using the Persistent Scatterers (PS) technique. This method involves identifying target points—individual pixels within the image—that exhibit consistently high radar reflectivity over time. By analysing SAR data acquired sequentially, this approach aims to enhance the accuracy of ground displacement estimates and minimise errors caused by transient atmospheric disturbances. For each reference point, both the temporal displacement trend and the average velocity of movement were determined. The analysis was carried out using the ScanSAR module integrated into the SARscape software. The newly processed dataset covers the period from June 2023 to June 2025 and includes only descending orbit values, as ascending orbit data have not been processed properly. Figures 72 and 73 illustrate point velocities, focusing on the landslide body downstream and the trench upstream of the slope.

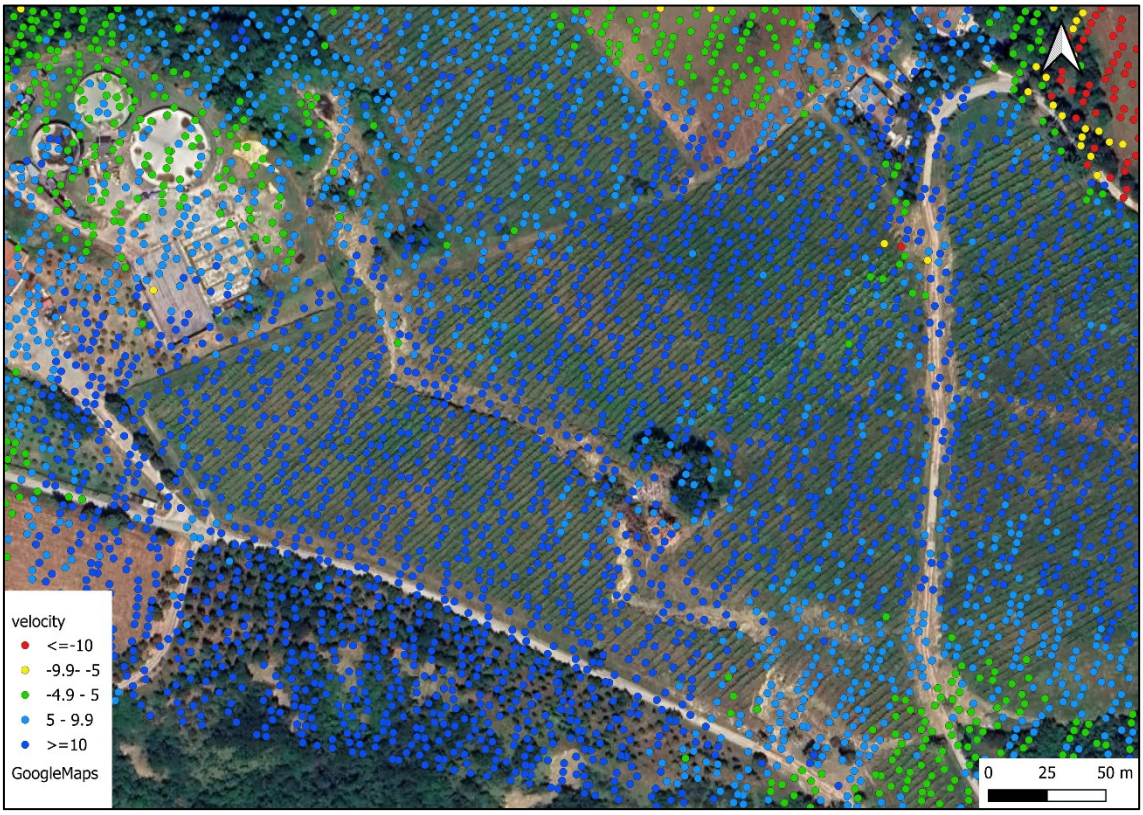

Figure 73. SAOCOM descending data of the slop upstream.

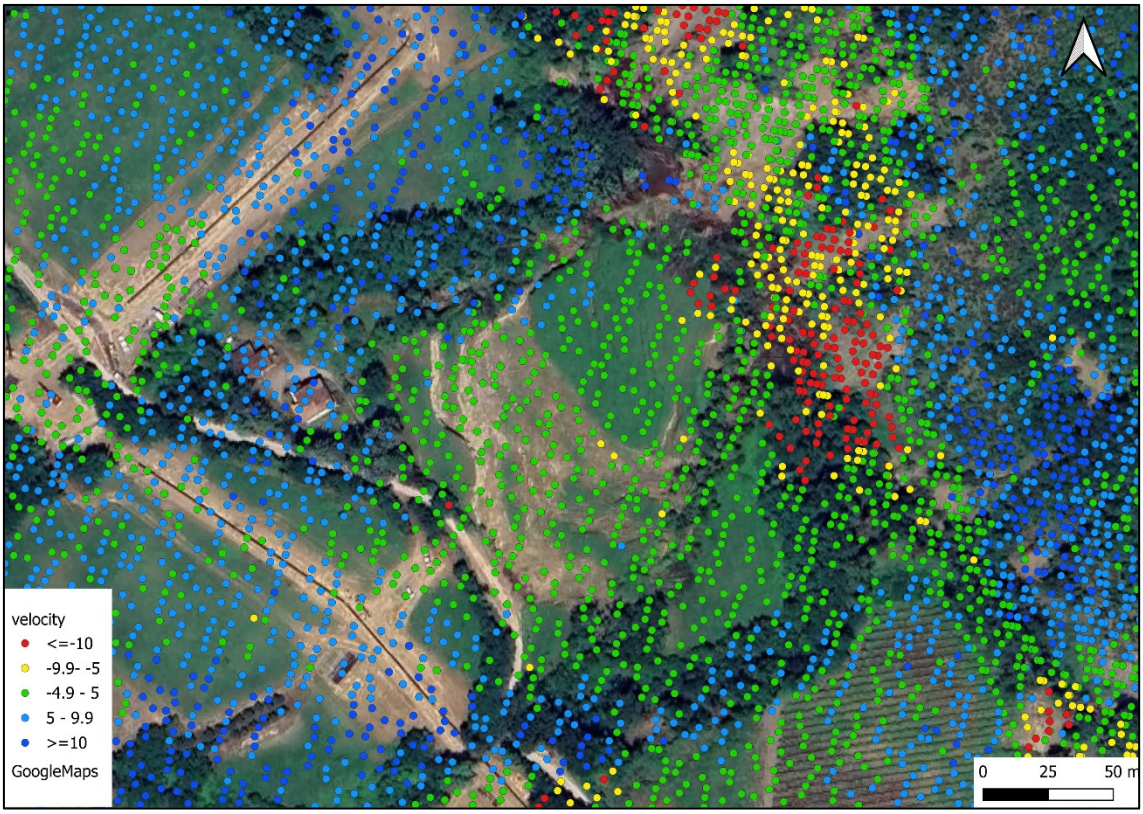

Figure 74. SAOCOM descending data of the slope downstream.

4. Discussion

4.1 Extensometers

Precipitation data recorded by the total station during 2024 indicate a well-defined seasonal rainfall pattern. Between January and July, rainfall generally occurs sporadically, with intensities ranging from low to moderate (≤ 20–25 mm), interspersed with a few isolated events of slightly higher intensity. A marked increase in precipitation is observed in early July, with amounts approaching 50 mm—sufficient to moisten the surface soil but insufficient to generate significant piezometric fluctuations or a notable rise in groundwater pressure. In August, a single rainfall event produces approximately 40–50 mm, which, although locally significant, does not substantially alter the water balance in the deeper sections of the slope. In contrast, the exceptional rainfall at the end of September, with an estimated total of 240 mm, constitutes an extreme event. Such intense and concentrated precipitation can induce a rapid increase in pore pressure, reactivate pre-existing fracture surfaces, and potentially accelerate the deformations recorded by extensometers. This event may represent the primary trigger for any movement or deformation signals observed in the subsequent weeks. From October to December 2024, rainfall remains moderate but frequent, creating prolonged soil saturation and maintaining elevated pore pressure. These conditions could favour residual movements or slow slope adjustments, even in the absence of further heavy rainfall. Overall, the rainfall pattern towards the end of 2024 suggests a hydrogeological scenario characterised by accumulated saturation. For extensometer C_0103, the initial curve appears almost stable around 0 mm, with instrumental or physiological micro-fluctuations indicating an absence of significant movement, consistent with the low rainfall during this period. From mid-June to mid-August, a slow but progressive negative displacement is observed, amounting to approximately 1–1.5 mm in total. The curve exhibits a sharp decrease of up to 3.5–3.7 mm, characterised by a very steep gradient between late August and early September. This phase coincides with moderate rainfall and the most intense precipitation episode in September, consistent with a flexural–compressive behaviour of the upper portion of the slope. A sudden positive shift of approximately 2.5–3 mm is then observed, followed by a subsequent stabilisation of the values. This can be interpreted as soil drainage and the consequent reduction in pore pressure; however, the recovery is incomplete, indicating residual deformation.

The C_0102 extensometer, located slightly lower than C_0103 and still outside the landslide body, exhibits a similar response to the September event but differs in its initial behaviour, where a gradual decrease is observed. Being positioned further downslope, it is likely more influenced by water infiltration, which tends to persist downstream for longer periods.

The R_0003 strain gauge shows a cumulative decreasing trend throughout the year, with step-like variations synchronised with the most significant rainfall pulses, similar to the behaviour of the R_0006 strain gauge. The R_0004 strain gauge also displays a comparable pattern, with the notable difference of being strongly affected by the exceptional September event. In fact, a pronounced vertical drop in the curve is evident, followed by stabilisation until the end of the year.

The R_0005 extensometer is positioned more externally, on the right-hand edge relative to the landslide body, and therefore acts as a peripheral sensor, useful as a control point for deformation outside the most active zone. The graph confirms that the point monitored by R_0005 is not actively under tension but tends towards slow shortening, indicative of compressive behaviour of the slope, at least during the initial months. Between late September and early October, a marked negative peak occurs, corresponding to the exceptional 240 mm rainfall event. A partial recovery towards less negative values is then observed, indicating that part of the deformation is irreversible.

4.2 Reflectors

Monitoring using a total station and reflectors installed along the slope enabled a detailed assessment of the response of the area above and adjacent to the main landslide body. As shown in the previous results, the reflectors are grouped into five functional sets:

- P1001-P1007, above the detachment zone
- P1008-P1014, left sector above the landslide
- P1015-P1021, halfway up the slope
- P1022-P1030, halfway up the slope
- P1032-P1039, upper part of the slope

The reflectors positioned immediately above the landslide (P1001–P1007) exhibit millimetric variations in both the Easting and Northing components, distributed in a substantially symmetrical manner with respect to the zero line, with oscillations of less than ±0.01–0.015 m. Some anomalous movements are observed during the September event, attributable to the combined effects of intense rainfall, atmospheric disturbances, and possible optical refractions, but not to actual ground movement. Therefore, in the absence of cumulative trends of either positive or negative displacement, the summit portion demonstrates substantial stability.

A similar pattern is observed in the group of reflectors installed further to the left of the first set, still outside the landslide body. The graphs show limited variations, generally within a few millimetres. Some points exhibit isolated peaks in both the Easting and Northing components, likely attributable to reading errors or atmospheric disturbances rather than actual ground movement. The reflectors from P1015 to P1021 constitute an additional fundamental control set, positioned in an intermediate location on the slope and upstream of the landslide situated further downslope. In this case, oscillations are imperceptible during the initial period and become more evident towards the end of September, though without directional coherence. This behaviour confirms that the median sector is not involved in any gravitational instability process, either superficial or deep. A similar dynamic is observed in the second series of reflectors (P1022–P1030), as well as in the subsequent group (P1031–P1039).

Therefore, no significant trend is observed. During the critical September event, a sudden increase in data dispersion is noted, with both positive and negative shifts. In general, due to the lack of instrument maintenance by the installation company, the dataset is temporally discontinuous and excessively scattered, making it of limited use for more detailed analysis.

Nevertheless, it can support general observations, given the considerable number of reflectors, and provide a basis for comparison with other monitoring methods.

4.3 GPS

The GPS graphs illustrate the evolution of movements since the start of monitoring in April 2024 and enable a direct comparison between hydro-meteorological conditions and the dynamics already observed by the strain gauges and reflectors installed along the slope. Processing the time series for the Easting, Northing, and altitude components helps to evaluate seasonal trends, identify possible progressive displacements, detect phases of acceleration, or confirm periods of substantial stability. Distinct points installed on the slope can be compared to distinguish the areas most sensitive to movement and to identify sectors characterised by different kinematic behaviour.

Starting with the analysis of GPS100ITA, a progression characterised by modest movements along the three spatial components is evident. For the vertical component, variations show slight variations of around ±4–5 mm, without a significant trend. Examining the Easting component, the initial behaviour is stable, oscillating around zero within a moderate range, before shifting sharply towards positive values (approximately +10 mm). From October onwards, the values remain elevated, maintaining a new average position without further significant transitions. This suggests a permanent eastward displacement, likely occurring between late August and early September 2024, followed by a stabilisation phase, remaining around 5 mm over the entire time interval.

The Northing component shows a continuous negative trend, indicating a gradual southward movement. Combining these elements, the three-dimensional movement of the point can be reconstructed, summarised as follows: a progressive lowering, a sudden eastward shift between late summer and early autumn, and a gradual southward sliding.

The GPS200ITA, placed instead in the central portion of the slope and in an area more directly influenced by gravitational processes, shows a decidedly more marked behaviour and is consistent with an active deformation dynamic: a progressive migration towards positive values of the eastern component can be observed, with an increase up to approximately +60–70 mm during September 2024, and then remain stable until September 2025; similarly, the northern component also reaches values above +85 mm after July 2025. The vertical component remains essentially stable, with fluctuations of less than ±5 mm, indicating that the movement is not accompanied by significant lowering or raising of the ground.

The GPS700ITA sensor is located in the upper part of the slope, immediately upstream of the landslide but below the drainage trench, in an area that represents a transition zone between the stable summit area and the moving mass below. During the monitoring period (April 2024 - November 2025), the GPS700ITA recorded minor movements: the East component shows limited variations of approximately +5 mm, while the North component shows a slightly greater increase, in the order of +10-12 mm, with vectors oriented in a direction consistent with that of the landslide body below. The height is practically constant, with oscillations of less than a few millimetres. These values suggest that the GPS700ITA, although not completely static, is not directly involved in the main deformation process, but is affected in an attenuated form by the propagation of the displacement from the bottom towards the top.

The GPS800ITA sensor, positioned at the top of the trench, is not fully involved in the movement as is the case with GPS200ITA and the other downstream sensors. The data show a significant, though not extreme, horizontal displacement as records an increase of approximately +20–22 mm, while the vertical component moves by approximately +35–40 mm, describing a resultant vector oriented towards the north-east. The variations concerning the vertical component are mainly stable, with a slight downward trend. This confirms that the downstream is the portion of the slope most actively involved in the deformation process.

The overall assessment of the movements detected by the GPS sensors installed along the slope shows a difference in kinematic behaviour between the points located downstream, near the methane pipeline and the landslide that occurred in May 2023, and those located further upstream, near the trench. The sensors installed in the unstable area (GPS100ITA and especially GPS200ITA) show displacement vectors consistently oriented towards the north-east, with magnitudes of several centimetres, indicating that the landslide body is still actively deforming. In particular, the GPS200ITA sensor records the greatest contribution, confirming greater mobility in the central and lower parts of the slope.
On the contrary, the GPS700ITA and GPS800ITA sensors, while recording a slight tendency towards horizontal deformation, show significantly lower displacements than the points mentioned above and substantially stable vertical values, indicating that the trench effectively acts as a hydraulic-mechanical barrier and kinematic separation.
The summit area of the slope is therefore relatively stable, with residual deformations of just a few millimetres.

Figure 75 provides an overview of the horizontal and vertical displacement vectors associated with each GPS.

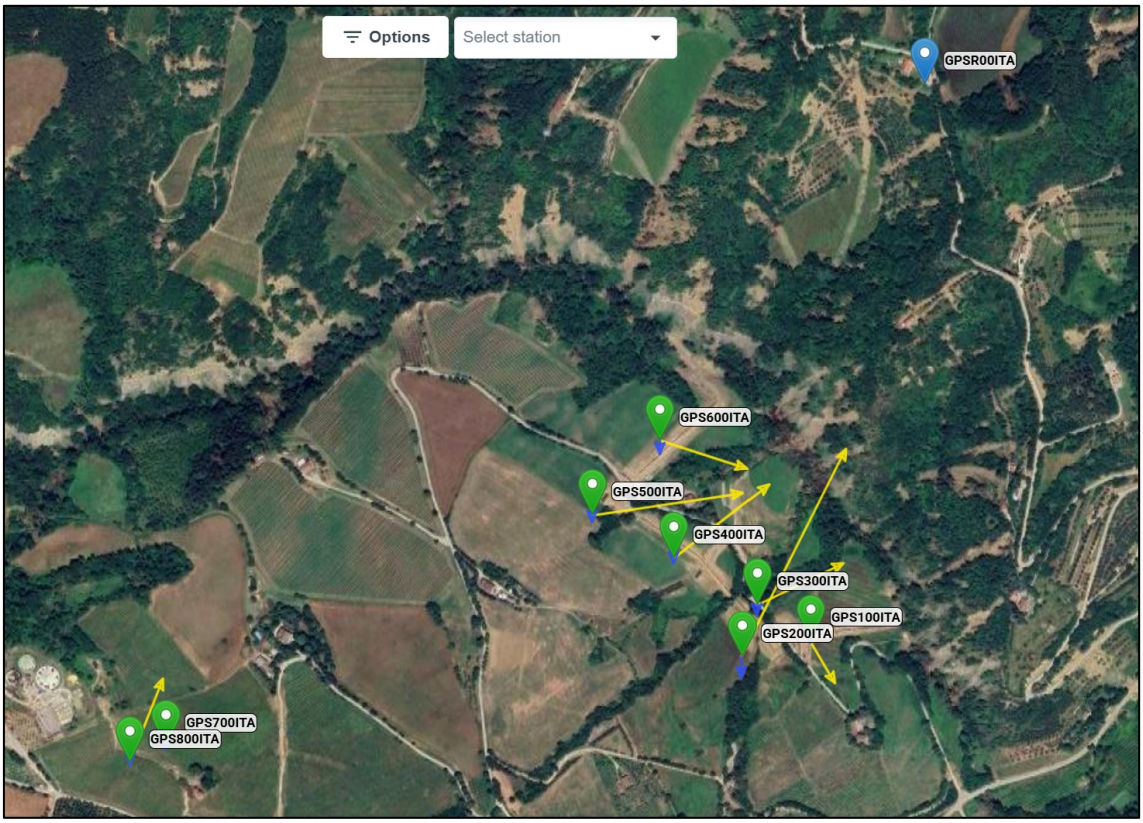

Figure 75. Vertical (blue arrow) and horizontal (yellow arrow) displacement vectors of GPS devices.

4.4 SAOCOM data

The EGMS datasets, especially in ascending orbit, suggest the presence of deformation precursors during the months preceding the May 2023 landslide.

Investigating the information collected by the SAOCOM satellite, it is immediately apparent that the future area affected by the landslide coincides with those where the average speed of movement is highest (indicated in red) during the period analysed. These points show movement along the satellite line of sight (LOS), away from the sensor, which is consistent with a displacement pattern oriented approximately along the steepest slope of the terrain.

Points exhibiting the highest average velocity were recorded between October 2020 and June 2023, with cumulative displacements in the order of 50–80 mm over a period of less than three years, showing a progressive trend during the months preceding the May 2023 event. The maximum recorded displacement values range from –60 mm to –80 mm, compared to those measured at the reflectors located at the centre of the landslide body. There is no acceleration or progression in the rate of deformation in the foot of the slope. This is to be expected and seems to confirm the stress state of the slope itself in the first quarter of 2023, marked by tensile stresses mainly in the part close to the road and in the centre of the actual detachment zone.

ALOS-2 also provides a smaller number of reflectors in this case (see Figure 74), yet it is advantageous for observing low-angle hillsides. A comparison between the two datasets was therefore conducted; however, it could not be continued because ALOS-2 data became unavailable just as deformations at point A7OUMA2 started to become apparent. Overall, the data trends are similar for both sensors.

Figure 76. ALOS-2 points discussed in comparison with SAOCOM, highlighted in magenta.

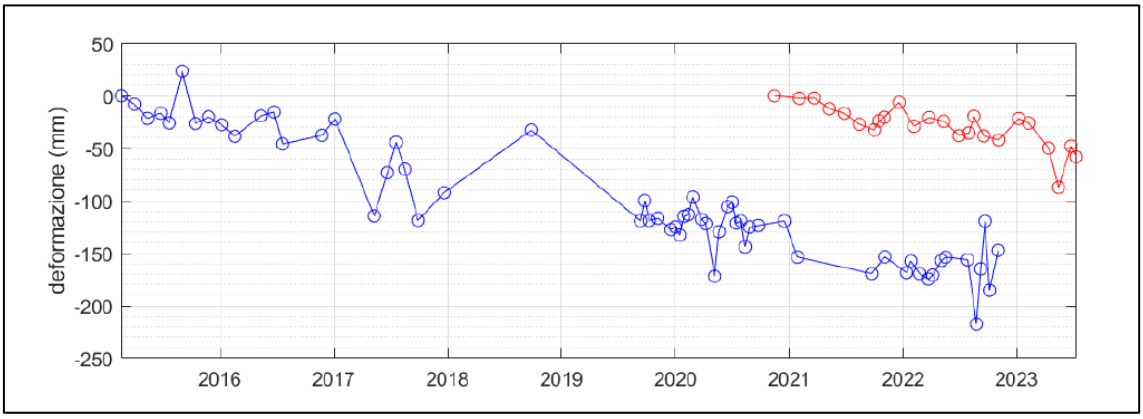

Figure 77. Comparison between SAOCOM-ALOS2 time series on points A7OUMA2 (red) and A7VEC1S (blue).

Despite the noise, ALOS-2, Figure 75, reveals a linear subsidence trend of approximately 170 mm over 8 years (Vavg = 21.5 mm/year). A comparable average rate was observed at the nearby SAOCOM point, which shows a similar linear trend until April 2023 (50 mm in 2.4 years, Vavg = 20.8 mm/year). Subsequently, an acceleration, absent in ALOS-2 due to the unavailability of data, probably corresponds to the rainy events of May 2023. After this episode, the previous deformation rate appears to resume unchanged.

Having only the descending orbit, it is not possible to calculate a complete 3D movement, but it is possible to obtain a very reliable view of vertical behaviour and a partial view of east–west movement. Positive LOS values indicate movement towards the satellite, typically associated with uplift or minor east-west components consistent with the line-of-sight geometry. Conversely, negative LOS values correspond to movement away from the satellite, generally interpreted as subsidence.

By evaluating the average LOS velocities obtained from SAOCOM data in descending orbit for the period July 2023 – July 2025, it is possible to clearly distinguish two deformation behaviours within the Modigliana slope. In the upper portion, at the trench formed after the rainfall event of 2023, the interferometric points show predominantly positive values, with LOS velocities between +4 and +12.

In the middle and lower parts of the slope, corresponding to the main landslide in Via Lago, the LOS velocities show negative values. The recorded velocities range from –10 to –25 mm/year. Projecting these values along the vertical component of the look vector, we obtain lowering velocities between –8 and –20 mm/year, with an estimated average value of around –14 mm/year, equivalent to about –28 mm of cumulative lowering over the entire observation period.

5. Conclusions

Overall, the monitoring system performed effectively throughout the entire observation period. All devices integrated into the network responded promptly to external inputs, particularly during the exceptional rainfall event that recorded 240 mm of precipitation. However, a more detailed analysis of the data obtained from each technique reveals that some instruments proved more reliable in delivering consistent results than others. Specifically, GPS sensors and SAOCOM satellite measurements provided more stable, continuous, and high-quality datasets, enabling the identification of movement trends with a reduced margin of uncertainty.

Conversely, although extensometers are valid field references, their limited number restricts their ability to provide extensive and representative measurements, as they only offer point-based data. These factors reduce the possibility of identifying large-scale deformation patterns. The use of reflective targets does not ensure adequate temporal continuity in the data series and highlighted significant dispersion in measured values, with considerable background noise. These limitations affect overall performance, despite prisms being evenly distributed along the slope.

Ultimately, the results validate the overall functionality of the monitoring system, highlighting that the combination of GPS measurements and satellite analysis represents the most effective approach currently available.

The findings also indicate potential benefits from future improvements to the system, such as increasing instrument density, optimising reflector positioning, and integrating additional measurement technologies to enhance spatial resolution and reduce data uncertainty. Furthermore, the fact that each method is managed by a different organisation or technician has led to variations in maintenance practices, data acquisition procedures, and quality control, resulting in inconsistencies and occasional gaps in the dataset. These limitations make it clear that, although the monitoring system has proven capable of detecting significant responses during periods of intense activity, further improvements are required, particularly through greater collaboration between responsible bodies, an increase in the number of ground-based instruments to ensure long-term reliability, stability, and interpretative accuracy of monitoring activities.

Based on the foregoing analysis, it is evident that a targeted comparison between GPS and InSAR (SAOCOM) datasets is required. Given that only the descending component derived from SAOCOM data, processed by the University of Padua, is available, these measurements can be compared exclusively with GPS observations.

This comparison indicates that the trench remains essentially stable, exhibiting a slight uplift. The GPS700ITA point immediately downstream confirms this behaviour, showing vertical oscillations of a few millimetres. These observations are consistent with SAOCOM interferometric data for the trench area, which reveal positive LOS velocities corresponding to a modest vertical displacement.

The GPS400ITA sensor, positioned upstream of the landslide on the upper edge of the slope, shows a vertical series characterised by millimetric variations, without any significant trend. The behaviour recorded is stable, with oscillations mainly attributable to seasonal effects or instrumental noise. This result is perfectly consistent with the SAOCOM data, which show LOS velocities close to zero in the summit area, corresponding to vertical movements of a few millimetres per year. The agreement between the two datasets confirms that the upper part of the slope is not involved in the main kinematics of the landslide, which instead develops mainly in the central and distal portions, where SAOCOM velocities are higher.

Analysis of GPS data reveals no significant displacement peaks associated with rainfall events, nor any correlation with minor precipitation. Regarding the 2025 dataset, no marked changes are observed, which can be attributed to the absence of exceptional rainfall events, Figure 78, comparable to those recorded in 2024, despite a higher number of rainy days.

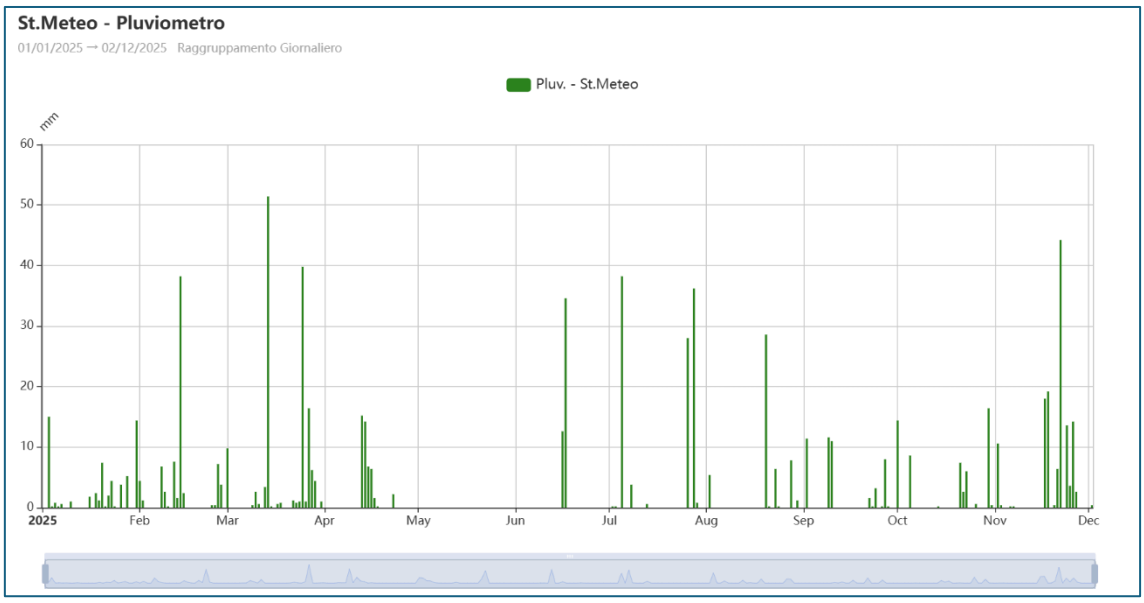

Figure 78. Results recorded by the weather station for precipitation from 1 January 2025 to 1 December 2025.

The downslope landslide is currently in motion: although its horizontal displacement is in the order of 10 cm over a couple of years, this magnitude is relatively insignificant within the given geomorphological context. However, if such movement were to occur within a residential setting, structural damage, such as wall fractures, would be expected. In the present case, the observation does not raise major concern, as the landslide is progressing towards the riverbed, beyond which lies a steep slope that would act as a natural barrier, effectively limiting further advancement.

Potential development of tension cracks, Figure 79, in the upper sector and within the detachment zone of the landslide represents a significant concern. The uppermost section exhibits a gentler slope compared to the lower portion of the landslide, which is inclined at approximately 15°, whereas the summit area, where the trench has formed, has an inclination of about 11°. This geometry makes downslope movement less likely; however, prolonged and intense rainfall could induce tension cracks due to elevated pore-water pressures within the rock strata. Such pressures may also generate an upward thrust along the weakest basal plane, producing uplift forces in addition to a vertical component that must be resolved along the reference axes.

The component parallel to the slip surface, combined with interstitial forces, contributes to overall instability. From the tension cracks, water overpressure could propagate towards the base of the block, resulting in an uplift force denoted as U, which further reduces the resisting forces. Tension cracks may also develop within the downslope trench, as these fractures typically form perpendicular to the direction of tensile stress. To mitigate the risk of crack formation, which could lead to detachment and subsequent movement of discrete blocks, anchoring systems could be installed on blocks that are clearly identifiable and structurally significant. A more effective approach involves preventing water ingress into fractures by implementing horizontal drainage systems both in the upper and lower sections of the slope. Such drainage would reduce pore-water pressure and hydrostatic uplift, thereby improving the overall factor of safety against failure.

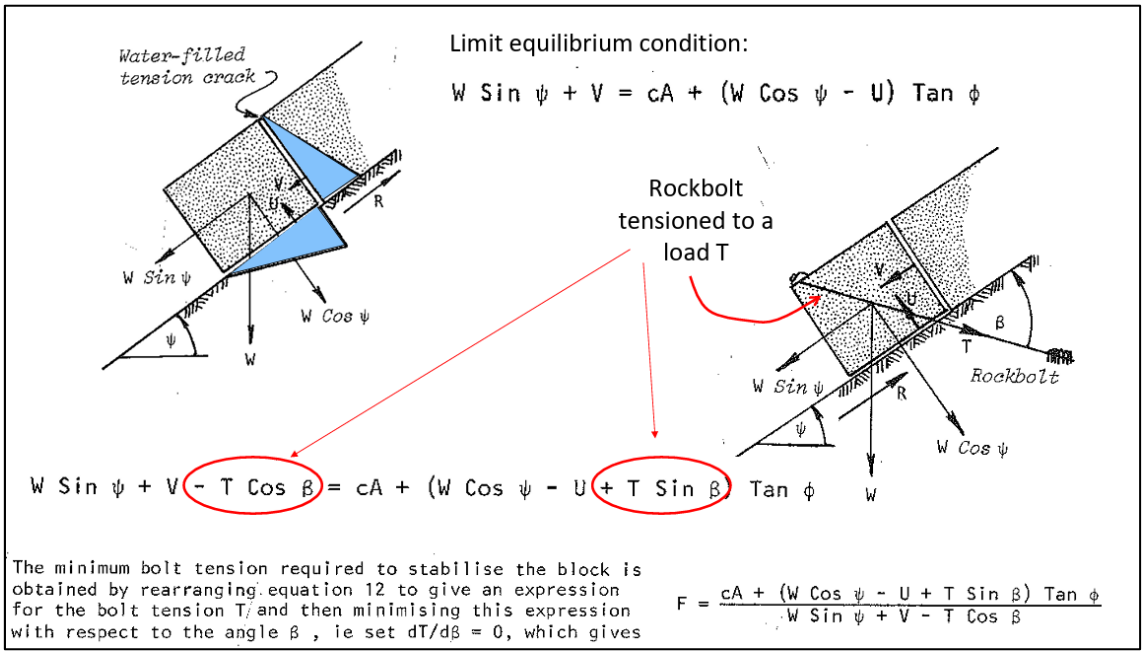

Figure 79. Effects of water pressure and reinforcement. F represent the safety factor, from Hoek and Bray 1977.

A comparative assessment of precipitation and reference system movements indicates that these systems exhibit an immediate response to extreme rainfall events, such as those of September 2024, or to events exceeding critical thresholds. It is therefore necessary to propose an alert system based on precise rainfall thresholds: 200 mm for a red alert, 100 mm for an orange alert and 60 mm for a yellow alert. This consideration is relevant and can be applied to areas with similar geomorphological characteristics of that considered, particularly where incipient or developing instability phenomena are present.

Bibliography

1. Antolini, G., Pavan, V., Tomozeiu, R., & Marletto, V. (2017). *Atlante Climatico dell'Emilia-Romagna 1961-2015*. Casma Tipolito, Bologna, Italy
2. Antolini, P., Borsetti, A. M., Cremonini, G., Pialli, G., Ricci Lucchi, F., & De Nardo, M. T. (2001). *Note Illustrative della Carta Geologica d'Italia alla scala 1:50.000, Foglio 254–Modigliana*. Servizio Geologico d'Italia.
3. Bertacchini, E., Castagnetti, C., Capra, A., Rivola, R., & Corsini, A. (2011). Rilievi integrati per il monitoraggio e la gestione dell'instabilità dei versanti. In *Geomatica: le radici del futuro–Tributo a Sergio Dequal e Riccardo Galetto* (pp. 89-98). Edizioni SIFET.
4. Brath, A., Casagli, N., Marani, M., Mercogliano, P., & Motta, R. (2023, 12 dicembre). *Rapporto della Commissione tecnico-scientifica istituita con deliberazione della Giunta Regionale n. 984/2023 e determinazione dirigenziale 14641/2023, al fine di analizzare gli eventi meteorologici estremi del mese di maggio 2023*. Bologna.
5. Cardinali, C., Foraci, R., Tesini, M. S., & Pizziolo, M. (2023, giugno 3). *Rapporto degli eventi meteorologici di piena e di frana dell'1-4 maggio 2023* (ARPArE, Servizio Sala Operativa e Centro Funzionale, Area geologia, sismica e suoli – Regione Emilia-Romagna). ARPAE Emilia-Romagna.
6. Casagli, N., Gigli, G., Carlà, T., Lombardi, L., & Nocentini, M. (2024, 24 ottobre). *Studio della Frana 1 in Via Lago, Modigliana (FC): Convenzione per prestazioni conto terzi tra il Centro per la Protezione Civile dell'Università degli Studi di Firenze e Snam Rete Gas S.p.A.* Centro per la Protezione Civile, Università degli Studi di Firenze.
7. Casagli, N., Gigli, G., Carlà, T., Lombardi, L., & Nocentini, M. (2025, febbraio 21). *Studio della frana di via Casale a Modigliana (FC) e della frana di via Monte Visano a Brisighella (FC): Frana 2 e Frana 3* (Convenzione per prestazioni conto terzi tra il Centro per la Protezione Civile dell'Università degli Studi di Firenze e Snam Rete Gas S.p.A.). Centro per la Protezione Civile, Università degli Studi di Firenze.
8. Catani, F., Floris, M., Rosi, A., Meena, S. R., Chen, X., & Puliero, S. (2024, 25 ottobre). *Analisi dati sat. frane 1,2,3 Forlì 2023: Area Modigliana, Frana Via Lago e intorno (Rapporto intermedio #1, Versione 1.0; Contratto n. 7300005141)*. Dipartimento di Geoscienze, Università degli Studi di Padova. Rapporto per SNAM Rete Gas S.p.A.
9. Farabegoli, E., Benini, A., Martelli, L., Onorevoli, G., & Severi, P. (1991). Geologia dell'Appennino romagnolo da Campigna a Cesenatico. *Memorie Descrittive della Carta Geologica d'Italia, 46*, 165-184.
10. Ferrario, M. F., & Livio, F. (2023). Rapid mapping of landslides induced by heavy rainfall in the Emilia-Romagna (Italy) region in May 2023. *Remote Sensing, 16*(1), 122.
11. Hoek, E. (1977, giugno). Structurally controlled instability in underground excavations. Paper presented at the *18th U.S. Symposium on Rock Mechanics (USRMS)*, Golden, Colorado.
12. ISPRA. (2023, maggio 17). *REPORT ISPRA 17 maggio 2023 – Evento alluvionale Emilia-Romagna 16–17 maggio 2023: Quadro di sintesi generale della pericolosità e del rischio di alluvioni nella Regione Emilia-Romagna*. Istituto Superiore per la Protezione e la Ricerca Ambientale. http://www.isprambiente.gov.it/files2023/notizie/pdf24_merged.pdf
13. ISPRA. (2023, maggio 19). *Nota: Quadro di sintesi dissesto frane Emilia-Romagna, Italia (aggiornamento 19/05/2023)*. Istituto Superiore per la Protezione e la Ricerca Ambientale. https://www.isprambiente.gov.it/files2023/notizie/nota-19-maggio.pdf

14. MUTTI, M. D. S. E., & Lucci, F. R. (1972). LE TORB| D| T| DELL'APPENNINO SETTENTRIONALE| NTRODUZIONE ALL'ANALS DI FACES (").
15. Savvaidis, P. D. (2003). Existing landslide monitoring systems and techniques. In *From stars to earth and culture* (pp. 242-258).
16. Snam Rete Gas S.p.A. (2023, novembre). *Metanodotto Arezzo–Minerbio: Variante definitiva Frana 1 in Comune di Modigliana (FC). Report indagini geognostiche: Indagini per variante in microtunnel*. Documento interno non pubblicato.
17. Thirugnanam, H., Uhlemann, S., Reghunadh, R., Ramesh, M. V., & Rangan, V. P. (2022). Review of landslide monitoring techniques with IoT integration opportunities. *IEEE Journal of Selected Topics in Applied Earth Observations and Remote Sensing, 15*, 5317-5338.